

Laser in der Materialbearbeitung
Forschungsberichte des IFSW

M. Eckerle
Generation and amplification
of ultrashort pulsed high-power
cylindrical vector beams

Laser in der Materialbearbeitung

Forschungsberichte des IFSW

Herausgegeben von

Prof. Dr. phil. nat. Thomas Graf, Universität Stuttgart
Institut für Strahlwerkzeuge (IFSW)

Das Strahlwerkzeug Laser gewinnt zunehmende Bedeutung für die industrielle Fertigung. Einhergehend mit seiner Akzeptanz und Verbreitung wachsen die Anforderungen bezüglich Effizienz und Qualität an die Geräte selbst wie auch an die Bearbeitungsprozesse. Gleichzeitig werden immer neue Anwendungsfelder erschlossen. In diesem Zusammenhang auftretende wissenschaftliche und technische Problemstellungen können nur in partnerschaftlicher Zusammenarbeit zwischen Industrie und Forschungsinstituten bewältigt werden.

Das 1986 gegründete Institut für Strahlwerkzeuge der Universität Stuttgart (IFSW) beschäftigt sich unter verschiedenen Aspekten und in vielfältiger Form mit dem Laser als einem Werkzeug. Wesentliche Schwerpunkte bilden die Weiterentwicklung von Strahlquellen, optischen Elementen zur Strahlführung und Strahlformung, Komponenten zur Prozessdurchführung und die Optimierung der Bearbeitungsverfahren. Die Arbeiten umfassen den Bereich von physikalischen Grundlagen über anwendungsorientierte Aufgabenstellungen bis hin zu praxisnaher Auftragsforschung.

Die Buchreihe „Laser in der Materialbearbeitung – Forschungsberichte des IFSW“ soll einen in der Industrie wie in Forschungsinstituten tätigen Interessentenkreis über abgeschlossene Forschungsarbeiten, Themenschwerpunkte und Dissertationen informieren. Studenten soll die Möglichkeit der Wissensvertiefung gegeben werden.

Generation and amplification of ultrashort pulsed high-power cylindrical vector beams

von Dr.-Ing. Michael Eckerle
Universität Stuttgart



utzverlag München

Als Dissertation genehmigt
von der Graduate School of Excellence advanced Manufacturing Engineering
der Universität Stuttgart

Hauptberichter: Prof. Dr. phil. nat. Thomas Graf
Mitberichter: Prof. Dr.-Ing. Manfred Berroth

Bibliografische Information der Deutschen Nationalbibliothek
Die Deutsche Nationalbibliothek verzeichnet diese Publikation
in der Deutschen Nationalbibliografie; detaillierte bibliografische
Daten sind im Internet über <http://dnb.ddb.de> abrufbar.

Zugleich: Dissertation, Stuttgart, Univ., 2019

D 93

Das Werk ist urheberrechtlich geschützt.
Sämtliche, auch auszugsweise Verwertungen bleiben vorbehalten.

Copyright © utzverlag GmbH 2019

ISBN 978-3-8316-4804-7

Printed in Germany

utzverlag GmbH, München
Tel.: 089-277791-00 · www.utzverlag.de

Contents

Contents	5
List of Symbols	8
Abstract	12
Kurzfassung	15
1 Introduction	20
2 State of the art	22
2.1 Extra-cavity generation of CVBs	22
2.2 Intra-cavity generation of CVBs in continuous wave operation	24
2.3 Intra-cavity generation of CVBs in pulsed operation	25
2.4 Amplification of CVBs	26
3 Objective of this work	27
3.1 Polarization state	28
3.2 Pulsed operation	28
3.3 Laser technology	29
4 Cylindrical vector beams	31
4.1 Vortex versus cylindrical vector beams	31
4.2 Evaluation of the polarization purity	34
5 Radially polarized mode-locked thin-disk laser	42
5.1 Considerations regarding the behavior of the SESAM	42
5.1.1 Saturation	42
5.1.2 Damage threshold	45
5.2 Grating waveguide output coupler	47
5.2.1 Design	47
5.2.2 Production and qualification	49
5.3 Effects of an intra-cavity phase shift	52
5.4 Considerations regarding the cavity design	55

5.5	Setup	56
5.6	Experimental results	58
5.6.1	Performance in continuous wave operation	60
5.6.2	Performance in mode-locked operation	61
5.7	Summary	66
6	High-power single-stage single-crystal fiber amplifier	69
6.1	Single-crystal fiber module	70
6.2	Kerr lens self-focussing	70
6.3	High-power pumping	73
6.4	Setup	76
6.5	Experimental results	77
6.6	Summary	87
7	Summary and outlook	89
	Bibliography	92
	Acknowledgements	101

List of Symbols

Symbol	Meaning	SI-Units
Latin Letters		
A	Constant; Entry in the cavity round trip matrix	
AOI	Angle of incidence	°
A_{RAH}	Magnitude of an Extended Jones state	
D	Entry in the cavity round trip matrix	
$DOAP$	Degree of azimuthal polarization	%
$DOH1P$	Degree of hybrid1 polarization	%
$DOH2P$	Degree of hybrid2 polarization	%
$DORP$	Degree of radial polarization	%
E	Electric field	V/m
\hat{E}	Normalized measured electric field vector	
\hat{E}_{azi}	Normalized electric field vector of an ideal azimuthally polarized beam	
\hat{E}_{h1}	Normalized electric field vector of an ideal hybrid1 polarized beam	
\hat{E}_{h2}	Normalized electric field vector of an ideal hybrid2 polarized beam	
\hat{E}_{rad}	Normalized electric field vector of an ideal radially polarized beam	
$E_{1,RAH}$	Electric field of a CVB with a radial polarization	V/m
$E_{2,RAH}$	Electric field of a CVB with an azimuthal polarization	V/m
$E_{3,RAH}$	Electric field of a CVB with a hybrid1 polarization	V/m
$E_{4,RAH}$	Electric field of a CVB with a hybrid2 polarization	V/m
E_{nm}	Electric field of a Hermite-Gaussian mode	V/m
E_p	Pulse energy	J
E_{pl}	Electric field of a Laguerre-Gaussian mode	V/m
f_{rep}	Repetition rate of a pulse laser	1/s
F_p	Pulse fluence	J/m ²
F_{pD}	Pulse fluence of a doughnut-shaped beam	J/m ²

Symbol	Meaning	SI-Units
F_{pG}	Pulse fluence of a Gaussian beam	J/m ²
F_{sat}	Saturation fluence of a SESAM	J/m ²
\hbar	Reduced Planck's constant ($1.054571 \cdot 10^{-34}$)	Js/rad
H_m	Hermite polynomial	
H_n	Hermite polynomial	
I	Intensity	W/m ²
k	Angular wavenumber	1/m
\vec{J}_{ext}	Extended Jones vector	
l	Order of the Laguerre-Gaussian mode	
L_p^l	Laguerre polynomial	
m	Order of the Hermite-Gaussian mode	
M^2	Beam quality factor	
M_{POL}	Mueller matrix of a polarizer	
M_{QWP}	Mueller matrix of a quarter-wave plate	
n	Order of the Hermite-Gaussian mode	
n_0	Linear refractive index	
n_2	Nonlinear refractive index	
p	Order of the Laguerre-Gaussian mode	
p_{azi}	Projection of a normalized measured electric field onto the ideal azimuthal state	
p_{h1}	Projection of a normalized measured electric field onto the ideal hybrid1 state	
p_{h2}	Projection of a normalized measured electric field onto the ideal hybrid2 state	
p_{rad}	Projection of a normalized measured electric field onto the ideal radial state	
P	Average power	W
\hat{P}	Pulse peak power	W
P_{abs}	Absorbed power	W
P_{crit}	Critical power	W
P_{extr}	Extracted power	W
P_{out}	Average output power of a pump diode	W
P_{pump}	Average output power of an amplifier	W
P_{seed}	Average power of the seed	W

Symbol	Meaning	SI-Units
ΔP_{out}	Variation of the average output power of the amplifier	W
r	Radial distance in a cylindrical coordinate system	m
R	Radius of curvature of the phase front of a beam	m
R	Reflectivity of an optical component	
R_{lin}	Reflectivity of a completely unsaturated SESAM	
R_{ns}	Reflectivity of a saturated SESAM	
R_{tot}	Total reflectivity of a SESAM for an incident beam with an arbitrary beam shape	
RoC_d	Radius of curvature of the laser disk	m
RoC_{Disk}	Radius of curvature of the laser disk	m
RoC_s	Radius of curvature of the SESAM	m
ΔR	Saturable absorption of a SESAM	
ΔR_{ns}	Non-saturable absorption of a SESAM	
S	Saturation of a SESAM	
\vec{S}	Stokes vector	
$S_0 - S_3$	The four Stokes parameters	
TBP	Time bandwidth product	
w	Radius of a Gaussian beam	m
w_0	Radius of a Gaussian beam at the waist	m
w_d	Radius of a doughnut shaped beam at the waist	m
x	Position coordinate in a Cartesian system	m
\hat{x}	Unit vector in x-direction	m
y	Position coordinate in a Cartesian system	m
\hat{y}	Unit vector in y-direction	m
z	Distance to the beam waist	m
Greek Letters		
β_{TPA}	Two photon absorption coefficient	m/W
δ	Phase shift	rad
δ_{RAH}	Phase of an Extended Jones state	rad
η_{abs}	Absolute efficiency	rad
η_{extr}	Extraction efficiency	rad
θ	Azimuth angle in a cylindrical coordinate system	rad
θ_{pol}	Orientation angle of a polarizer	rad
λ	Wavelength	m

Symbol	Meaning	SI-Units
λ_0	Wavelength in vacuum	m
$\Delta\lambda$	FWHM spectral width of a laser	m
ξ	Gouy phase	rad
τ_p	Pulse duration	s

Abstract

Due to their unique properties, the cylindrical vector beams (CVB) with their axially symmetric polarization state, and in particular the LG_{01}^* mode with its doughnut-shaped intensity distribution, have shown their potential in various applications such as e.g. particle trapping and the excitation of plasmons in rotationally symmetric structures [1] or the acceleration of electrons [2].

Particularly in several applications in the field of laser material processing the performance could be improved by using a CVB instead of a linearly or circularly polarized Gaussian beam. For example, depending on the process and processed material, the cutting speed and quality can be improved for laser cutting with a CO_2 laser [3,4]. For laser drilling applications with pulsed laser sources e.g. increased drilling speeds of 1.5 - 4 times could be demonstrated [5].

As a consequence of the disparity of the promising results and the small number of existing data on this matter, the European Union supported the project RAZIPOL, which started in 2013. To further investigate surface structuring of large areas and the drilling of wholes with a large aspect ratio, a system delivering several 100 W of average output power with an either radially or azimuthally polarized output beam was built. To obtain such a performance, a system composed of a seed laser, several single-crystal fiber (SCF) stages, and a subsequent thin-disk multipass (TDMP) amplifier was set up. The radial or azimuthal polarization of the output beam was realized by means of a polarization converter within the preamplifier stage. Even though the results achieved within RAZIPOL were impressive, it turned out that the high level of complexity of the seed system can cause problems in terms of long-term stability and the quality of the CVB.

Therefore, the aim of the present work was to develop an alternative seed system. Especially a reduced complexity, compared to the RAZIPOL system, and a good beam quality of the CVB, in terms of the homogeneity of the intensity and the radial polarization distribution, were the target. The latter is necessary as it strongly affects the final quality of the CVB after the amplification in the TDMP. The minimum targeted output power was 50 W and determined by the requirements of the TDMP amplifier.

To realize the desired results, a combination of a mode-locked thin-disk oscillator and a subsequent SCF amplifier was chosen. The thin-disk technology was used due to the power scalability of the concept. Mode-locked operation was achieved by means of a semiconductor saturable absorber mirror (SESAM). To obtain the radial polarization of the output beam of the system a grating waveguide mirror was used. This device is a grating mirror which additionally employs a waveguiding effect in its dielectric layers to achieve the desired polarization dependent reflectivity. The spectral behavior is modelled by varying the parameters of the grating and the layers. Until the beginning of this work, at the IFSW these devices were only used as highly-reflective mirrors at one end of the cavity in conjunction with a standard output coupler at the other end. As this time the SESAM already had to be positioned at one end of the cavity to obtain stable single-pulse operation, the grating waveguide mirrors' parameters had to be adapted, such that it could additionally act as an output coupler with the desired reflectivity. Due to the grating waveguide nature of the device and its use as an output coupler, the device is called "Grating Waveguide Output Coupler" (GWOC). As already mentioned before, one SCF amplifier stage was used to boost the output of the oscillator to the power level required by the TDMP. Compared to the SCF stages in RAZIPOL, a crystal with a lower doping concentration was chosen. This was done to diminish the thermal load in the crystal and thus, to reduce detrimental thermal effects which can negatively affect the CVB quality.

With this approach, the first mode-locked thin-disk oscillator with a radial output polarization could be demonstrated. A maximum output power of 13.3 W was achieved at a pump power of 61 W. The maximum average output power was limited by the onset of instabilities in the mode-locking process and the intensity distribution of the beam. The pulse repetition rate of the oscillator was 42.1 MHz, which resulted in a pulse energy of 316 nJ. Under the assumption of a sech^2 -shape of the pulses, a pulse duration of 907 fs was measured. This results in a pulse peak power of 0.31 MW. In terms of average output power, peak power and pulse duration these values were records for pulsed oscillators generating CVBs. The pulse energy was formerly only exceeded by Q-switched CVB systems. At the same time, the obtained homogeneity of the doughnut-shaped intensity distribution as well as the high degree of radial polarization (DORP) of 97 ± 1 % were unprecedented for such a pulsed oscillator system. With measured values of the M^2 below 2.1 this parameter was also close to the theoretical case.

As mentioned before, the oscillator output was boosted in a subsequent SCF amplifier. For this amplifier stage, two different pump diodes with nominal wavelengths of 940 nm and 969 nm were tested. Surprisingly, the diode with an emission wavelength of 940 nm lead to a better performance in terms of output power. With this particular diode an average output power of the amplifier of 69.7 W was obtained at a pump power of 482 W.

In comparison, with the second diode an average output power of 66.3 W was achieved for a pump power of 519 W. The pulse durations after the amplification were 1030 fs and 909 fs, respectively. The different values were a result of a variation of the pulse duration of the seed source, which was 938 fs in the experiment with the 940 nm diode and 800 fs in the experiment with the 969 nm diode. This resulted in pulse energies of $1.68\mu\text{m}$ (940 nm) and $1.63\mu\text{m}$ (969 nm) and corresponding pulse peak powers of 1.48 MW and 1.58 MW, respectively. While the gain of 5.2 was larger in the first experiment (compared to 5.0), the long-term stability was better when pumping at 969 nm. The values of the M^2 slightly increased to 2.1-2.4 in both experiments with the SCF booster. Additionally, the beams became slightly distorted and developed a minor astigmatism. As a result of a linear phase shift inside the SCF crystal and a subsequent optical component, the transmitted beams were polarized in the so-called "hybrid1" (H1) polarization. The degrees of H1 polarization were $96.4\pm 1\%$ and $96.1\pm 1\%$ for the case of pumping at 940 nm and 969 nm, respectively. To show that such a phase shift can easily be compensated, a half-wave plate was introduced in front SCF in the setup with the 969 nm diode. This resulted in a degree of radial polarization of the amplified beam of $94.1\pm 1\%$, while the other parameters stayed unaffected by the compensation. Despite the minor degeneration of the quality of the beam and the polarization state, the results are still very promising. Thus, an alternative seed system with a reduced complexity and a good beam quality was successfully realized.

Kurzfassung

Im Verlauf der letzten Jahrzehnte entwickelte sich ein immer größeres Interesse an Laserstrahlen mit axial-symmetrischen Polarisationszuständen, den sogenannten "cylindrical vector beams" (CVB). Vor allem die LG_{01}^* Mode, mit ihrer Doughnut-ähnlichen Intensitätsverteilung, ist dabei von besonderem Interesse für die verschiedensten Anwendungen. So kann diese beispielsweise für das Einfangen von Partikeln oder zur Anregung von Oberflächenplasmonen auf rotationssymmetrischen Strukturen verwendet werden [1]. Des Weiteren wurde nachgewiesen, dass ein solcher Strahl, unter der Verwendung einer Linse mit einer sehr hohen numerischen Apertur, auf einen extrem kleinen Durchmesser fokussiert werden kann. Bei einer ausreichenden Größe der numerischen Apertur kann dieser sogar signifikant kleiner werden als das theoretische Minimum eines Strahls mit homogener linearer Polarisation [6,7]. Dieser Effekt ist auf eine longitudinale z-Komponente des Laserstrahls zurückzuführen, die sich im Bereich der Strahltaile ausbildet und große Anteile der Laserleistung beinhalten kann. Bei einer azimutalen Polarisation des Laserstrahls bildet sich diese Komponente hingegen nicht aus. Theoretisch kann dies im Bereich der Strahltaile dazu genutzt werden, die Intensitätsverteilung, durch eine Anpassung des Verhältnisses von radialer und azimutaler Polarisation, zu modellieren [8]. Bei ausreichend hohen Spitzenleistungen im gepulsten Betrieb werden Strahlen mit dieser speziellen Polarisationsform zudem interessant in Applikationen zur Beschleunigung von Partikeln wie zum Beispiel Elektronen [2, 9], Ionen [10] und Protonen [11].

Die positiven Eigenschaften die sich durch diese Polarisationsformen für die Laser-Materialbearbeitung ergeben können, wurden schon 1999 von Niziev und Nesterov theoretisch aufgezeigt [12]. So sagten Sie eine erhöhte Schneidgeschwindigkeit voraus, wenn statt eines Laserstrahls mit einer linearen oder zirkularen Polarisation, ein Laserstrahl mit einer radialen Polarisation verwendet würde. 2010 wurde die Richtigkeit dieser Hypothese für einige Materialien nachgewiesen [3]. Dabei zeigte sich für einen radial polarisierten Laserstrahl eines CO_2 -Lasers im Dauerstrichbetrieb eine Verbesserung des Schneidprozesses, verglichen mit der Verwendung eines Laserstrahls mit zirkularer Polarisation. In Abhängigkeit vom bearbeiteten Material, konnte dadurch entweder die Bearbeitungsgeschwindigkeit um 50 % erhöht werden, die Qualität des Schnittes wurde verbessert oder weniger Edelgas wurde für den Prozess benötigt. Kurz darauf wurden am IFSW Experimente mit einem radial polarisierten CO_2 -Laser mit Laserleistungen bis

zu 3 kW durchgeführt. Dabei konnten vergleichbare Ergebnisse für weitere Materialien und Prozesse erzielt werden. Zum Beispiel konnte die Bearbeitungsgeschwindigkeit beim Laserstrahlschweißen um 33 % erhöht werden, ohne dabei die Spritzerbildung zu verstärken.

Bereits 2007 wurden die Vorteile einer azimutal polarisierten LG_{01}^* Mode für das Laserstrahlbohren mittels eines gepulsten Lasers untersucht [5]. Dabei kam ein Gütegeschalteter Nd:YAG Laser zum Einsatz, der Nanosekunden-Pulse erzeugte. Verglichen mit der Anwendung linearer oder zirkularer Polarisation, konnten in Abhängigkeit von der Dicke des bearbeiteten Materials, 1,5 bis 4 mal höhere Bohrgeschwindigkeiten erzielt werden. Vergleichbare Vorteile wurden außerdem beim Bohren von Mikrolöchern mit einem gepulsten Yb:YAG System nachgewiesen [13]. Dabei zeigten sich, je nach Dicke der bearbeiteten Bleche, Vorteile für Laserstrahlen mit radialer (für Blechdicken unter 0,5 mm) oder azimutaler (für Blechdicken über 1 mm) Polarisation. Die Vorteile dieser speziellen Strahl- bzw. Polarisationsformen beschränken sich dabei nicht ausschließlich auf die Bearbeitung von Metallen. So wurde beispielsweise gezeigt, dass das Bohren von Mikrolöchern in SiO_2 und reines Silizium die höchste Effizienz unter der Anwendung eines azimutal polarisierten Laserstrahls aufweist [14]. Bei den Versuchen kam ein modengekoppelter Ti:Sa-Laser zum Einsatz. Weitere Untersuchungen wurden zum Bohren in Karbonfaserverstärktes Plastik durchgeführt. Im Vergleich mit einem azimutal polarisierten oder unpolarisierten Strahl, konnte mit einem radial polarisierten eine 10-fach höhere Bohrgeschwindigkeit erzielt werden [15]. Eine weitere interessante Anwendung ist zudem die Strukturierung von Oberflächen mittels Laserpulsen mit azimutaler Polarisation. So bilden sich durch die Bearbeitung Strukturen im Mikro- und Nanometerbereich aus, die zu neuen Anwendungen führen könnten [16].

Da trotz der positiven und vielversprechenden Ergebnisse im Bereich der Materialbearbeitung mit gepulsten Lasern mit axial-symmetrischer Polarisation keine Systeme mit großer Ausgangsleistung vorhanden waren, förderte die europäische Union ab 2013 das Projekt RAZIPOL [17]. Das Projekt hatte das Ziel, diese Form von Laserstrahlung bei mehreren 100 Watt Ausgangsleistung zu erzeugen, um ein effizientes, großflächiges Bearbeiten von Oberflächen und das Bohren von Löchern mit großen Aspektverhältnis zu untersuchen. Zu diesem Zweck wurde eine Verstärkerkette bestehend aus einem Seedlaser, drei sogenannten "Single-Crystal Fiber" (SCF) Verstärkern und einem finalen Scheibenlaser-Multipassverstärker aufgebaut. Die radiale bzw. azimutale Polarisation wurde mittels eines Polarisationskonverters erzeugt. Bei einer korrekten Ausrichtung wandelt dieser einen einfallenden, linear polarisierten Gausstrahl in den gewünschten CVB um. Obwohl die in RAZIPOL gezeigten Resultate beeindruckend sind, zeigte sich, dass das Seedsystem vor dem Multipassverstärker aufgrund seiner hohen Komplexität zu

einigen Problemen führen kann. So stellte sich vor allem die Stabilisierung des Seedlasers als sehr herausfordernd dar. Auch die Qualität der radialen bzw. azimutalen Polarisation genügte regelmäßig nicht den erwarteten Ergebnissen.

Aus diesem Grund war das Ziel der vorliegenden Arbeit, ein System zu entwickeln, welches alternativ als Seedquelle genutzt werden könnte. Dabei lag der Fokus auf einer Verringerung der Komplexität des Systems und einer hohen Qualität der Intensitätsverteilung und der Reinheit der radialen Polarisation des erzeugten Strahls. Letztere beeinflusst maßgeblich das Ergebnis nach dem Multipassverstärker. Um als Seedquelle für den Multipass-Verstärker sinnvoll einsetzbar zu sein, musste zudem eine Ausgangsleistung von mindestens 50 W erzielt werden.

Um das gewünschte Ziel zu erreichen wurde eine Kombination aus einem modengekoppelten Oszillator mit radialer Polarisation und einem einzelnen, nachfolgenden SCF-Verstärker gewählt. Aufgrund der Leistungsskalierbarkeit des Konzepts wurde die Scheibenlasertechnologie für den Oszillator gewählt. Der modengekoppelte Betrieb wurde durch den Einsatz eines sättigbaren Absorberspiegels (Semiconductor saturable absorber mirror - SESAM) erlangt. Zur Erzeugung der radialen Polarisation des Lasers wurde ein am IFSW schon länger zum Einsatz kommender Ansatz gewählt. Dieser lag in der Verwendung von dielektrischen Gitterspiegeln, die den Beugungseffekt der optischen Gitter mit einem Wellenleitereffekt in der dielektrischen Schichtstruktur des Spiegels kombinieren. In Abhängigkeit der Polarisation des einfallenden Lichts, kann durch eine geeignete Wahl der Strukturparameter des Gitters wie Periode, Tiefe und Füllfaktor und die Dicke der dielektrischen Schichten die spektrale Reflektivität des Bauteils beeinflusst werden. Bis zum Beginn der Arbeit wurden diese Bauteile in Kombination mit einem herkömmlichen Auskoppler als Endspiegel der Kavität verwendet. Aufgrund des gewünschten modengekoppelten Betriebs bei gleichzeitiger radialer Polarisation des Laserstrahls, musste der Gitterspiegel erstmals als Auskoppler fungieren. Dies war notwendig, da der sättigbare Absorberspiegel ebenfalls als Endspiegel der Kavität eingesetzt werden muss, um eine stabile Modenkopplung, zu gewährleisten. Die so, am IFSW, zum ersten Mal gleichzeitig als Auskoppler verwendete Gitter-Wellenleiterstruktur wird "Grating Waveguide Output Coupler" (GWOC) genannt. Um den gewünschten Auskopplungsgrad zu erzielen, mussten die Strukturparameter des Gitterspiegels angepasst werden. Zur Verstärkung des Ausgangsstrahls wurde wie eingangs erwähnt eine SCF-Verstärker gewählt. Verglichen mit den Verstärkern im RAZIPOL-Projekt wurde ein Kristall mit einer niedrigeren Dotierung verwendet, um einen negativen Einfluss der thermischen Effekte im Verstärkerkristall auf die Qualität des verstärkten Strahls zu vermeiden.

Mit dem gewählten Ansatz konnte der weltweit erste modengekoppelte Scheibenlaser mit

radialer Polarisation demonstriert werden. Bei einer maximalen Pumpleistung von 61 W lieferte das System eine Ausgangsleistung von 13.3 W. Die maximale Ausgangsleistung war durch das Auftreten von Instabilitäten des Betriebs bei höheren Pumpleistungen begrenzt. Die Pulsrepetitionsrate des Systems betrug 42.1 MHz, was zu einer Pulsenergie von 316 nJ führte. Unter der Annahme eines sech²-förmigen Pulses wurden eine Pulsdauer von 907 fs und eine daraus resultierende Pulsspitzenleistung von 0.31 MW ermittelt. Damit erreichte das System die höchste bis zu diesem Zeitpunkt demonstrierte Ausgangsleistung und die gleichzeitig kürzeste Pulsdauer eines Oszillators mit axial-symmetrischer Polarisation. Im Bereich der Pulsenergie wurden zuvor nur gütegeschaltete Systeme mit höheren Werten gezeigt. Der Strahl wies gleichzeitig eine, bei einem solchen System bis zu diesem Zeitpunkt noch nicht gezeigte, nahezu ideale doughnutförmige Intensitätsverteilung auf und erreichte einen sehr guten "Degree of radial polarization" von 97 ± 1 % (gibt die Qualität bzw. Reinheit der Polarisation an). Für die Beugungsmaßzahl wurden Werte $< 2,1$ gemessen.

Für den zuvor erwähnten SCF-Verstärker wurde der Einsatz von Pumpquellen mit verschiedenen Emissionswellenlängen getestet. Die beiden verwendeten Systeme wiesen Wellenlängen von nominell 940 nm bzw. 969 nm auf. Dabei zeigte sich überraschenderweise unter Verwendung der 940 nm Diode eine höhere maximale Ausgangsleistung von 69.7 W bei einer Pumpleistung von 482 W, verglichen mit einer Ausgangsleistung von 66.3 W bei einer Pumpleistung von 519 W unter Verwendung der 969 nm Diode. Die Pulsdauern nach der Verstärkung betrugen 1030 fs und 909 fs. Der Unterschied ist auf eine Änderung der Pulsdauer und der Repetitionsrate des Seedlasers zwischen den beiden Versuchen zurückzuführen. Diese betrugen im ersten Fall 938 fs bzw. 41.5 MHz und im zweiten Fall 800 fs bzw. 40.7 MHz. Damit lagen die entsprechenden Pulsenergien nach der Verstärkung bei $1.68 \mu\text{J}$ (940 nm) bzw. $1.63 \mu\text{J}$ (969 nm), mit entsprechenden Pulsspitzenleistungen von 1.48 MW bzw. 1.58 MW. Während die Versuche mit der ersten Diode zu besseren Verstärkungsergebnissen führten, zeigte sich bei den Versuchen mit der zweiten Diode eine bessere Langzeitstabilität der Ausgangsleistung. Trotz weiterhin sehr guter Werte der Beugungsmaßzahl von 2.1-2.4 zeigte sich in beiden Fällen ein leichter Astigmatismus und gewisse Verformungen des Ausgangsstrahls. Durch einen Phasenshift zwischen den orthogonalen Komponenten der Polarisation des Laserstrahls, hervorgerufen durch den Verstärkerkristall und ein nachfolgendes optisches Element, verfügte der Ausgangsstrahl zudem über eine sogenannte "Hybrid1"-Polarisation. Daher wurde für den Versuch mit der 969 nm Diode zusätzlich nachgewiesen, dass sich diese Polarisationsform, mittels einer Vorkompensation mit einem Halbwellenplättchen, wieder in die radiale Polarisation umwandeln lässt. Der Polarisationsgrad der Hybrid1-Polarisation betrug in den beiden Versuchen 96.4 ± 1 % bzw. 96.1 ± 1 %. Mit Hilfe des Halbwellen-

plättchens konnte im letzteren Fall zudem eine radialer Polarisationsgrad von $94.1 \pm 1 \%$ erreicht werden, ohne dabei die anderen Betriebsparameter negativ zu beeinflussen. Trotz der leichten Verschlechterung der Strahlparameter, liegen sowohl die Beugungsmaßzahl, als auch die Reinheit der Polarisation in einem sehr guten Bereich. Somit konnte das Ziel der Entwicklung eines alternativen Seedsystems mit reduzierter Komplexität und guter Strahlqualität in weiten Teilen erfüllt werden.

1 Introduction

During the last decades, the cylindrical vector beams (CVB) with their anisotropic axially symmetric polarization state have gained a lot of attention. Especially the LG_{01}^* ¹ mode, with its doughnut-shaped intensity distribution, has been proven to be useful in various applications. For example, it is an interesting tool for particle trapping and the excitation of surface plasmons in rotationally symmetric structures [1]. Furthermore, it has been shown that a radially polarized LG_{01}^* can be focussed to extremely small spot sizes using optics with a high numerical aperture (NA). In case of a sufficiently large NA the focal spot size can become significantly smaller than theoretically possible with a linearly polarized beam² [6, 7]. This effect is caused by a longitudinal z-component of the electric field in the vicinity of the waist of the focussed beam. This component evolves in the center of the beam and can carry a large amount of the power of the laser. A CVB with azimuthal polarization does not exhibit this feature and keeps its doughnut shape in the proximity of the beam waist. Theoretically, this can be used for spatial focus engineering by adjusting the ratio of radial and azimuthal polarization within a beam [8]. In addition, in case of pulsed laser beams with extremely large peak powers the acceleration of particles such as electrons [2, 9], ions [10], and protons [11] becomes an interesting topic.

The beneficial properties specifically for laser material processing applications were theoretically outlined in 1999 by Niziev and Nesterov [12]. They predicted an increased cutting speed when using radially polarized laser beams instead of laser beams with a linear or circular polarization state. For some materials the hypothesis was proven to be correct in 2010 by Endo [3]. The radial polarization of a 2 kW beam of a CO₂ laser in continuous wave (CW) operation led to an improved cutting performance compared to results obtained with circular polarization. Depending on the processed material, either the cutting speed could be increased by up to 50 %, the cutting quality improved or less inert gas was required. Shortly afterwards, the application department at the IFSW conducted experiments with a radially polarized CW CO₂ laser with even larger average powers of up to 3 kW. They were able to demonstrate comparable tendencies for

¹The abbreviation LG is supposed to indicate that the intensity distribution is similar to that of a Laguerre-Gaussian mode, even though the LG_{01}^* mode is actually a superposition of two Hermite-Gaussian modes as will be shown in Chapter 4.

²If the spot size of the beam is defined via the FWHM width of the intensity distribution.

further materials and processes [4]. For example, they showed an increase of 33 % in the allowable feed rate for welding with minimum spattering.

Already 2007 Meier et al. experimentally investigated the benefits of pulsed CVB laser beams for drilling applications using a Q-switched (QS) Nd:YAG laser that delivered nanosecond pulses [5]. Depending on the thickness of the metal sheets, they achieved 1.5 - 4 times faster drilling speeds as compared to results obtained with linear and circular polarization. Comparable results were demonstrated for the drilling of deep micro-holes in metal sheets with azimuthally (sheet thickness ≥ 1 mm) and radially (sheet thickness ≤ 0.5 mm) polarized picosecond pulses generated by an Yb:YAG laser [13]. The beneficial properties of pulsed CVBs for laser material processing are not restricted to metals. For instance, drilling micro-holes into SiO₂ and pure Si substrates is most efficient when an azimuthally polarized beam is used, as was shown with a mode-locked TiSa laser in [14]. The results of an investigation regarding drilling of holes in carbon fiber reinforced plastic with a pulsed (3 Hz) CO₂ laser were reported in [15]. A 10 times higher drilling speed could be achieved using azimuthal instead of radial or random polarization. Another interesting topic is the structuring of surfaces with pulsed CVBs. Their intensity and polarization distribution lead to special structures on the micro- and nanometer scale, which might be used for new applications in the future [16].

As a result of these various promising applications and results, the development and investigation of laser sources generating these special types of laser beams is an ongoing process.

2 State of the art

The idea to build a laser is based on the extension of microwave techniques to the optical regime [18]. Interestingly, the same accounts for the generation of CVBs. In 1964 Marcatili and Schmeltzer predicted, that in a hollow circular waveguide a wave with azimuthal polarization would experience the lowest propagation losses [19]. This led to the very first demonstration of an azimuthally polarized ruby laser by Pohl in 1972 [20]. Pohl utilized the birefringence of a calcite crystal to lift the degeneracy of the modes with radial and azimuthal polarization in his laser cavity. In the same year Mushiake et al. showed the results of the first radially polarized gas (HeNe) laser [21]. The radial polarization state of the output beam was achieved by means of a conical end mirror with different reflectivities for incident s- and p-polarized light.

Even though Mushiake et al. stated that they didn't have "any practical suggestions about the application of the radially polarized mode" at the time, it is obvious that plenty of ideas have been developed since then. As will be shown in the following, the same accounts for the techniques to generate this special type of beams. These techniques can be divided into intra- and extra-cavity approaches. The first subsection of this section is dedicated to the intra-cavity approaches. The second subsection, presenting some examples of intra-cavity techniques, will first focus on CW and afterwards on pulsed oscillator systems. Finally, the third subsection is dedicated to publications dealing with the amplification of CVBs. While the list of systems is by far not comprehensive, it is supposed to give the reader a good overview of the most common approaches and the ones most suited to build high-power systems.

2.1 Extra-cavity generation of CVBs

Numerous ways to generate CVBs outside a laser cavity have been demonstrated during the last decades. A general approach implemented in various fashions is to coherently combine two beams with orthogonal polarization. The local intensity of one beam has to have a $\cos^2(\theta)$ and the other one a $\sin^2(\theta)$ dependence on the azimuth angle θ . Such an approach, starting with a linearly polarized fundamental mode laser is e.g. described in [22]. In general, such an approach is rather complex as it is necessary to first create the

two beams. More simple are the approaches with which one can transform an incident linearly polarized fundamental mode into a CVB by means of a single device. Such a device rotates the local polarization at each point of the cross-section of an incident beam, such that the beam has a global axially symmetric polarization state after it is reflected by or transmitted through the device. For instance, in 1996 Stalder and Schadt proposed a device that uses the twisted nematic effect of liquid crystals to rotate the local polarization accordingly [23]. A device based on the published approach has been commercialized by ARCOptix S.A [24]. The disadvantage of using the liquid crystal based approach is the comparatively small damage threshold of 200 mJ/cm^2 for 10 ns pulses at a wavelength of 1064 nm. For comparison, the super-structured wave plate (s-waveplate) commercially available from ALTECHNA offers an approximately 100 times higher damage threshold for comparable laser beam parameters [25]. The rotatory effect of the s-waveplate is achieved by writing self-assembled nanostructures in silica glass using a femtosecond laser [26]. The local orientation of the birefringence acting on a transmitted beam is controlled via the polarization of the femtosecond laser. Such a device was tested at the IFSW with picosecond pulses up to an incident average power of 700 W at a wavelength of 1030 nm. Due to reflection and diffraction losses the transformation efficiency was limited to approximately 78 %. A different device consists of several half-wave plate segments. Each of these segments rotates the linear polarization of an incident beam by a certain angle to produce a CVB. The first reported device based on this effect consisted of only four segments [7]. This ultimately limited the conversion efficiency. Therefore, later such devices with up to eight segments were developed [27]. At the IFSW, such segmented half-wave plates were successfully qualified with up to 8 kW of incident CW power at a wavelength of 1030 nm and with up to 200 W at 515 nm. Additionally, at a wavelength of 1030 nm the segmented half-wave plate was tested with sub-picosecond pulses with up to 350 W of incident average power without causing any damages. This proves the ability of the device to withstand high powers of ultrashort laser pulses. Unfortunately, all these polarization converters suffer from one major problem, which is the diffraction of the incident beam at the nano-structures or the boundaries between the wave plate segments, respectively. This results in the necessity to clean up the beam after the converter, which causes losses $\geq 10 \%$. Moreover, cleaning up the beam at high power levels can become extremely challenging.

2.2 Intra-cavity generation of CVBs in continuous wave operation

One way to circumvent the problems arising from the diffracted beam parts is to set up a laser that directly generates a CVB. A common practice to do so, especially in case of rod lasers, is to exploit the thermally induced birefringence in strongly pumped isotropic laser crystals [28, 29]. Due to the radial cooling scheme the stress tensors, and therefore the birefringence, are axially symmetric and can be divided into radial, tangential, and axial contributions [30]. This results in a difference of the thermal focussing effect for radially and azimuthally polarized beams. Thus, in case the resonator is properly designed, a mode with only one of the two polarization states will start to oscillate. The highest average output power achieved with an oscillator exploiting this effect was reported by Moshe et al. in 2003 [31]. They demonstrated a radially polarized Nd:YAG rod laser with an average output power of 70 W with a high polarization purity and a M^2 -value of 2. At the expense of a slightly worse M^2 -value of 2.3 and 2.7 the group was later able to increase the output power of such an oscillator system to up to 180 W and 200 W of average output power for beams with radial and azimuthal polarization [32]. As these kinds of systems rely on the thermally induced birefringence in the laser rod, they only work for certain pump power levels. Another approach, comparable to that used by Mushiake et al. in 1972 [21], was employed by Endo to demonstrate up to 2.1 kW of radially polarized emission from a CO₂ laser [3]. He replaced the cavity end mirror with a so-called triple axicon. This device first of all led to the oscillation of a doughnut-shaped mode. The radial polarization state of the laser mode was obtained by means of the coating of the triple axicon, which exhibited a polarization dependent reflectivity. A detailed description of the device and its functionality was already published in 2008 [33]. Lately, a similar device in conjunction with four quarter-wave phase retarders was used by another group to generate up to 1.5 kW of average output power from an azimuthally polarized CO₂ laser [34]. In 2006 Moser et al. published the results of a CO₂ laser emitting 45 W of radially polarized light [35]. They used an anti-reflection (AR) coated GaAs substrate with a binary centrosymmetric diffraction grating on the backside as a cavity end mirror. The parameters of the grating were optimized such that incident radially polarized light coupled to the zero-order reflection of the device, whereas azimuthally polarized light was mainly transmitted. At the IFSW 2.7 kW of average output power from a radially polarized CO₂ laser were demonstrated in 2007 in a collaboration with TRUMPF GmbH [36]. This was achieved by using a GaAs substrate with a multi-layered mirror and a sub-wavelength grating on top as the cavity end mirror. Due to coupling of azimuthally polarized light to leaky modes in the multi-layers the reflectivity for radially

polarized light was larger. Lately, researchers of the IFSW additionally demonstrated up to 670 W of average output power from a radially polarized Yb:YAG thin-disk laser at a wavelength of 1030 nm [37]. The polarizing device consisted of alternating corrugated layers of SiO₂ and Ta₂O₅ on a fused silica substrate. This is currently the record in terms of average output power for intra-cavity generated CVBs in the wavelength range around 1 μ m. At moderate output power levels, there are even more systems reported that are based on the combination of diffractive sub-wavelength structures and waveguiding effects [38–40]. Thereof the results published in [40] are particularly interesting from another point of view. While the average output power only reached 2.7 W, it was the first time that such a structure was used as an output coupler in a laser generating a CVB. As will be shown later, the possibility to use such a device as an output coupler was extremely important to achieve the results which are presented within this work.

2.3 Intra-cavity generation of CVBs in pulsed operation

All the oscillator systems introduced so far were operated in CW. Even though already the very first CVB laser demonstrated by Pohl in 1972 could be used either in QS or mode-locked (ML) operation [20], there are only few publications on pulsed oscillators generating CVBs. The corresponding pulse durations were 70 ns and 1 ns, respectively. Pulsed operation was achieved by means of a cryptocyanine-methanol bleachable absorber. After that, it took almost 35 years until the next pulsed CVB laser was mentioned. In 2007, Meier et al. demonstrated 4.6 W of average output power generated by a QS Nd:YAG rod laser. CVB emission with radial polarization was obtained by exploiting the thermally induced birefringence of the laser rod. The system generated 80-100 ns long pulses using an acousto-optic modulator (AOM). In 2009 Enderli and Feurer reported on the first generation of CVBs with pulse durations in the sub-nanosecond range, namely 140 ps [41]. They achieved an average output power of 3 W. Once more, the radial polarization was obtained by exploiting the thermally induced birefringence in the laser crystal and the pulsed operation by means of an AOM. Since then, the highest average output power demonstrated for a pulsed CVB, generated intra-cavity, was 10.6 W with a pulse duration of 75 ps [42]. The shortest pulse duration of 15.6 ps at an average output power of 2 W was achieved by Li et. al in 2013 [43]. In both systems a saturable absorber was used to obtain ML operation. Various other systems generating pulsed CVBs inside the cavity have been reported [44–46]. However, most of these systems do not even reach the Watt power level.

2.4 Amplification of CVBs

In 2010 Moshe et al. amplified a doughnut-shaped CVB (CW, $M^2 = 2.5$) with azimuthal polarization and an average power of 60 W to up to 1625 W of average output power [47]. They used three subsequent Nd:YAG rod amplifiers each pumped with 6 kW of average power. At the cost of a decreased beam quality, up to 4 kW of average output power were achieved with 550 W of seed power. Kanazawa et al. demonstrated the amplification of a 1 W radially polarized CW seed beam up to 21 W using an Yb-doped double clad fiber. However, the polarization of the output beam suffered from a strong distortion that was attributed to birefringence in the fiber core [48]. In 2013 the IFSW in collaboration with the Institut d'Optique in Paris and Fibercryst SAS demonstrated the amplification of CVBs in an Yb:YAG single-crystal fiber (SCF) amplifier [49]. A radially as well as an azimuthally polarized seed beam were successfully amplified from 33 W to up to approximately 100 W of average output power. In both cases a high polarization purity was maintained.

Due to the disparity between the promising properties for laser material processing and the limited amount of available experimental data on the matter, the European Union supported the project RAZIPOL, which started in 2013 [17]. The aim of the project was to generate sub-picosecond CVB pulses and to reach output powers in the range of several hundred Watts by means of cascaded SCF and thin-disk multipass (TDMP) amplifier stages. In a preceding test with a commercial seed laser (TruMicro5050), the radially polarized seed with a power of approximately 100 W was successfully amplified to up to 625 W of average output power in a TDMP amplifier system [50]. The polarization purity of the 6.5 ps pulses was well maintained, proving the potential of the TDMP amplifier concept for the amplification of CVBs. In a first test of the preamplifier system, a linearly polarized Gaussian seed beam with an average power of 1.5 W (20 MHz, 260 fs pulse duration) was amplified up to 72 W of average power in two SCF-based (double-pass) preamplifier stages. Subsequently, the fundamental mode was transformed into a radially polarized CVB by means of a SWP. Transmission losses and the necessary beam clean-up after the SWP led to a decrease of the average power down to 55 W. In a third SCF (single-pass) stage these 55 W (727 fs pulse duration) were amplified to up to 86 W (740 fs pulse duration) of average power [51]. A comparable system, with the SWP after the last amplifier stage, was finally used to seed the TDMP amplifier with 50 W of average power (727 fs pulse duration) to obtain 265 W of average output power after the amplification (782 fs pulse duration). At this power level the doughnut-shaped intensity distribution and the radial polarization state of the CVB could be well maintained. A detailed description of the TDMP amplifier concept can be found in [52, 53].

3 Objective of this work

Even though the experiments within the RAZIPOL project were successful and led to impressive results, the seed system for the TDMP amplifier is complex with its three preamplifier stages and the SWP including the beam clean up. Hence, the long term stabilization of the system becomes a difficult task. Furthermore, the beam quality after the TDMP amplifier strongly depends on the quality of the seed beam, which often was not as good as expected. Figure 3.1 schematically shows the rather complex amplifier chain of the RAZIPOL system including the polarization states between the different stages, indicated by the black arrows. As a result, the aim of this work was to develop a new system that generates sub-picosecond pulses with a radial or azimuthal polarization state and an average output power of at least 50 W (based on the requirements of the TDMP system). The main focus was a high quality of the emitted CVB and a more simple approach than the preamplifier chain used in the RAZIPOL project.

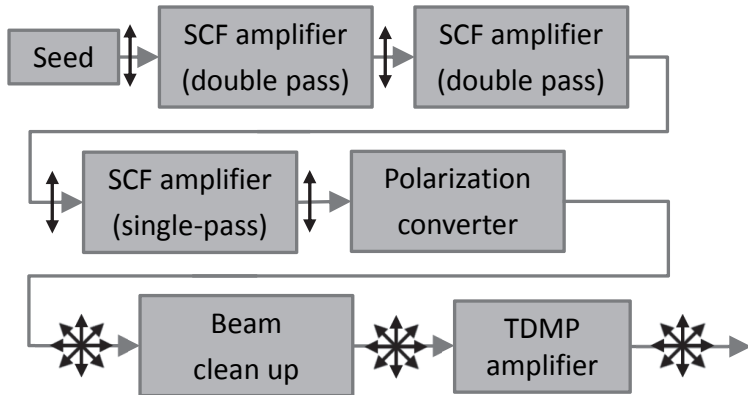


Figure 3.1: Graphical representation of the amplifier chain in the European project RAZIPOL. The black arrows indicate the polarization state of the laser beam at the respective position within the system.

3.1 Polarization state

From experience, CVBs directly generated by the oscillator reach a better beam quality and homogeneity of the intensity distribution than those generated by means of an extra-cavity approach. Looking at results shown in Section 2.2 and Section 2.3, especially the systems based on grating-waveguide structures [36–40, 54] furthermore led to systems with good results in terms of average output powers. Such a device can simply be used as a cavity end mirror without any additional restrictions to the cavity design. On the other hand, for approaches employing thermally induced [28, 29, 31, 32] or intrinsic [20] birefringence, the generation of the CVB either affords an additional transmissive component in the cavity, or the polarizing effect is coupled to the geometry and the crystallographic structure of the laser crystal. The triple-axicon mirror approach, which also led to good results, was so far only demonstrated for CO₂ lasers [3] and the complexity of the production of such a device is unclear. Therefore, a grating-waveguide based component was considered the best approach for the system presented in this work.

Throughout the literature different designs for grating waveguide structures can be found. The structures for which a reasonable average output power has been demonstrated or at least appears to be viable have already been introduced in Section 2.2 and Section 2.3. Of these approaches the one used in [54] already relies on very small structures if produced for the application in CO₂ lasers. If this approach would be transferred to lasers with a wavelength in the range of 1 μm , the production of the devices would become problematic. The approach of Zhao et al. relies on nano-pillars in the grooves of the grating [39]. This probably makes the production of the devices already complex for lasers in the 10 μm range and even more if the approach is transferred to shorter wavelengths. The design used in [38] and [40] both seem reasonable to produce and both were already used in a suitable wavelength range. Nevertheless, both do not possess any major advantage in comparison to the shallow and easy to produce devices so far developed and used at the IFSW. Thus, as result of the previously demonstrated good results and the available extensive experience, the device used to generate the CVBs was supposed to be based on the corrugated multilayer design generally used at the institute.

3.2 Pulsed operation

In general, most lasers generating ultrashort pulses are either mode-locked using the Kerr self-focusing effect in conjunction with a soft or hard aperture (see e.g. [55]) or by means of a semiconductor saturable absorber mirror (SESAM) (see e.g. [56]).

As Kerr lens mode-locking of a CVB has not yet been demonstrated and as the Kerr self-focusing effect caused by the doughnut-shaped intensity distribution of the CVBs is not as simple as that of a Gaussian beam, SESAM mode-locking was the chosen approach to generate the ultrashort pulses in the experiments presented throughout this work. As such a SESAM has to be used as an end mirror of the cavity to obtain stable mode-locked operation, the grating waveguide structure additionally had to act as the output coupler. Therefore, adjustments to the existing grating-waveguide designs were necessary.

3.3 Laser technology

As the system was meant to be power scalable on the long run, either the fiber [57], the slab [58], or the thin-disk [59] technology would have been suitable approaches. Nevertheless, the use of the thin-disk approach has several advantages compared to the fiber and slab technologies. First of all, due to the much larger beam diameter and the short propagation length in the laser medium, detrimental non-linearities, as a result of the pulsed operation, start to become a problem at higher pulse energy levels than in fiber and slab lasers. Secondly, due to the short interaction length between the disk and the light beam, the laser medium does not affect the polarization state of the CVB, while in general the propagation of such complex modes is more difficult in fibers. The same accounts for slabs if astigmatic focusing is used to obtain a good overlap of the laser and the pump light [60]. Such an astigmatic focussing induces a phase shift between s- and p-polarized light, which would have to be compensated to obtain a high polarization purity.

If the 50 W of average output power, required for a seed beam of a TDMP, could not be obtained simply by the oscillator setup, an appropriate amplification was to be considered. As the fiber and slab technology exhibit the already mentioned disadvantages for pulsed systems generating a CVB, they were excluded as a useful possibility. A classical rod amplifier would circumvent the problems of nonlinearities, but due to the bad overlap between the pump light of a standard low brightness diode and the seed beam, the efficiency would be extremely low. Thus, the most promising choice was the use of a SCF amplifier, like in the original setup. As average output powers in the range of at least 10 W were expected to be feasible from the oscillator system, the amplifier approach published in [49] was supposed to be a good solution. In the reported system, a SCF with a doping concentration of only 0.5 at. % was used. In comparison, SCF crystals with doping concentrations of 1 - 2 % were used in the project RAZIPOL. The lower doping concentration still leads to reasonable gain factors, while maintaining a high polarization

purity due to a low thermal stress in the crystal.

Figure 3.2 shows the planned seed system with the optional amplifier and the subsequent TDMP. The black arrows indicate the polarization state of the laser beam at the respective position within the system.

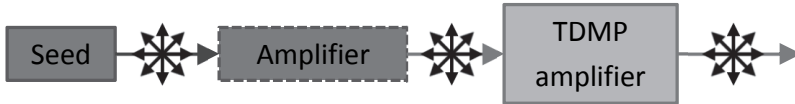


Figure 3.2: Graphical representation of the planned seed system and the subsequent TDMP. The black arrows indicate the polarization of the laser beam at the respective position within the system.

4 Cylindrical vector beams

The mathematical basis for CVBs is outlined in the first section of this chapter. Particularly the difference between CVBs and vortex beams is highlighted as the separation is often not precise throughout literature. The second section is dedicated to the evaluation of the polarization purity of the CVBs. Some methods to quantitatively assess this value are introduced to make the reader aware of the challenges which arise when comparing the values in different publications. Within this last section, the camera-based 2D-polarimeter, used throughout the experiments presented in this work, is thoroughly outlined.

4.1 Vortex versus cylindrical vector beams

Throughout the literature the Laguerre-Gaussian (LG) vortex beams and the doughnut-shaped CVBs with their axially symmetric polarization distribution are often not clearly separated, especially regarding the vortex nature [61]. In some cases the cylindrical vector

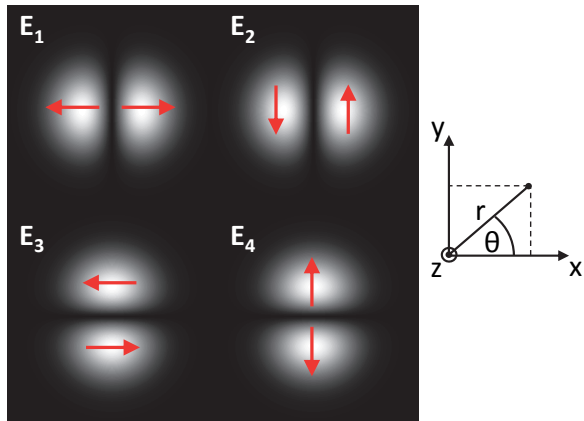


Figure 4.1: Graphical representation of the four basic HG modes $E_1 - E_4$ used to construct the CVBs including the instantaneous direction of the electric field indicated by the red arrows.

beams are e.g. described as the superposition of several vortex beams with opposite orbital charge and probably therefore treated as vortex beams even though the helical nature of the phase front is lost [62]. Another reason for the unclear separation could be the inconsistent discrimination of the terms LG_{01} and LG_{01}^* , where the LG_{01}^* notion should be used for the most fundamental CVBs. The term was introduced to point out that the intensity distribution of these beams is similar to that of the LG_{01} mode while at the same time it does not belong to the group of real LG modes. The full electric field of the LG_{01}^* mode is rather described as a superposition of two Hermite-Gaussian (HG) modes H_{01} and H_{10} with opposite polarization [30].

The Laguerre-Gaussian and the Hermite-Gaussian modes with a homogeneous polarization orientation across their cross-section are solutions to the scalar paraxial wave equation in cylindrical and rectangular coordinates, respectively. The electric field of the Laguerre-Gaussian modes at the azimuth angle θ and the distance r from the beam axis is thereby given by [63, 64]

$$E_{pl}(r, \theta, z) = A \frac{w_0}{w(z)} \left(\frac{r\sqrt{2}}{w(z)} \right)^l L_p^l \left(\frac{2r^2}{w^2(z)} \right) e^{-\frac{r^2}{w^2(z)}} \times e^{\frac{ikr^2}{2R(z)}} e^{-i[(2p+l+1)\zeta]} e^{il\theta}, \quad (4.1)$$

wherein A is a constant, p and l are the orders of the LG mode, w_0 is the beam radius

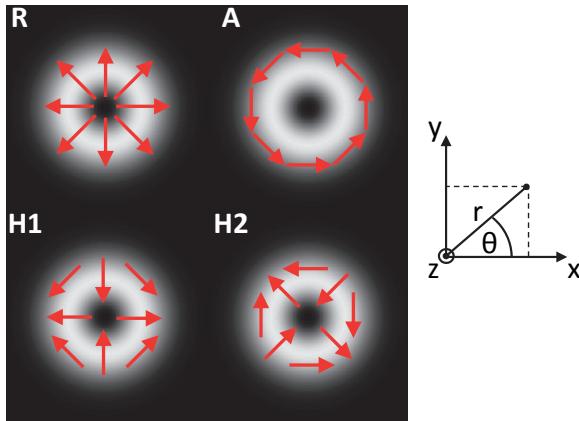


Figure 4.2: Graphical representation of a radially (R) and azimuthally (A) polarized beam as well as the two hybrid modes H1 and H2. The instantaneous direction of the electric field is indicated by the red arrows.

at its waist, $w(z)$ is the beam radius at the distance z from the beam waist, and $R(z)$ is the radius of curvature (ROC) of the phase front. The angular wavenumber is given by $k = \frac{2\pi}{\lambda}$, wherein λ is the wavelength. The so-called Gouy phase ζ depends on the Rayleigh range of the beam and describes the part of the phase shift a Gaussian beam acquires that differs from a plane wave of the same wavelength, and $L_p^l \left(\frac{2r^2}{w^2(z)} \right)$ is the Laguerre polynomial, where $L_0^1(x) = 1$. The last term of the formula is responsible for the helical phase front of the LG modes with $l \geq 1$. The sign of the exponent determines the handedness of the helical phase front and each photon of such a beam carries an orbital angular momentum of $l\hbar$. In contrast to this, the electric field distribution of the HG modes at the Cartesian coordinates x and y , which are related to r in Eq. 4.1 by $r = \sqrt{x^2 + y^2}$, is described by [63, 64]

$$E_{mn}(x, y, z) = A \frac{w_0}{w(z)} H_m \left(\frac{x\sqrt{2}}{w(z)} \right) H_n \left(\frac{y\sqrt{2}}{w(z)} \right) e^{-\frac{r^2}{w^2(z)}} \times e^{\frac{ikr^2}{2R(z)}} e^{-i[(m+n+1)\zeta]}, \quad (4.2)$$

wherein m and n are the orders of the HG mode, and $H_m \left(\frac{x\sqrt{2}}{w(z)} \right)$ and $H_n \left(\frac{y\sqrt{2}}{w(z)} \right)$ are the related Hermite polynomials. The most important for this work is given by $H_1(x) = 2x$. By keeping in mind that $re^{i\theta}$ can be written as $r(\cos(\theta) + i\sin(\theta))$ it is obvious that the LG_{01} mode can be constructed by the superposition of two HG modes HG_{10} and HG_{01} , where it is necessary that both modes have the same polarization and a phase difference of $\pi/2$. Hence, the electric field of the superposition can be written as $E_{10} + iE_{01}$.

Both sets of modes are linearly polarized. But as outlined before we are interested in the CVBs with their anisotropic polarization states. These do not necessarily have to be Gaussian [65] and can be described in a general form as spirally polarized beams [66, 67]. However, the present work concentrates only on CVBs which can be mathematically described as a coherent linear combination of the four HG modes depicted in Figure 4.1. The magnitude of the electric fields of the modes $E_1 - E_4$ at the beam waist ($z = 0$) with w_0 being $w(z = 0)$ are given by

$$\begin{aligned} E_1 &= E_{10}(r, \theta, 0) \hat{x} = \cos(\theta) \frac{r}{w_0} e^{-\frac{r^2}{w_0^2}} \hat{x}, \\ E_2 &= E_{10}(r, \theta, 0) \hat{y} = \cos(\theta) \frac{r}{w_0} e^{-\frac{r^2}{w_0^2}} \hat{y}, \\ E_3 &= E_{01}(r, \theta, 0) \hat{x} = \cos(\theta) \frac{r}{w_0} e^{-\frac{r^2}{w_0^2}} \hat{x}, \\ E_4 &= E_{01}(r, \theta, 0) \hat{y} = \cos(\theta) \frac{r}{w_0} e^{-\frac{r^2}{w_0^2}} \hat{y}, \end{aligned} \quad (4.3)$$

with \hat{x} and \hat{y} being the unit vectors in x- and y-direction. The instantaneous direction of the electric field is indicated by the red arrows. The electric field of the four axially symmetric polarization states, relevant for this work, are given by

$$\begin{aligned}
 E_{1,RAH} &= E_1 + E_4, \\
 E_{2,RAH} &= E_2 + E_3, \\
 E_{3,RAH} &= E_1 - E_4, \\
 E_{4,RAH} &= E_3 - E_2
 \end{aligned}
 \tag{4.4}$$

and termed radial (R, $E_{1,RAH}$), azimuthal (A, $E_{2,RAH}$), hybrid1 (H1, $E_{3,RAH}$), and hybrid2 (H2, $E_{4,RAH}$) throughout this work, according to the nomenclature introduced in [68]. Different other notations, such as e.g. "anti-vortex" for the H1 and the H2 polarization, that refer to the same four polarization states can be found throughout the literature [62,69]. A schematic of the electric field distributions of the four states can be seen in Figure 4.2. The polarity of the electric field is indicated by the red arrows. It can be seen that only beams with a doughnut-shaped intensity distribution are discussed.

Expressing the CVBs as a coherent linear combination of the HG modes makes it clear that CVBs have no helical phase structure. To visualize the difference, Figure 4.3 shows the electric field of a linearly polarized LG_{01} (a) and a radially polarized LG_{01}^* (b) mode at one instance in time at different positions z along the beam propagation path. The instantaneous direction of the electric field is once more indicated by the red arrows. Obviously, for the LG_{01} mode two lobes of opposite polarity rotate around the propagation axis, which is a result of the helical phase front. On the other hand, the LG_{01}^* keeps its doughnut-shaped profile at each position along the beam propagation path. However, they cannot be distinguished by their time-integrated intensity distribution, as can be seen in the last row of Figure 4.3. Throughout this work, some evaluations are valid for both types of modes since the investigated effect depends only on the intensity distribution and not on the polarization state. In these cases the modes are solely described as doughnut-shaped. Otherwise, "CVB" or " LG_{01}^* " is written in the text to indicated the dependence on the anisotropic polarization state.

4.2 Evaluation of the polarization purity

As discussed in the last section, mainly the polarization distribution characterizes the quality and type of a given CVB. It is therefore necessary to correctly assess the polarization purity. A simple way to do so in a qualitative manner is to place a rotatable polarizer into

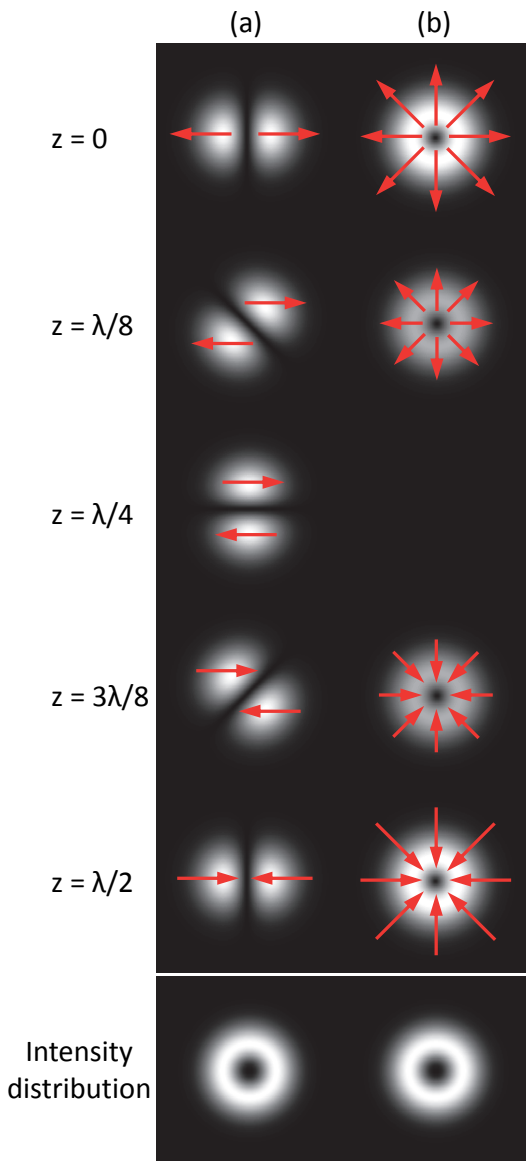


Figure 4.3: Comparison of the electric field of a linearly polarized LG_{01} (a) and a radially polarized LG_{01}^* mode (b) at one instance of time at different positions z along the beam propagation path. The instantaneous direction of the electric field is indicated by the red arrows. Additionally, the last row shows the similar intensity distributions of the two beams.

the beam path. While rotating the polarizer, two well separated lobes have to be observed behind it when analyzing a CVB. For an ideal radially polarized LG_{01}^* mode the two lobes will be aligned parallel to the polarization orientation of a beam transmitted by the polarizer as exemplarily depicted in Figure 4.4. For a beam with azimuthal polarization the two lobes will be aligned perpendicular to that orientation. For the H1 and H2 mode the lobes rotate against the rotation direction of the polarizer, thus the relative orientation of the lobes changes when the polarizer is rotated.

One of the major sources of degradation of the polarization purity of the CVBs are linear phase shifts occurring due to non-zero angles of incidence (AOI) on optical components such as e.g. mirrors. A non-zero AOI leads to a phase shift between the s- and p-polarized¹ components of the incident beam, respectively. Thus, the effect of this difference in the phase shift is only visible in areas of the beam cross-section where both components are non-zero. For a beam with one of the four polarization states ($E_{1,RAH} - E_{4,RAH}$) introduced in Section 4.1, this would mainly affect the electric field on the diagonals. Thus, such a phase shift would not be visible for a x- or y-orientation (compare to Figure 4.2) of the transmission axis of the polarizer.

¹By convention throughout this work the s- and p- polarization refer to light polarized orthogonal and parallel to the plane of incidence determined by the incident beam and the normal vector of an optical component (see also [64]). In case of an AOI of 0° p- is parallel to the plane of the lab table if not stated differently.

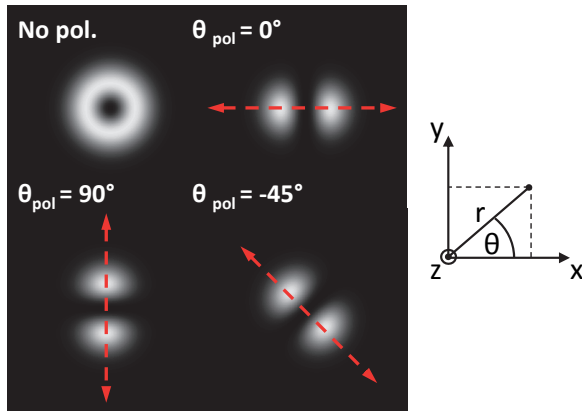


Figure 4.4: Radially polarized LG_{01}^* mode including the expected intensity distributions if a polarizer is placed into the beam path. The red arrows indicate the orientation angle θ of the orientation of the polarization of a beam transmitted by the polarizer.

To get a quantitative measure of the polarization purity there are different methods described throughout literature. In one method the power transmitted through a polarizer is determined for varying orientations (azimuth angles) of the device [35]. The lower the modulation of the signal the better is the polarization purity, and the polarization state is indicated by the orientation of the lobes of the transmitted beam relative to the orientation of the polarizer.

In another method, the polarizer is fixed in one orientation and an image of the transmitted beam is taken. Then the intensity $I(r, \theta)$ at a distance r from the beam center is plotted versus the angle θ relative to the orientation of the polarizer [70] as can be seen in Figure 4.5. The expected intensity for a radially polarized beam is given by $I(r, \theta) = I_{max} \cos^2(\theta)$. For an azimuthally polarized beam it is given by $I(r, \theta) = I_{max} \sin^2(\theta)$. The extinction ratio is used as a measure of the polarization purity. A problem with this method would occur, if e.g. the incident beam would have an H1 polarization with an orientation like in the example in Figure 4.2. Such a beam would also result in a radial polarization purity of 100 % even though the beam has a different polarization. In general, a major disadvantage of both approaches is that it is not possible to fully determine the polarization state in case of a mixture of $E_{1,RAH} - E_{4,RAH}$. Such a mixture could e.g. be the result of the phase shifts due to the already discussed non-zero AOIs on the mirrors in the system. However, such a phase shift can be easily compensated in case the exact polarization state is known.

This is one of the reasons why at the IFSW the polarization state is fully assessed with a camera-based 2D-polarimeter. As the device is essential for the classification of the demonstrated results, the setup and the calculation of the polarization state is thoroughly outlined in the following. Since the setup of the device was not part of this work, the information is to a large extent a summary of the respective part of the master thesis written by Frieder Beirow at the IFSW [71].

In [72] and [68] an extension of the Jones matrix formalism (see [64]) is introduced, that treats the four polarization states radial, azimuthal, H1, and H2 as base states with which each arbitrary axially symmetric polarization state of a doughnut-shaped mode can be described. The entries of the extended Jones vector \vec{J}_{ext} contains the magnitude A_{RAH} and the phase δ_{RAH} of all four states with

$$\vec{J}_{ext} = \begin{pmatrix} A_{1,RAH} e^{i\delta_{1,RAH}} \\ A_{2,RAH} e^{i\delta_{2,RAH}} \\ A_{3,RAH} e^{i\delta_{3,RAH}} \\ A_{4,RAH} e^{i\delta_{4,RAH}} \end{pmatrix}. \quad (4.5)$$

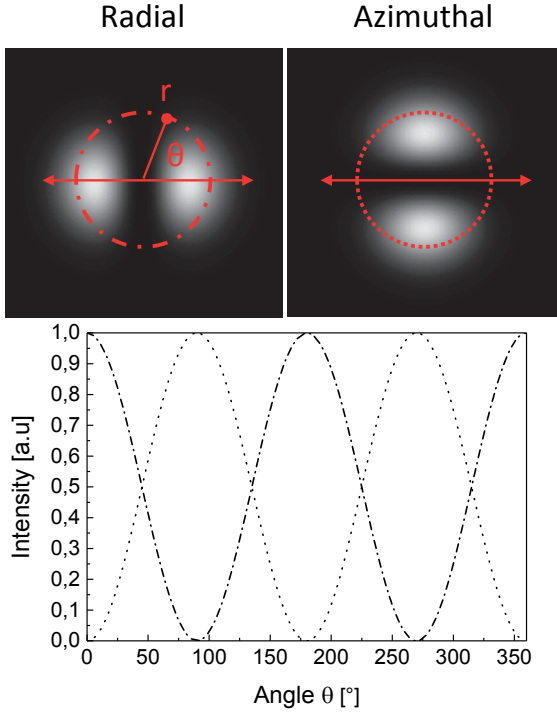


Figure 4.5: Intensity measured along the red circles for a radially (dash-dotted curve) and azimuthally (dotted curve) polarized beam which propagated through a polarizer. The orientation of the transmission axis of the polarizer is indicated by the arrows.

The respective degrees of radial (DORP), azimuthal (DOAP), hybrid1 (DOH1P) and hybrid2 (DOH2P) polarization are defined as

$$\begin{aligned}
 \text{DORP} &= \frac{|\vec{J}_{ext} \cdot (1 \ 0 \ 0 \ 0)^T|^2}{|\vec{J}_{ext}|^2}, \\
 \text{DOAP} &= \frac{|\vec{J}_{ext} \cdot (0 \ 1 \ 0 \ 0)^T|^2}{|\vec{J}_{ext}|^2}, \\
 \text{DOH1P} &= \frac{|\vec{J}_{ext} \cdot (0 \ 0 \ 1 \ 0)^T|^2}{|\vec{J}_{ext}|^2}, \\
 \text{DOH2P} &= \frac{|\vec{J}_{ext} \cdot (0 \ 0 \ 0 \ 1)^T|^2}{|\vec{J}_{ext}|^2}.
 \end{aligned} \tag{4.6}$$

The normalization of the values is necessary as the formalism also treats lossy elements, which result in $|\vec{J}_{ext}| \neq 1$, even though the sum of the degrees of polarization is defined to

be 1.

The 2D-polarimeter, which can measure these values, consists of a rotatable quarter-wave plate positioned in front of a polarizer and a CCD camera, as schematized in Figure 4.6. The polarization state of a partially polarized beam can be described via the four well-known Stokes parameters $S_0 - S_3$ and the effect of an optical component by the respective Mueller matrix [73]. Thus, if the polarization state of a beam incident on the 2D polarimeter is given by \vec{S} , the polarization state \vec{S}' in the plane of the camera can be written as [74]

$$\vec{S}'(\theta) = \begin{pmatrix} S'_0 \\ S'_1 \\ S'_2 \\ S'_3 \end{pmatrix} = M_{POL} \cdot M_{QWP}(\theta) \cdot \vec{S} = M_{POL} \cdot M_{QWP}(\theta) \cdot \begin{pmatrix} S_0 \\ S_1 \\ S_2 \\ S_3 \end{pmatrix}, \quad (4.7)$$

with M_{QWP} and M_{POL} being the Mueller matrices of the quarter-wave plate and the polarizer and θ the rotation angle between the axis of the polarizer, indicating the orientation of the transmitted polarization, and the slow axis of the quarter-wave plate. Expanding the function leads to

$$\begin{pmatrix} S'_0 \\ S'_1 \\ S'_2 \\ S'_3 \end{pmatrix} = \frac{1}{2} (S_0 + S_1 \cos^2(2\theta) + S_2 \sin(2\theta) \cos(2\theta) + S_3 \sin(2\theta)) \begin{pmatrix} 1 \\ 1 \\ 0 \\ 0 \end{pmatrix}. \quad (4.8)$$

The quarter-wave plate is mounted in a motorized rotatable stage. During the measurement the wave plate is rotated by 360° , while in parallel images of the beam are

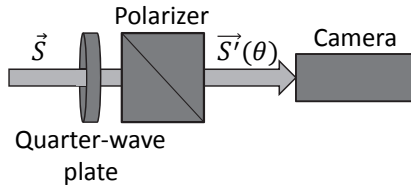


Figure 4.6: Schematic setup of the camera-based 2D polarimeter.

taken. The measured intensity at each pixel of the camera image is related to the Stokes parameters via $I(\theta) = S'_0(\theta)$. Some trigonometric conversion of Eq. 4.8 yields [74]

$$I(\theta) = \frac{1}{2}(A + B\sin(2\theta) + C\cos(4\theta) + D\sin(4\theta)) \quad (4.9)$$

$$\begin{aligned} A &= S_0 + \frac{1}{2}S_1, \\ B &= S_3, \\ C &= \frac{1}{2}S_1, \\ D &= \frac{1}{2}S_2. \end{aligned} \quad (4.10)$$

Hence, using a Fourier analysis the four coefficients can be calculated and the Stokes parameters at each point derived. The local electric field vector $\vec{E}(u, v)$ at the pixel positions u and v with the x- and y-components $E_x(u, v)$ and $E_y(u, v)$ ² and the phase shift δ between these components can subsequently be determined via the following formulae:

$$\begin{aligned} E_x(u, v) &= \pm \frac{1}{2} \sqrt{S_0(u, v) + S_1(u, v)} \\ E_y(u, v) &= \pm \frac{1}{2} \sqrt{S_0(u, v) - S_1(u, v)} \\ \delta &= \arctan(S_3(u, v)/S_2(u, v)) \end{aligned} \quad (4.11)$$

To improve the result of the calculation and to diminish the effects of noise, a region of interest is defined by means of a threshold intensity of the pixels. When the intensity on a pixel is below the threshold, it is not taken into account for the subsequent calculation steps. The center of the beam is determined via the center of gravity of the sum of all the images taken during the measurement. As soon as the beam center is defined, the normalized electric field vectors $\hat{E}_{rad}(u, v)$, $\hat{E}_{azi}(u, v)$, $\hat{E}_{h1}(u, v)$, and $\hat{E}_{h2}(u, v)$ at each pixel can be calculated for the ideal cases of a perfect radial, azimuthal, hybrid1, and hybrid2 polarization of the incident beam. In a next step, the projections p_{rad} , p_{azi} , p_{h1} , and p_{h2} of the normalized measured electric field vector $\hat{E}(u, v)$ onto these four ideal states are calculated for each pixel of the camera by

$$\begin{aligned} p_{rad} &= \hat{E}(u, v) \cdot \hat{E}_{rad}(u, v), \\ p_{azi} &= \hat{E}(u, v) \cdot \hat{E}_{azi}(u, v), \\ p_{h1} &= \hat{E}(u, v) \cdot \hat{E}_{h1}(u, v), \\ p_{h2} &= \hat{E}(u, v) \cdot \hat{E}_{h2}(u, v). \end{aligned} \quad (4.12)$$

²The orientation of the coordinate system is defined by the orientation of the camera, wherein the x-axis is parallel to the rows of pixels of the camera chip and the y-axis parallel to the columns.

The average values \bar{p}_{rad} , \bar{p}_{azi} , \bar{p}_{h1} , and \bar{p}_{h2} of the four parameters across the complete region of interest are then the entries of the extended Jones vector in Eq. 4.5. Finally, the degrees of polarization can be calculated according to Eq. 4.6. Slightly different 2D-polarimeter setups were also used by other groups [27, 75].

5 Radially polarized mode-locked thin-disk laser

In this chapter the setup and experiments are described, that led to the first demonstration of a radially polarized mode-locked thin-disk laser. The mode-locked operation and the radial polarization state were obtained by means of a SESAM and a GWOC, respectively. Thus, the first and the second section of this chapter are dedicated to these components. For the SESAM the behavior regarding its saturation and damage threshold for an incident LG_{01}^* mode are discussed. As the GWOC is a new device, that was used for the very first time, the second section treats the design, production and first qualification of these devices. As already pointed out before, linear phase shifts inside the laser cavity can be detrimental for the polarization purity of the emitted CVBs. Therefore, an experimental investigation regarding the influence of such a phase shift on the polarization state was performed. The results of this investigation will be presented in the third section. This is followed by a thorough discussion of cavity design issues arising from setting up a laser cavity with a dominant doughnut-shaped mode. After a description of the actual laser design and the presentation of the experimental results, the chapter is concluded with a summary.

5.1 Considerations regarding the behavior of the SESAM

This section discusses some preceding considerations regarding the behavior of the SESAM. At first, the theoretical investigation of the saturation of a SESAM in response to an incident doughnut-shaped beam is discussed. To numerically evaluate the behavior, the approach usually used to derive the required SESAM parameters was slightly modified. Furthermore, the relative damage thresholds that apply for a Gaussian and a doughnut-shaped mode are compared.

5.1.1 Saturation

For a beam with a flat-top intensity distribution and under the assumption of a slow saturable absorber, the saturation of the reflectivity R of a SESAM can be described by

the function [76]

$$R(F_p) = R_{ns} \frac{\ln \left(1 + \frac{R_{lin}}{R_{ns}} \left(e^{\frac{F_p}{F_{sat}}} - 1 \right) \right)}{\frac{F_p}{F_{sat}}} e^{-\frac{F_p}{F_2}} \quad (5.1)$$

wherein F_p is the pulse fluence, R_{ns} the reflectivity for pulses with a high fluence, R_{lin} the reflectivity in the unsaturated state, F_{sat} the saturation fluence of the SESAM and F_2 the parameter describing the decrease of the reflectivity at high fluences caused by inverse saturable absorption. For dominant two photon absorption (TPA) the parameter F_2 depends on the two photon absorption coefficient β_{TPA} and is proportional to the pulse duration [77]. An exemplary behavior for the reflectivity of a SESAM with weak ($\frac{F_2}{F_{sat}} \approx 0.5 \cdot 10^5$), strong ($\frac{F_2}{F_{sat}} \approx 0.5 \cdot 10^3$) as well as without any TPA is depicted in Figure 5.1 as a function of the saturation parameter S , where

$$S = F_p / F_{sat}. \quad (5.2)$$

Alternatively to the parameters introduced above, the graph also shows the saturable and non-saturable absorption ΔR and ΔR_{ns} , respectively, which are parameters often provided by manufacturers. They are related to R_{ns} and R_{lin} by $\Delta R = R_{ns} - R_{lin}$ and $\Delta R_{ns} = 1 - R_{ns}$. These parameters are determined by measuring the reflectivity of the SESAM for different pulse fluences, which results in a curve comparable to the calculated one shown here. Subsequently, the parameters are derived by fitting the theoretical curve to the experimental data. However, as mode-locked lasers do not oscillate in a transverse flattop mode, Eq. 5.1 should not be directly fitted to the measured reflectivities. Rather the local reflectivity $R(F_p(r))$, depending on the local fluence $F_p(r)$ of the incident beam, can be integrated over the whole beam cross-section to get the precise total reflectivity R_{tot} for a given pulse energy and beam shape. This can be done by combining Eq. 5.1, which now depends on r , with

$$R_{tot} = \frac{1}{E_p} \int_0^\infty 2\pi r dr R(F_p(r)) F_p(r). \quad (5.3)$$

as demonstrated by Haiml et. al in [76], wherein E_p is the energy of the incident pulse. For an incident Gaussian beam with a local fluence $F_{pG}(r)$ given by

$$F_{pG}(r) = \frac{2E_p}{\pi w_0^2} \cdot e^{-\frac{2r^2}{w_0^2}} \quad (5.4)$$

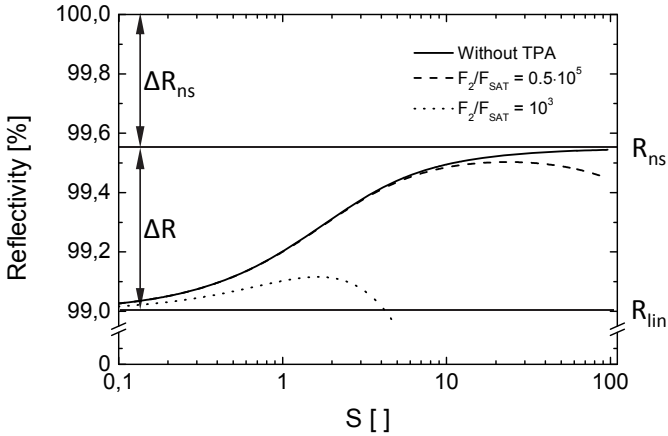


Figure 5.1: Reflectivity of a SESAM with weak, strong and without TPA versus the saturation parameter S .

they were able to demonstrate an improvement of the fit when using Eq. 5.3 with $F_p(r) = F_{pG}(r)$ instead of simply using Eq. 5.1. Moreover, in the same publication the quality of the fit with and without the inclusion of TPA was investigated. It turned out that the fit is sufficiently accurate up to a saturation of $S = 10$ even without taking TPA into account. It is apparent from Figure 5.1 that this only holds as long as the TPA is not too strong, otherwise the rollover affects the saturation behavior strongly even for saturation values below 10.

Following the chain of reasoning above, the saturation behavior of a SESAM for an incident doughnut-shaped beam with a pulse energy E_p can be calculated by introducing the local fluence $F_{pD}(r)$ of such a beam given by

$$F_{pD}(r) = \frac{4E_p \cdot r^2}{\pi w_0^4} \cdot e^{-\frac{2r^2}{w_0^2}} \quad (5.5)$$

into Eq. 5.3 with $F_p(r) = F_{pD}(r)$. To be able to theoretically compare the saturation behavior of the SESAM for the incidence of a Gaussian and a doughnut-shaped beam, the parameters provided by the manufacturer (ΔR , ΔR_{ns} and F_{sat}) can be used.

In a first step, the reflectivity curve versus the pulse energy is calculated for a Gaussian mode of a given size according to Eq. 5.3 again with $F_p(r) = F_{pG}(r)$. Subsequently,

the reflectivity curve for an incident doughnut-shaped mode, given by Eq. 5.3 with $F_p(r) = F_{pD}(r)$, can be fitted to the calculated values with w_0 as the fitting parameter. The result is the size of the doughnut-shaped mode for which a comparable saturation behavior is obtained as with an incident Gaussian mode of a given beam radius. As the M^2 -value of an ideal doughnut-shaped mode is 2.0, the radius w_d of this beam, calculated according to the second moment method, is given by $w_d = \sqrt{2}w_0$ [78].

In Fig 5.2 the approach was applied for a SESAM with $\Delta R = 0.55$, $\Delta R_{ns} = 0.45$ and $F_{sat} = 140 \mu\text{J}/\text{cm}^2$. As the parameter F_2 , describing the magnitude of the inverse saturable absorption, was unknown, the fit was only done up to a saturation of $S \approx 10$ to limit the error of the result. Figure 5.2 (a) shows the size w_d of the doughnut-shaped intensity distribution, resulting from the fitting procedure, for various radii of the Gaussian beam. The obtained values are only slightly larger than the corresponding radii of the Gaussian mode. Therefore, one can conclude that the behavior of the SESAM for the two different intensity distributions is comparable. Hence, in terms of the SESAM saturation, it is feasible to predict the mode-locking behavior of a laser with a doughnut-shaped mode based on results obtained with Gaussian mode lasers. The reflectivity curve for a Gaussian mode with a beam radius of 0.45 mm with the behavior for the corresponding doughnut-shaped mode is exemplarily depicted in Figure 5.2 (b).

5.1.2 Damage threshold

Another important parameter that has to be considered is the damage threshold of the SESAM. As stated in [77], the fluence at which a damage is expected is proportional to $\sqrt{F_2}$ and related to the energy absorbed due to inverse saturable absorption. It is interesting to note that, according to the same source, this value does not depend on the absorber itself but rather on the summarized TPA in the different layers of the complete structure. Treating the damage mechanism laterally as a localized effect, one can compare the peak intensities of a Gaussian and a doughnut-shaped beam. This way, it is possible to estimate the damage threshold for the latter, based on the experience made with systems operating with a Gaussian mode. As shown in the previous section, a doughnut-shaped mode leads to a comparable saturation behavior of the SESAM as a Gaussian mode of the same size. Therefore, it is reasonable to compare the peak intensities of modes of the same size as shown in Figure 5.3. It is evident that the peak fluence of the doughnut-shaped mode is lower than that of the Gaussian mode with the same 2nd moment width. More precisely, it can be shown that the peak intensity is smaller by a factor of 0.74. Hence, during stable mode-locked operation the intra-cavity pulse energy can be larger

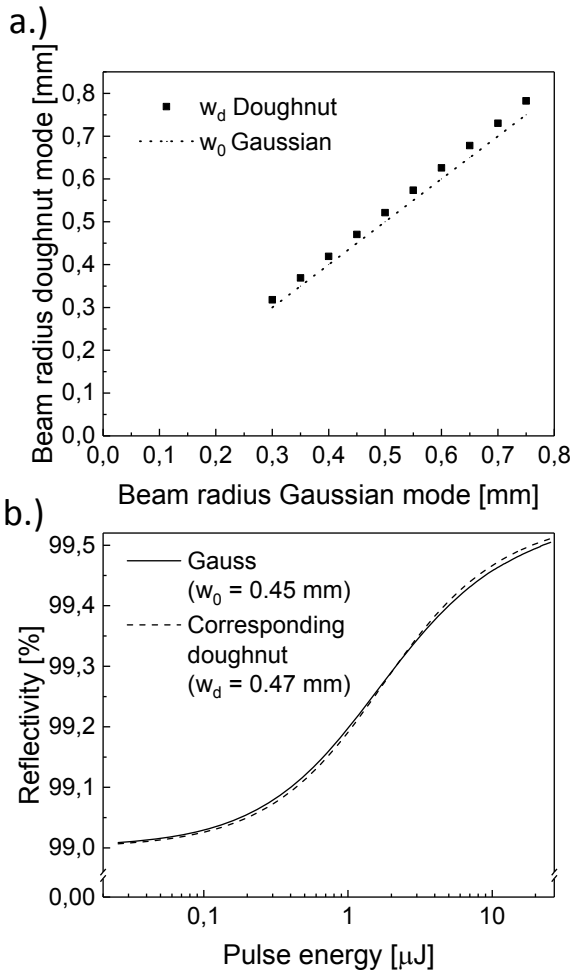


Figure 5.2: Beam radius of a doughnut-shaped mode saturating the SESAM to the same extent as a fundamental mode with the given beam radius (a) and an exemplary fit for a beam radius of the fundamental mode of 0.45 mm (b).

by a factor of 1.36 compared to that of a Gaussian mode laser without getting damaged, as long as both systems emit pulses with the same pulse duration.

5.2 Grating waveguide output coupler

In the following the design and functionality of the GWOCs will be explained. Afterwards, some information on the production will be given and the results of the qualification of the produced devices will be presented. It has to be noted, that the GWOCs were designed by Dr. Marwan Abdou Ahmed at IFSW and fabricated at the Institut für technische Optik (ITO) of the University of Stuttgart.

5.2.1 Design

The design of the GWOCs used for the experiments discussed in this work is based on the approach introduced in [79]. The devices consist of alternating corrugated quarter-wave layers (for a laser wavelength of 1030 nm and an AOI of 0°) of Ta_2O_5 and SiO_2 on a micro-structured standard fused silica substrate with a thickness of 6.35 mm and a diameter of 25.4 mm. The structure and the principal functionality is schematically depicted in Figure 5.4. The discrimination in the reflectivity spectra for incident beams

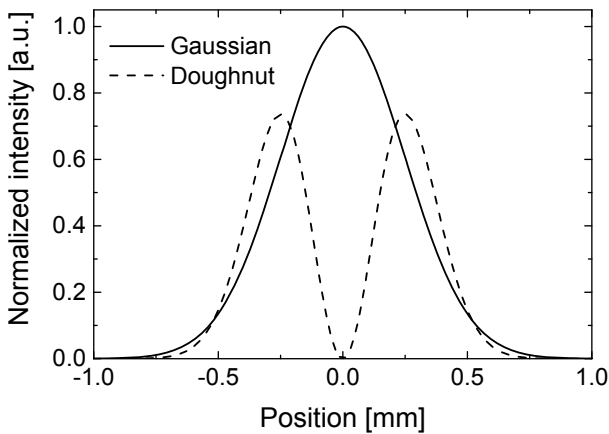


Figure 5.3: Comparison of the intensity of a fundamental Gaussian and a doughnut-shaped mode.

with radial and azimuthal polarization is achieved by choosing the grating parameters such that light with one of the two polarization states (azimuthal in Figure 5.4) efficiently couples to leaky modes in the multi-layers of the device. This coupling effect increases the diffraction into the $\pm 1^{\text{st}}$ diffraction order of the grating. Hence, the reflectivity for a beam with this polarization is significantly decreased at the respective wavelength. For the orthogonal polarization (i.e. radial in Figure 5.4) no leaky mode is excited and therefore a much higher reflectivity is obtained. One of the major challenges in designing a GWOC is to minimize the diffraction of the transmitted beam (radial in Figure 5.4) into the $\pm 1^{\text{st}}$ diffraction order. The parameters that can be varied to obtain the desired reflectivity are the duty cycle, the period, and the depth of the grating. In case of a more complex design also the thickness and the number of the nominal "quarter-wave" layers can be adjusted. As the gratings were meant to be used as output couplers the backside of the substrates were AR-coated. The nominal residual reflectivity of the AR coating was less than 0.1 % at a wavelength of 1030 nm. The substrate was additionally wedged by $30'$ to prevent even minimal back reflections into the cavity that might occur at the AR-coated surface, as such back reflections could have destabilized the intended mode-locked operation. Since the light that is diffracted into the $\pm 1^{\text{st}}$ diffraction orders heats the mount of the grating, the mount has to be water-cooled in high-power systems to avoid thermally induced misalignment of the laser.

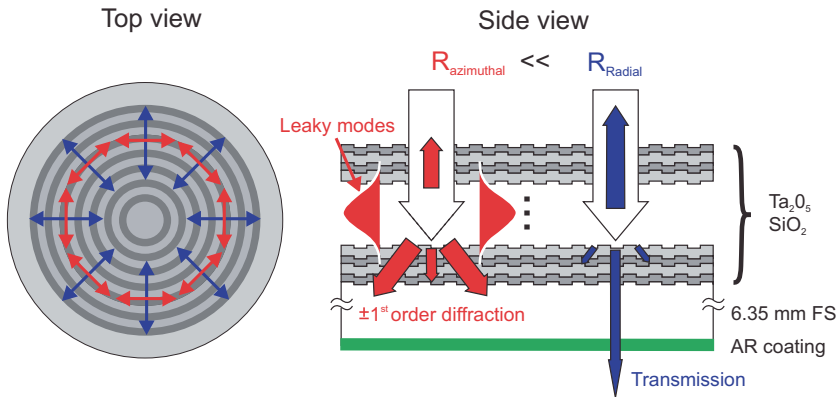


Figure 5.4: Schematic of the structure and the principal of function of the GWOC.

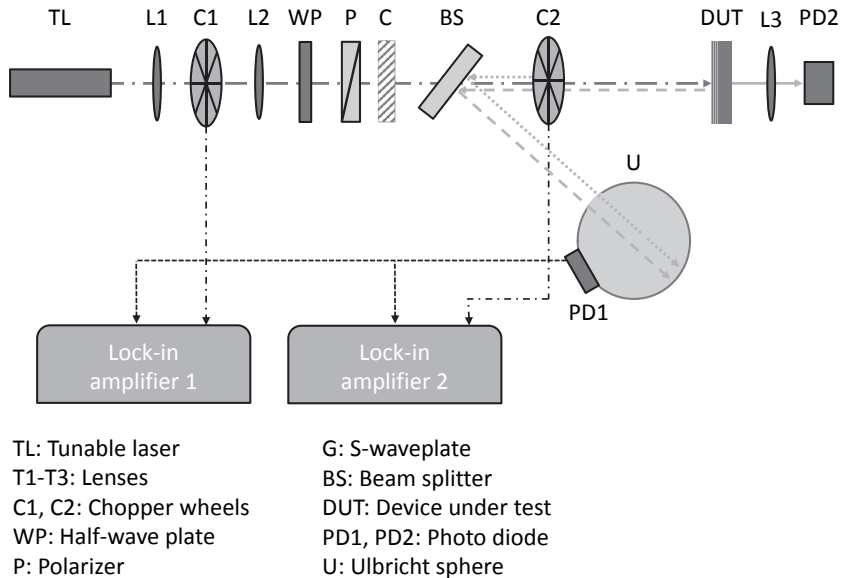


Figure 5.5: Schematic of the setup used to determine the reflectivity and transmission of the GWOCs for beam with a radial or azimuthal state of polarization.

5.2.2 Production and qualification

The production of a GWOC starts with the deposition of a photo resist on the substrate. The photoresist is then exposed using laser direct writing lithography. The development of the photoresist is followed by a dry etching process. Finally, the structured substrate has to be cleaned of the residual resist, before it can be coated with the quarter-wave layers using the ion plating layer deposition technology. The diameter of the structured area of the GWOCs was 6 mm. Figure 5.6 shows an image of a GWOC and a side view of a cleaved sample taken with a scanning electron microscope¹ (SEM) to image the quarter-wave layers.

To verify the quality of the produced GWOCs, the reflectivity was measured by Tom Dietrich with a customized reflectivity measurement setup for radially and azimuthally polarized light. The setup is schematically depicted in Figure 5.5. The light source is a laser with a tunable wavelength. The first lens pair (L1,L2) is used to expand the beam. The half-wave plate (WP) in conjunction with the polarizer (P) are used to guarantee

¹The SEM image was kindly provided by the Insitut für Mikroelektronik.

a good linear polarization on the subsequent polarization converter (C) and to set the incident power on the device under test (DUT). To transform the linear polarization into a radial or azimuthal polarization a s-waveplate is used [25]. The first chopper wheel (C1) and lock-in amplifier are used to generate a signal that is proportional to the current output power of the tunable laser. The second chopper wheel has a highly reflective (HR, $R=0.9995$) coating for the wavelength range of the laser source. The partially reflective beam splitter (BS) is used to direct the light reflected by the chopper wheel and the tested device into the Ulbricht sphere (U). Hence, the photo diode (PD1) sphere gets an alternating signal from the chopper wheel and the tested component. Thus, the second lock-in amplifier measures a signal proportional to the difference between the reflectivities. The actual reflectivity of the grating can be calculated using the signals from the two lock-in amplifiers. The transmission of the gratings is measured with the second photo diode (PD2) by comparing the signals with and without the DUT in the beam path. The lens (L3) is used to focus the beam onto the photo diode. Obviously, the transmission measurement lacks the feedback of the current power of the tunable laser and is therefore less precise than the measurement of the reflectivity. A thorough introduction of the setup for linear gratings, which means that the s-waveplate is taken out of the setup, and the calculation of the reflectivity based on the signals of the two lock-in amplifiers can be found in [80].

For comparison the calculated and measured reflectivity for an exemplary grating are depicted in Figure 5.7. The grating had a nominal period of 900 nm, a depth of the grooves of 30 nm, a duty cycle of 50 %, and 11 layers on top of the substrate. It can be seen that the dip in the reflectivity is smaller than intended and shifted to shorter wavelengths. The two parameters that might lead to such a strong blue shift are the period of the grating and the optical thickness of the nominal quarter-wave layers. As both parameters are usually well controlled by the manufacturer it is not yet clear what exactly caused the discrepancy between the calculated and the measured reflectivity. Despite the deviation from the actual design values, the finally obtained discrimination of approximately 30 % of the reflectivity at a wavelength of 1030 nm for beams with radial ($R = 94.7 \%$) and azimuthal ($R = 64.9 \%$) polarization is by far sufficient to build a laser with the desired polarization state. Even for smaller differences of the reflectivity it has been demonstrated that it is possible to obtain laser operation with a high polarization purity [81].

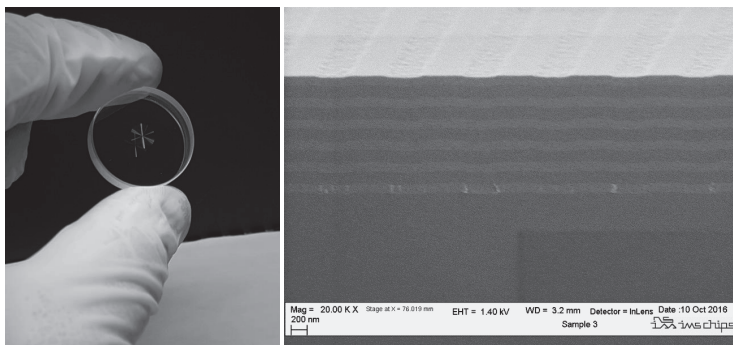


Figure 5.6: Photograph (left) and SEM image (right) of a GWOC.

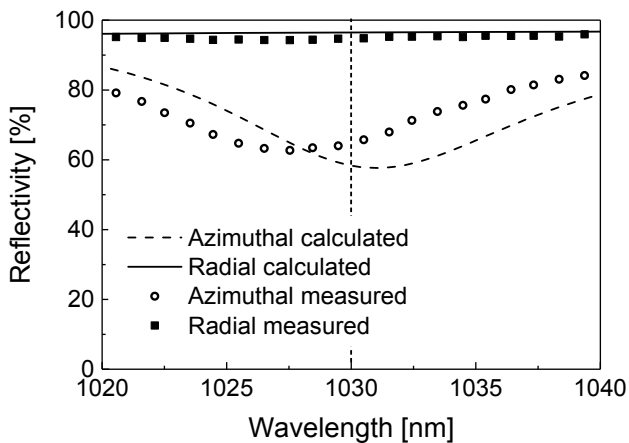


Figure 5.7: Calculated and measured reflectivity of a radially and an azimuthally polarized beams under perpendicular incidence.

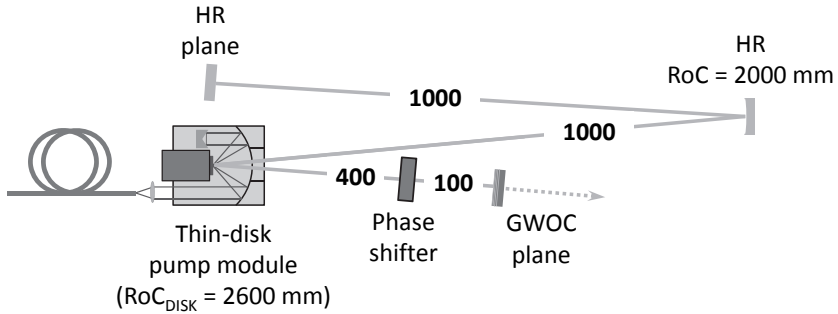


Figure 5.8: Schematic setup of the system used to investigate the effects of a linear phase shift inside the cavity on the polarization state of the outcoupled beam.

5.3 Effects of an intra-cavity phase shift

Regarding the polarization purity, linear phase shifts inside the cavity (e.g. due to the non-zero AOIs on the cavity mirrors) are more detrimental for oscillators emitting CVBs than for lasers with a linear polarization. The latter is only weakly affected by a linear phase shift as long as the main axis of this phase shift is rotated by a small angle relative to the polarization orientation of the laser. On the other hand, CVBs will be especially affected in the axes tilted by 45° relative to the main axis of the phase shift. Preceding tests were performed to quantitatively verify the effect of such a linear phase shift inside the cavity on the performance of a radially polarized laser. For this purpose, a z-shaped cavity was set up, as shown in Figure 5.8². A GWOC and a standard HR mirror were used as the end mirrors of the cavity. The measured reflectivities of the GWOC for incident beams with radial and azimuthal polarization were 95.0 % and 69.7 %, respectively. An increasing amount of linear phase shift was introduced into the cavity by means of a Berek polarization compensator [82]. This device is capable to introduce an adjustable linear phase onto a transmitted beam. The phase shifter was oriented such that the main axes of the phase shift were parallel to the s- and p-polarization of the oscillator. This way, the phase shift had the same effect as that induced by a non-zero AOI on a mirror.

The intensity distributions of the emitted beams for various values of the introduced linear round-trip phase shift are shown in Figure 5.9 along with the corresponding intensity distributions of the beams after transmission through a rotated polarizing beam splitter. The orientation of the polarization of a beam transmitted through the polarizer is indicated

²By convention, throughout this work a positive RoC corresponds to a concave shape of the mirror surface, whereas a negative sign indicates a convex shaped surface.

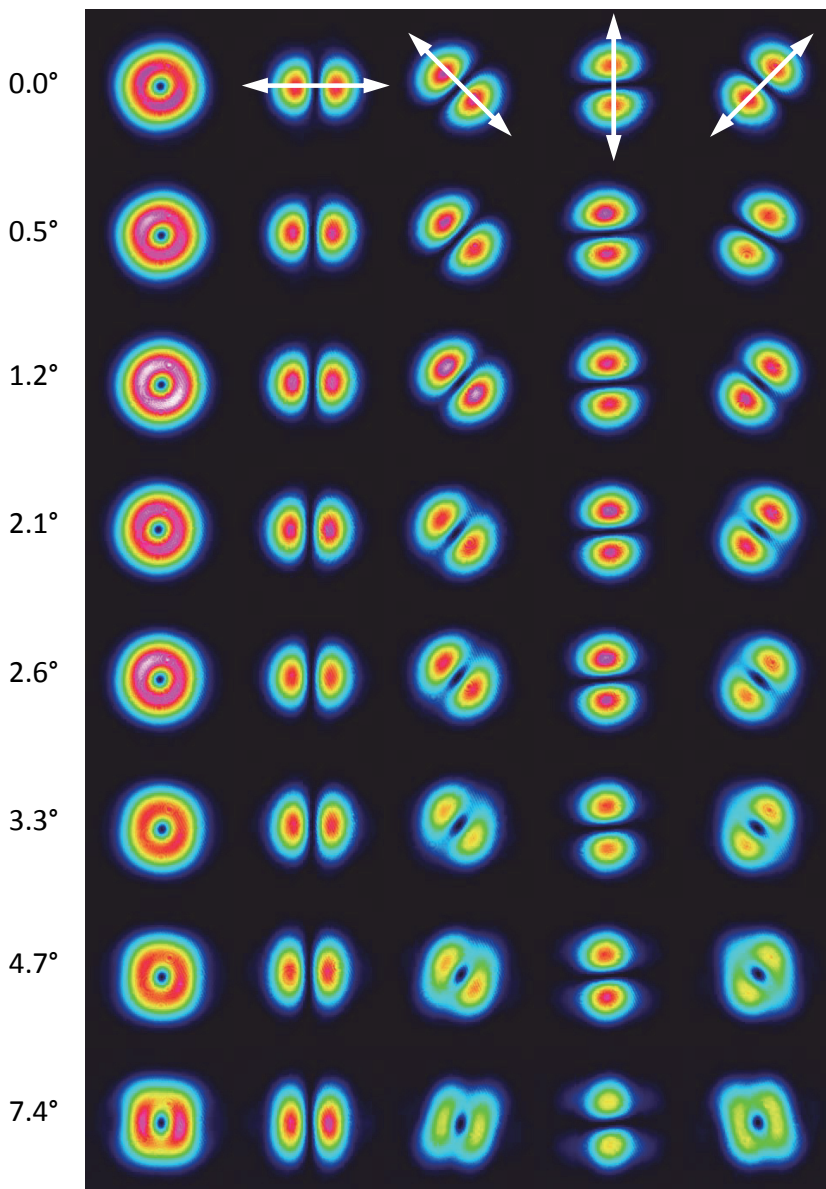


Figure 5.9: Intensity distributions of the output beams for different values of the linear phase shift (per round-trip) introduced into the cavity. The other columns show the intensity distribution of the beam after transmission through a polarizing beam splitter with different orientations of the transmission axis.

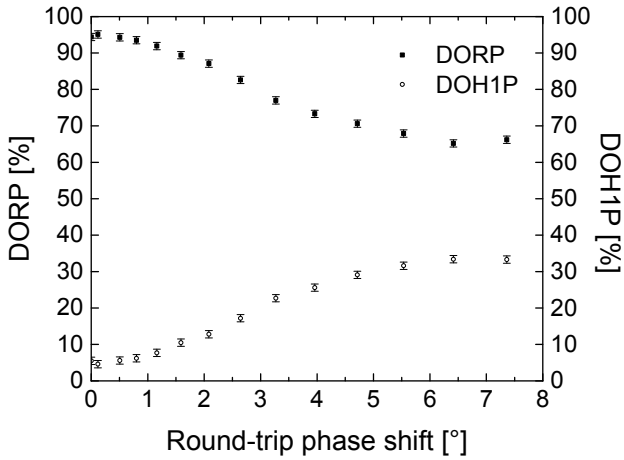


Figure 5.10: DORP and DOH1P of the output beam for different values of the linear round-trip phase shift introduced into cavity.

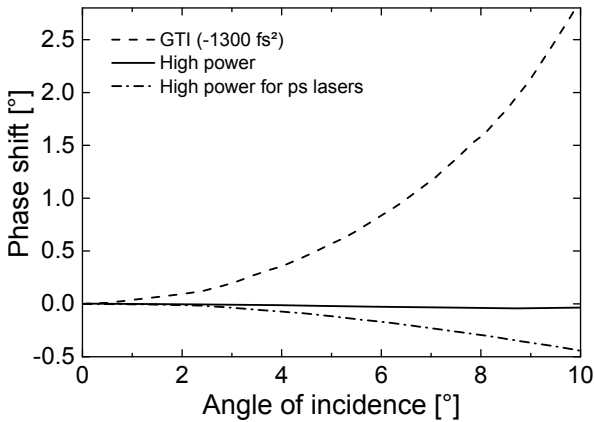


Figure 5.11: Phase shift between incident s- and p-polarized light vs. AOI for different types of mirror coatings.

in the first row by the white arrows. As can be seen, the lobes behind the polarizer oriented at 45° and 135° start to touch more and more with an increasing phase shift until finally the whole beam loses its doughnut shape. The measured DORP decreases with an increasing phase shift until it reaches a plateau, as shown in Figure 5.10. At the same time the degree of H1 polarization (DOHIP) increases by the corresponding amount and the average output power of the laser decreased from 2.1 W to 0.7 W because of depolarization losses. The fact that the DORP only reaches a maximum value of 95 % might have been caused by a mirror with an unnaturally large phase shift for the used AOI .

For comparison, the phase shift between light with a horizontal and vertical polarization, incident on commonly used mirrors, versus the AOI is plotted in Figure 5.11³. As there are two bounces on one folding mirror for each cavity round-trip, it is obvious that especially for the Gires-Tournois interferometer (GTI) mirrors with a group delay dispersion (GDD) of -1300 fs^2 the AOI is very critical. Fortunately, the sign of the phase shift is opposite for different mirror types. Thus, the phase shifts of different mirrors can compensate each other to some extent.

5.4 Considerations regarding the cavity design

Several points had to be taken into consideration when designing an oscillator with a dominant doughnut-shaped mode. First of all the cavity was supposed to support the doughnut-shaped mode with an ideal M^2 -value of 2. Hence, the cavity design was done for the respective M^2 -value using the same design guidelines as commonly used to set up a fundamental mode laser. In general, by choosing the proper ratio of the laser mode diameter to the pump spot diameter (from experience usually a value in the range of 0.7 - 0.85 is working) the onset of modes larger than the desired mode can be suppressed by the insufficient gain-loss balance of these higher order modes. Additionally, the oscillation of the Gaussian mode is prevented by the use of the GWOC, which only supports the efficient oscillation of modes with the correct polarization state and no intensity in the beam center. As a consequence, only the radially or azimuthally polarized LG_{01}^* is oscillating if using a GWOC with a larger reflectivity for radial or azimuthal polarization, respectively. Another parameter that is crucial for a stable operation is the mode size on the GWOC. The quality of the output beam is extremely sensitive to transverse misalignments between the GWOC and the oscillating mode. Thus, a system with a small beam diameter on the GWOC is harder to align than a system with a larger

³The data was provided by the manufacturer.

beam diameter at that position. This is a result of the larger relative translation for the beam with the small beam diameter for the same absolute misalignment. Finally, to obtain the rotationally symmetric doughnut shape of the mode, it is necessary to design the cavity such that the calculated doughnut-shaped mode of the cavity exhibits as little astigmatism as possible. Beside non-zero AOIs on the curved folding mirrors, the astigmatism of the RoC of the SESAM and the Yb:YAG disk pose the major challenges to the cavity design in this sense. Figure 5.12 shows the radii of curvature of a representative subset of the SESAMs available from the manufacturer. The dashed line indicates the case of an ideal SESAM without any astigmatism. It is obvious that almost all of the samples exhibit a pronounced asymmetry in terms of their RoC. This had to be taken into account when designing the laser cavity.

5.5 Setup

A schematic of the experimental setup is depicted in Figure 5.13. An Yb:YAG disk with a thickness of $215\ \mu\text{m}$, a nominal doping concentration of 7 at. %, and a diameter of 12 mm was used as the amplifying medium. The disk was wedged by 30° to prevent detrimental back reflections at the AR coating of the disk, as such back reflections can destabilize the ML process. The disk was optically pumped using a fiber coupled pump diode with a

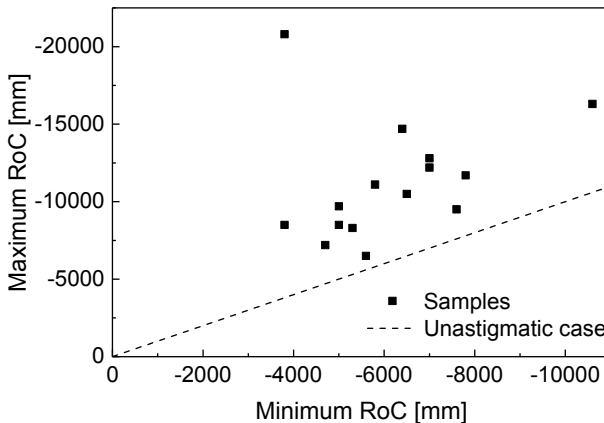


Figure 5.12: Measured RoC of a representative subset of the SESAMs available from the manufacturer. For comparison the dashed line indicates the ideal case of an unastigmatic SESAM.

central emission wavelength around 940 nm. The multi-mode fiber had a core diameter of 1 mm. The disk was mounted onto a concave polycrystalline diamond heat sink to enable efficient heat extraction. To guarantee a sufficiently high pump absorption the disk was integrated into a standard 24-pass pump module [83]. The RoC of the disk was approximately 4000 mm and exhibited negligible astigmatism. The pump spot diameter was set to 2.7 mm. Mode-locking was achieved by using a SESAM from BATOP GmbH⁴ as a cavity end mirror. The SESAM was specified to have a saturation fluence of $140 \mu\text{J}^5$, a recovery time of 1 ps, saturable losses of 0.6 %, and non-saturable losses of 0.4 %. Two GTI mirrors with an overall round-trip GDD of -4400 fs^2 were introduced into the resonator to balance the SPM in the cavity and to allow soliton mode-locking, which takes place in the anomalous dispersion regime [85]. Using the GWOC with the spectral reflectivity depicted in Figure 5.7 as an OC lead to the radial polarization of the laser mode.

Beside the astigmatism of the SESAM, the thermal effects in the Yb:YAG disk, introduced by the increasing pump powers, had to be taken into account in the resonator design. Following the guidelines outlined in the last section led to a cavity with a strong suppression of astigmatism. Figure 5.14 shows the calculated beam caustics of the doughnut-shaped mode in the resonator for different values of the RoC of the SESAM and the disk. First of all the RoC of the disk is varied from the nominal 4 m (in the unpumped state) to a value of 5 m. The RoC of the SESAM is varied from -5 m to -15 m which is sufficient to cover the complete range of RoC of the available SESAMs (compare

⁴BATOP uses the acronym SAM (saturable absorber mirrors) for its SESAMs.

⁵The value given here differs by a factor of 2 to the value given in [84] as BATOP has changed its definition of the fluence in the meantime to allow for a better comparability with other results.

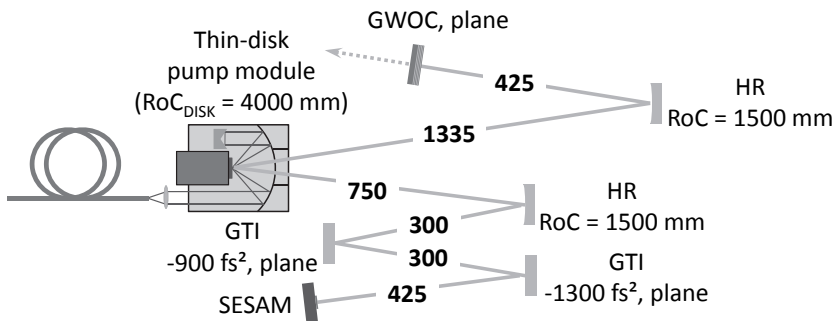


Figure 5.13: Schematic setup of the radially polarized mode-locked laser system including the distances between the components in millimeters.

to Figure 5.12). Although an RoC of the disk of 5 m is even larger than the value expected for the pump powers applied in the experiments, the caustic deviates only slightly. The calculated beam radii on the disk and SESAM are depicted in Figure 5.15. As can be seen, even in the most extreme cases the astigmatism of the beam is negligible. The size of the mode on the disk varies between 1.015 mm and 1.030 mm for all values which corresponds to a ratio of 0.75-0.77 between the laser mode and the pump spot (1.35 mm) radius. As discussed in the former section, these values are in the range aimed for to suppress the onset of oscillation of higher order modes. The beam size on the SESAM of approximately 0.5 mm was expected to be sufficient for output powers of 15-20 W if using an output coupler with a reflectivity of approximately 95 %. This assumption was based on experiences previously made with same SESAM type in oscillators with a Gaussian fundamental mode. For cavity designs with a larger mode size on the SESAM, the astigmatism induced by the imperfect SESAMs would have been stronger.

An advantage of the generally small beam size variation within the cavity is that the mode-locking behavior is decoupled from the thermal lens of the disk. This means, that the saturation of the SESAM (depends on the beam size on the SESAM) and the amount of self-phase modulation of the pulses (depends on the integrated beam size of the caustic of the mode in the resonator) change mostly as a result of a changing intra-cavity power. The minor variation of the beam diameter on the GWOC does also not affect the laser as the beam size is still large enough for all the possible parameter sets. For the sake of completeness the stability parameter $(A+D)/2$, derived from the cavity round-trip matrix, is shown in Figure 5.16. Even for a large RoC of the disk, i.e. a high pump power, the resonator is well within the stability range given by $1 > (A + D)/2 > -1$ [86].

5.6 Experimental results

In the following section the experimental results will be described. At first, the oscillator was qualified in continuous wave (CW) operation. The aim was to determine whether the system would be able to sustain a doughnut-shaped mode, at sufficiently high output powers, without instabilities of the intensity distribution. As the transverse modes are coupled to the longitudinal modes of the cavity, e.g. via the Gouy phase (see Eq. 4.1 and Eq. 4.2), such instabilities would also affect the stability of the mode-locked operation and subsequently risk damaging the optical components of the laser.

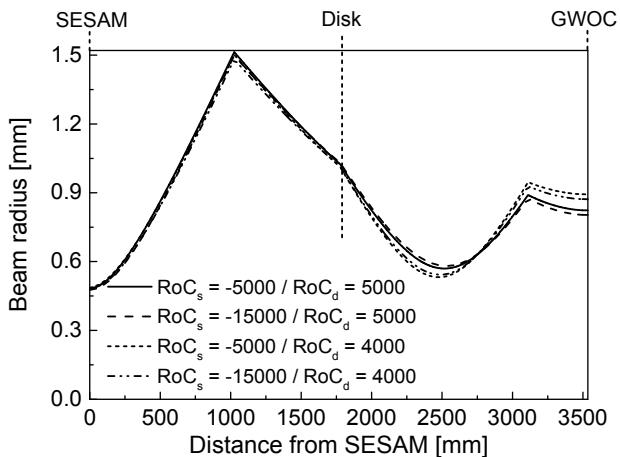


Figure 5.14: Caustic for different ROCs R_d and R_s of the disk and the SESAM, respectively.

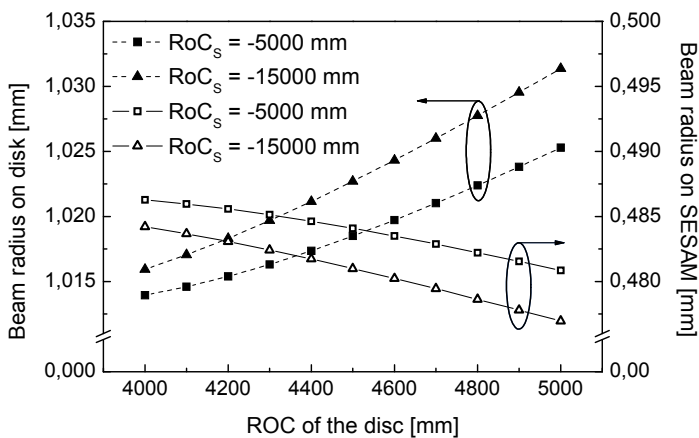


Figure 5.15: Calculated beam radii on the disk and SESAM for a variation of the ROC of the disk and the SESAM, respectively.

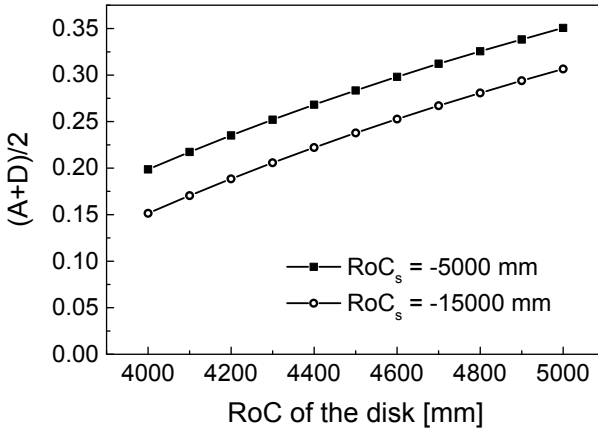


Figure 5.16: Stability of the resonator for a variation of the ROC of the disk and the SESAM.

5.6.1 Performance in continuous wave operation

The oscillator schematized in Figure 5.13 was successively tested in CW operation with a standard outcoupling (OC) mirror (with a transmission of 5 %) and with the GWOC as a cavity end mirror, respectively. CW operation was obtained by using a plane HR mirror instead of the SESAM. The power curves for both cases are shown in Figure 5.17. Additionally, the far field beam profiles at maximum average output power are depicted. It can be seen that the laser already oscillated with a dominant doughnut-shaped mode when using the standard OC. However, the Gaussian mode still had sufficient gain in the center to oscillate in parallel. Compared to that, the Gaussian mode was completely suppressed when using the GWOC, and the far field image shows an almost ideal doughnut-shaped intensity distribution. The additional images, obtained by introducing a rotatable polarizer into the beam path, qualitatively show the high polarization purity of the output beam. The fact that the threshold of the laser in both experiments is at approximately 21 W of pump power indicates that the reflectivity of the GWOC is in the same range as that of the standard OC of 95 %. This is in good agreement with the measured data in Figure 5.7 which states a reflectivity of 94.7 % at a wavelength of 1030 nm. Stable laser operation up to an average output power of 45 W at a pump power of 127 W and a corresponding absolute optical efficiency of 35 % was possible with the GWOC. Above this value, the mode became unstable. While the threshold in both experiments was the same, the slope efficiencies of 52.8 % (standard OC) and 42.3 % (GWOC) differ significantly. This can be attributed to the aforementioned residual diffraction of the outcoupled beam in the GWOC

and possibly to a minor extent to the complete suppression of the fundamental mode in the center of the beam. While direct measurements, done with the setup introduced in Subsection 5.2.2, imply that almost 45 % of the outcoupled light are diffracted into the $\pm 1^{\text{st}}$ diffraction orders, the experiment rather suggests maximum diffraction losses of approximately 20 % (if it is assumed that the lower slope efficiency is solely an effect of the diffraction losses). This uncertainty makes the calculation of the intra-cavity power based on the output power of the laser imprecise, as the possible fraction of the intra-cavity power that is transmitted by the device ranges from 2.9 % ($5.3 \% \cdot 0.55$) to 4.2 % ($5.3 \% \cdot 0.8$).

5.6.2 Performance in mode-locked operation

To obtain mode-locked laser operation the HR cavity end mirror was replaced by a SESAM as already shown in Figure 5.13. As can be seen in Figure 5.18 (a) the threshold of the pump power increased by approximately 1.5 W to 22.5 W. This can be attributed to the additional losses introduced into the cavity by the combined effects of the saturable and unsaturable losses of the SESAM of overall 1 %. Up to an average output power of 1.6 W (28.4 W of pump power) the laser was operating in CW mode. For pump powers

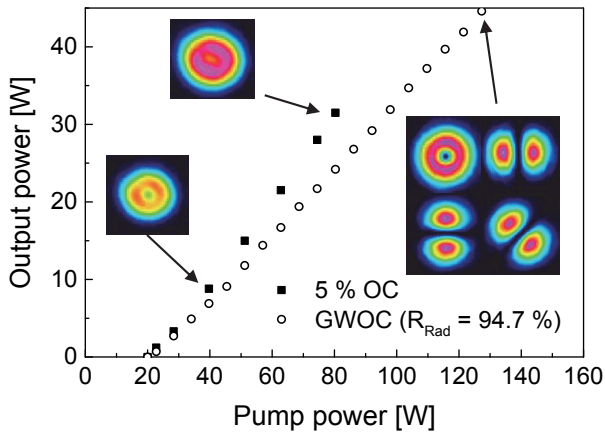


Figure 5.17: Comparison of the CW performance of the oscillator with a standard OC and the GWOC. The images show the intensity distributions of the output beams at the corresponding average output powers of 8.8 W (OC), 31.5 W (OC) and 45 W (GWOC), respectively. For the GWOC experiment, images obtained by positioning a rotating polarizer in front of the camera are additionally shown.

between 30 to 40 W the pulse peak power was strongly fluctuating due to Q-switched mode-locking (QML). As soon as the intra-cavity pulse energy reached a sufficiently high value to suppress QML [87] stable soliton mode-locking took place for average output powers of 7.6 W to 13.3 W with corresponding pump powers of 45 W and 61 W, respectively. The available average output power was limited by increasing instabilities of the mode-locking behavior and the transverse intensity distribution of the oscillating doughnut-shaped mode. These instabilities caused damages to the SESAM as soon as the laser was operated at pump powers above 61 W. The absolute optical efficiency at the maximum average output power was 21.8% as can be seen in Figure 5.18 (b). Taking into account that the laser was operated only three times above threshold, this absolute efficiency is comparable to the performance of other Yb:YAG-based laser systems which were mode-locked with a SESAM and operating in the Gaussian mode [88–90]. In mode-locked operation the system even exhibited an excellent slope efficiency of 36.9 %. Considering the losses due to diffraction into the $\pm 1^{\text{st}}$ diffraction orders, 20 - 45 % higher slope efficiencies will be possible with exactly the same system in case the diffraction losses of the GWOC can be prevented.

As expected from mode-locking theory, the pulse duration continuously decreased with increasing intra-cavity pulse energy [85]. The pulse duration was 1.5 ps and 900 fs (under the assumption of sech^2 -shaped pulses) for average output powers of 7.6 W and 13.3 W, respectively. The autocorrelation of the pulses at the latter operation point is depicted in Figure 5.19 (a). The corresponding optical spectrum is shown in Figure 5.19. It has a full width at half maximum (FWHM) spectral width of approximately 1.5 nm. The resulting time bandwidth product (TBP) of 0.384 is slightly above the value of 0.315 of an ideal unchirped sech^2 pulse. This is in agreement with the theory, as the exact solution of the master equation for a passively mode-locked laser is a slightly chirped sech^2 pulse [91, 92]. Single pulse ML operation was verified using a photo diode from ALPHALAS (bandwidth >2 GHz, rise time <175 ps) positioned behind one of the cavity folding mirrors in conjunction with a fast oscilloscope from Tektronix (up to 5 Gsamples/s) and a wide-range autocorrelation with a span of 150 ps. The autocorrelation as well as the oscilloscope signal confirmed the single pulse operation. The pulse repetition rate of the system was in the range of 42.1 MHz. At the maximum output power, this corresponded to a pulse energy of 316 nJ and a resulting pulse peak power of 0.31 MW taking into account the sech^2 pulse shape. Assuming a beam size of 0.47 mm on the SESAM and considering the possible transmission rate of the GWOC (2.9 - 4.2 %), the laser was operated with a saturation factor of the SESAM ranging from 7.5 (4.2 % transmission) to 11 (2.9 % transmission) at the maximum output power. These numbers are well within the range of values at which Gaussian mode lasers, built with

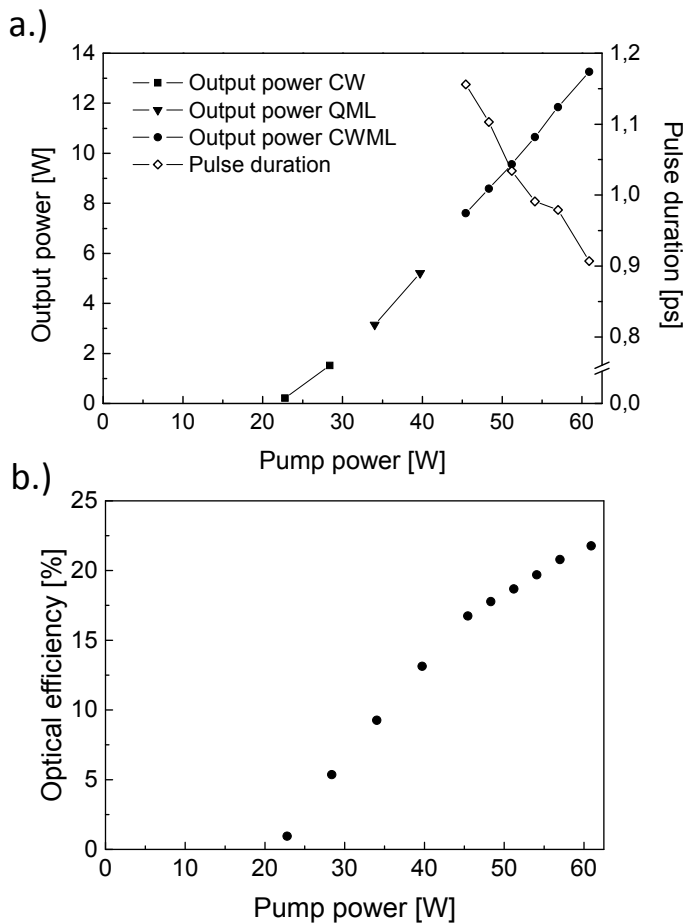


Figure 5.18: Output power of the oscillator for continuous wave (CW), Q-switched mode-locked (QML), and CW mode-locked operation and the corresponding pulse duration in mode-locked operation (a). Additionally, the optical efficiency of the system is shown in (b).

the same type of SESAMs, became unstable. Thus, the average output power of the laser was most probably limited by the increasing saturation of the SESAM, which caused the formerly described instabilities.

The pulse trace in Figure 5.20 (a) confirms the high stability of the laser in terms of pulse peak power. Furthermore, no side bands appeared in the radio frequency (RF) spectra in (b). Side bands would appear next to the repetition frequency of the laser in case of a modulation of the pulse train envelope due to relaxation oscillations. Even above the QML limit these can lead to fluctuations of the pulse energy and the pulse peak power [93]. The two radio frequency spectra were measured with a span of 90 kHz at a resolution bandwidth (RBW) of 30 Hz and a span of 1 MHz at a resolution bandwidth of 1 kHz, respectively. Furthermore, over the course of one hour no degradation was observed in terms of output power, beam quality or stability of the mode-locked operation.

The radial polarization purity was qualitatively evaluated by taking images of the far field of the laser's output beam with a rotating polarizer in front of a CCD-camera. The white arrows in Figure 5.21 indicate the orientation of the polarization of light transmitted through the polarizer. The orientation and the clear separation of the lobes indicates the high polarization purity of the laser beam. The beam itself had an almost ideal axially symmetric intensity distribution, and the Gaussian mode was clearly suppressed. To quantitatively determine the polarization purity of the radially polarized laser beam the DORP was measured using the aforementioned camera-based 2D Stokes polarimeter (see Subsection 4.2). At an average output power of 13.3 W a DORP of 97 ± 1 % and DOHIP of 3 ± 1 % were determined. The fact that the beam is only polarized in the radial and

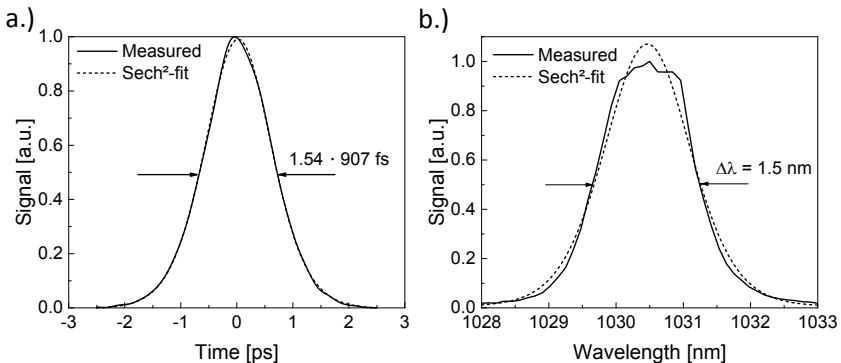


Figure 5.19: Autocorrelation (a) and optical spectrum (b) of the output pulses at the maximum output power of 13.3 W.

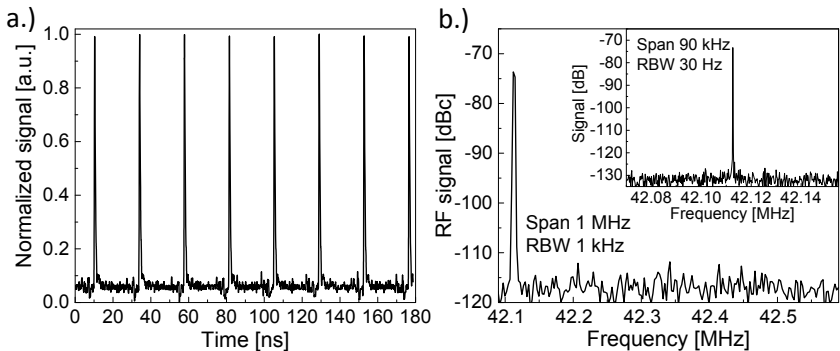


Figure 5.20: Temporal behavior (a) and radio frequency spectra (b) of the radially polarized mode-locked laser at the maximum average output power of 13.3 W.

the H1 states indicates that the DORP might have been improved by further minimizing the AOIs on the folding mirrors (see Section 5.3), which would have decreased the phase shift induced between *s*- and *p*-polarized components of the beam. A far field image of the beam overlaid with a subset of the local polarization ellipses extracted from the 2D-polarimeter measurement is shown in Figure 5.21. The high DORP is reflected in the low ellipticity and the alignment of the majority of the ellipses towards the center of the beam.

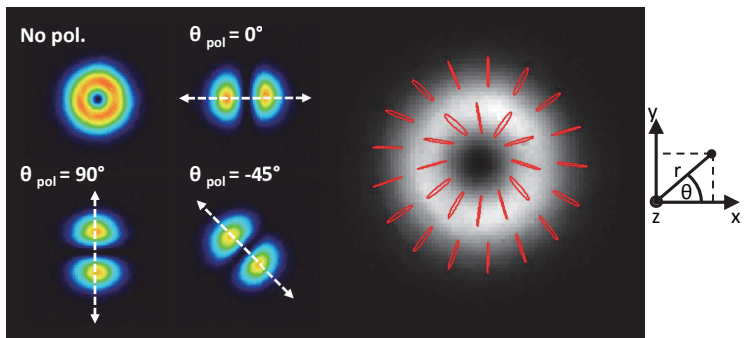


Figure 5.21: Images of the intensity distribution of the output beam obtained by placing a rotation polarizer in front of the camera. The white arrows indicate the orientation of the transmitted polarization. Furthermore, the beam cross-section with a subset of the polarization ellipses obtained with the 2D-polarimeter is shown.

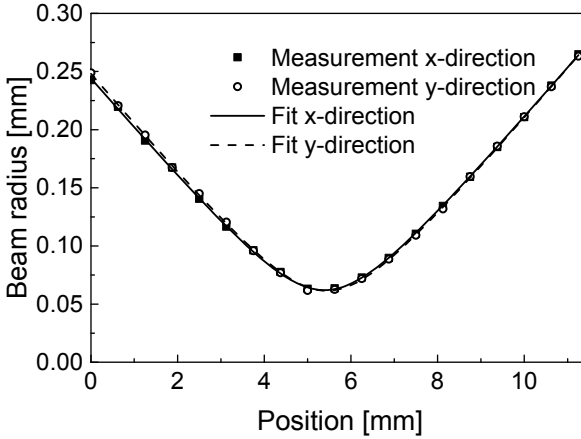


Figure 5.22: Measured beam radii for the vertical as well as the horizontal direction including the related fit curves. For both cases the M^2 was < 2.1 .

The M^2 of the beam was measured to be < 2.1 for the x- as well as the y-direction. This is close to the value of 2.0 for an ideal LG_{01}^* mode. For the complete pump power range no astigmatism of the emitted beam was observe. As an example, Figure 5.22 shows a measurement of the beam radii (determined according to the 2nd moment method [94]) along a caustic at the maximum average output power of the laser. Hence, the design of the resonator led to the desired results.

5.7 Summary

In this chapter the experimental results of the first demonstration of a radially polarized mode-locked thin-disk laser were presented. To be able to achieve this special mode of operation, a new device called "grating waveguide output coupler" and a SESAM were used as the cavity end mirrors. A maximum average output power of 13.3 W was achieved at a pump power of 61 W. Higher output powers were prevented by the onset of instabilities and the diffraction losses of the light transmitting the GWOC. The repetition rate was 42.1 MHz. The pulse duration was measured to be 907 fs at the maximum output power assuming sech^2 -shaped pulses. This lead to a pulse energy and a pulse peak power of 316 nJ and 0.31 MW, respectively. The LG_{01}^* mode exhibited an ideal doughnut-shaped intensity distribution and a high DORP of 97 ± 1 %. Additionally, the values of the M^2 were smaller than 2.1. Figure 5.23 shows an overview of the published

results of oscillator systems emitting pulsed CVBs for which the performance parameters are available [5, 41–46, 95–98]. As can be seen in (a) the presented system exhibits the highest average output power and shortest pulse duration of all systems. More precisely, it is the only system showing a pulse duration below 1 ps. In terms of pulse energy only the QS systems achieve higher values. Taking into account the much shorter pulse duration of the presented system, it is evident that it is the system reaching the highest pulse peak powers. Additionally, the homogeneity of the intensity distribution and the polarization purity of the LG_{01}^* mode are unprecedented for pulsed CVB oscillators with several Watts of average output power.

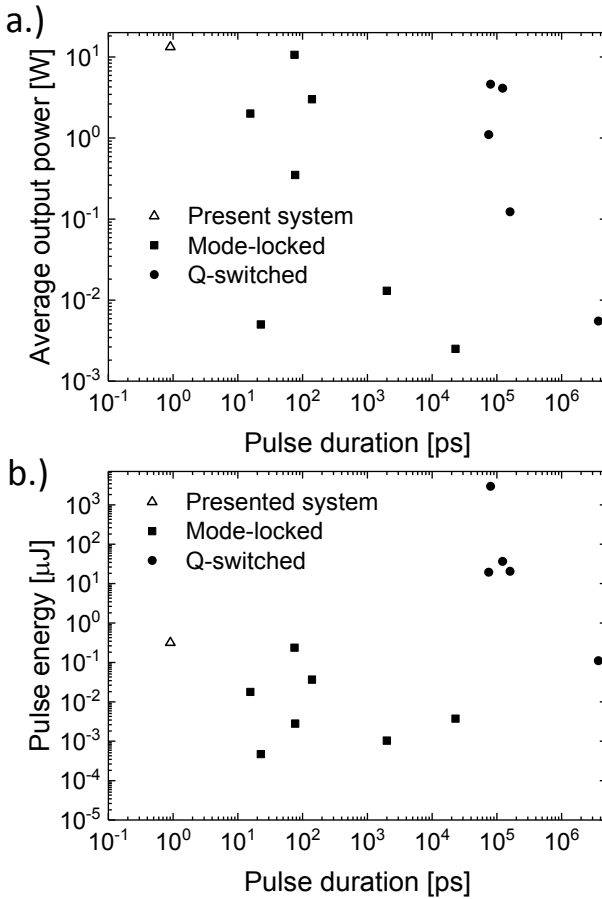


Figure 5.23: Average output power (a) and pulse energy (b) vs. pulse duration of different oscillator systems generating pulsed CVBs (including the system presented in this work) [5, 41–46, 95–98].

6 High-power single-stage single-crystal fiber amplifier

In this chapter the experimental results of the high-power single-stage SCF amplification of the radially polarized mode-locked CVB are presented. The SCF amplifier was considered to be the proper approach to obtain a gain ≥ 4 required to reach the demanded ≥ 50 W of output power with the available seed power. The assumption was based on the results published in [49]. Therein, the IFSW, in collaboration with the Institut d'Optique in Paris and Fibercryst SAS, reported on the successful high-power amplification of CW CVBs (radially and azimuthally polarized). Average output powers exceeding 100 W were obtained, starting from a seed power of 32 W. The gain factor of 3 was achieved in a single-stage single-pass SCF amplifier by means of high-power pumping with up to 515 W. Unlike the SCF modules within the RAZIPOL project [51], the module used for the high-power pumping experiments in [49] contained an Yb:YAG crystal with a doping concentration of only 0.5 at. %. As a result, the CVBs were exposed to lower thermally induced distortions, and thus high polarization purity and good beam quality could be achieved. Considering the lower available seed power of 13.3 W (as compared to 32 W) of the system introduced in the last chapter, the desired gain of a factor ≥ 4 was estimated to be attainable as a result of a lower saturation of the gain in the amplifier crystal. Moreover, using a single-stage amplifier accounted for the aim of this project to simplify the amplification chain compared to the system used in the RAZIPOL project.

Some basic information about the SCF module and its principle of function are given in the first section of this chapter. Afterwards, the results of a numerical investigation, which was done to evaluate the impact of the Kerr self-focusing effect on beams with a doughnut-shaped intensity distribution, are outlined. In the third section the procedure is discussed that was used to correctly set the seed beam parameters on the SCF's entrance facet. In the two subsequent sections the experimental setup and the results are discussed, before the chapter is concluded with a summary.

6.1 Single-crystal fiber module

The SCF technology is considered to be a particularly good choice for the amplification of radially and azimuthally polarized pulsed CVBs. Due to the rod shape and the radial cooling concept an axially symmetric heat distribution will form in the pumped crystal. In turn, such a heat distribution will lead to an axially symmetric stress pattern within the crystal. The only polarization states not affected by these are the radial and the azimuthal polarization. While the seed beam propagates freely in the SCF crystal, the pump light is guided by total internal reflection (TIR). This leads to a concentration of the pump light in the SCF center and subsequently a higher overlap with the seed beam, than obtainable in a rod laser with a larger diameter of the crystal. Furthermore, this allows for the use of low-brightness pump diodes while maintaining a good efficiency of the system. Additionally, the moderate diameter of the amplifier crystal diminishes the problem of nonlinearities arising in fiber amplifiers from high pulse peak intensities.

The single-crystal fiber module used for the presented investigations was a customized version of the SCF module commercially available from Fibercryst [99]. The footprint was more compact than that of the standard module to loosen the geometrical restrictions on the setup and the height of the crystal was fixed to 100 mm. The Yb:YAG crystal had a length of 40 mm, a diameter of 1 mm, and a doping concentration of 0.5 at. %. Both ends of the SCF were AR-coated for the wavelengths of the pump diodes of 940 and 969 nm as well as for the wavelength of the seed beam of 1030 nm. The single-crystal was glued into a groove in an approximately 3 mm thick copper slab. This slab in turn was mounted between two thick, water-cooled copper blocks. To improve the heat transfer between the slab and the copper blocks, graphite foil was placed in between. Figure 6.1 shows a picture of the module used for the experiments. The flow path of the cooling water is indicated by the dashed red line.

6.2 Kerr lens self-focussing

Even though the size of the beam in a SCF amplifier is much larger than in a fiber amplifier, nonlinear effects might reach a level which is not negligible any more at high pulse peak powers. A nonlinear effect that can lead to a collapse of the beam and a resultant damage of the crystal is Kerr lens self-focussing. The critical power P_{crit} of self-focussing is the value at which the convergence of the beam due to Kerr lensing and the divergence due to diffraction cancel each other out. For a Gaussian beam P_{crit} can be derived from Fermat's principle and is given by [100]

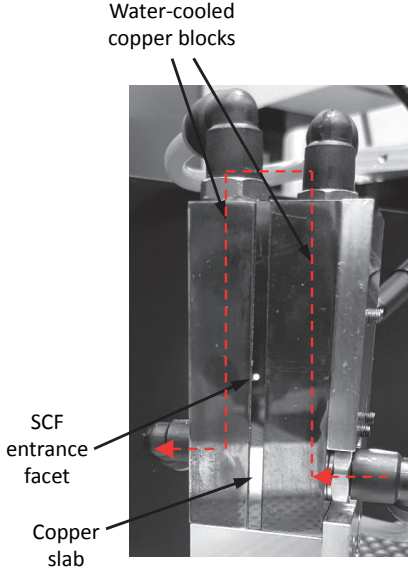


Figure 6.1: Photograph of the module used for the experiments. The flow path of the cooling water is indicated by the dashed red line. The SCF was illuminated from the backside to improve the visibility.

$$P_{cr} = \frac{\pi \cdot 0.61^2 \cdot \lambda_0^2}{8n_0n_2} \quad (6.1)$$

wherein λ_0 is the wavelength of the laser beam in vacuum, and n_0 and n_2 are the linear and nonlinear refractive indices of the material in which the laser propagates. For YAG one obtains a critical power of approximately 1.33 MW, with $n_0 = 1.815$ (at 1030 nm [101]) and $n_2 = 6.5 \cdot 10^{-16} \text{ cm}^2/\text{W}$ [102].

While it is apparent that the Kerr lens has a focussing effect on a Gaussian beam, because of the maximum intensity in the beam center, the situation is different for beams with a doughnut-shaped intensity distribution. Furthermore, the special shape prevents the derivation of an analytical function for the critical power. Thus, a simple numerical evaluation of this parameter was performed prior to the experiments. The beam propagation was simulated using the split-step Fourier method described for example in [103, 104]. In this method the nonlinear effects and the propagation are calculated in separate steps and domains, which are related by the Fourier transformation. To verify the

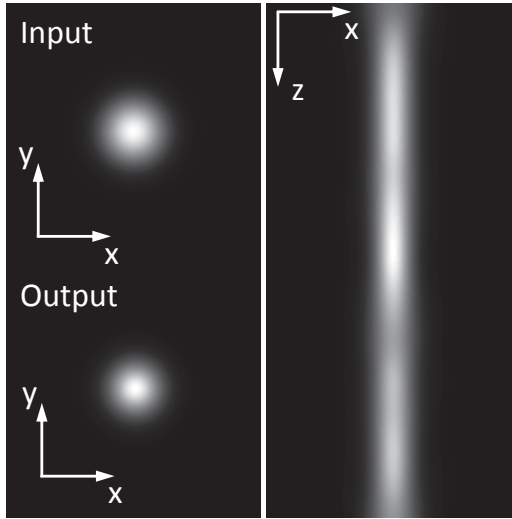


Figure 6.2: Calculated beam profiles of a pulsed fundamental Gaussian beam with a pulse peak power of 1.35 MW before and after the propagation over a distance of 20 m in bulk YAG. Additionally, the evolution of the cross-section of the beam is shown.

validity of the model, the propagation of a Gaussian mode in YAG was simulated at first. Self-phase modulation was not taken into account in the simulation and the propagation was only calculated for the pulse peak. This means that the change of the temporal shape of the pulse due to the Kerr effect was not taken into account. Figure 6.2 shows the beam profiles before and after the propagation over a distance of 20 m in bulk YAG for a pulse peak power of 1.35 MW and a beam radius w_0 of 0.7 mm. As can be seen in the evolution of the beam cross-section, the intensity distribution is almost invariant along the propagation path. This case matches the definition of the critical power. As the peak power of 1.35 MW is almost equal to the analytically calculated value of the critical power of 1.33 MW, the model was considered to be valid. For comparison, a comparable propagation-invariant intensity distribution for a LG_{01}^* mode with a radius $w_d = 0.7$ mm is obtained for a pulse peak power of approximately 5.52 MW. The results of the simulation of a 5 m long propagation¹ can be seen in Figure 6.3. For higher peak powers the beam collapses like it is known from the fundamental mode. Thus, the critical

¹The value of the beam size and the propagation distance were chosen such that the computational requirements in terms of resolution and step number and width could be handled by the system executing the calculations.

power of a doughnut-shaped beam is more than 4 times larger than that of a fundamental Gaussian beam. Assuming that the pulse duration is not affected by the amplification in the SCF, the critical peak power of 5.52 MW translates into a critical average power of more than 200 W using the parameters of the seed laser (0.31 MW peak power, 13.3 W average power) presented in the last chapter. As this value is much larger than the targeted output power of 50 W and taking into account the comparatively short length of the SCF of 40 mm, Kerr lens self-focusing was considered to be uncritical in the experiments presented in this work.

6.3 High-power pumping

In many SCF experiments the seed is prepared such that its waist, with a diameter in the range of 400 to 450 μm , is positioned somewhere within the SCF [105–107]. This is possible because of the moderate pump powers of up to 200 W in these experiments. Due to the strong thermal lens in the SCF for the high-power pumping scheme, such a seed beam would be strongly focussed and therefore risks damaging the output facet's coating

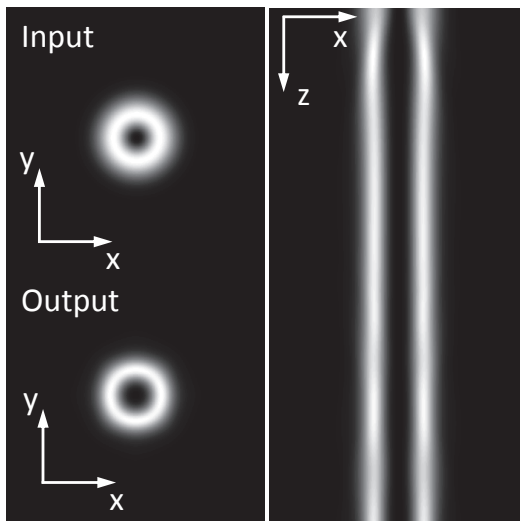


Figure 6.3: Calculated beam profiles of a pulsed radially polarized LG_{01}^* mode with a pulse peak power of 5.52 MW before and after the propagation through 5 m of bulk YAG. Additionally, the evolution of the cross-section of the beam is shown.

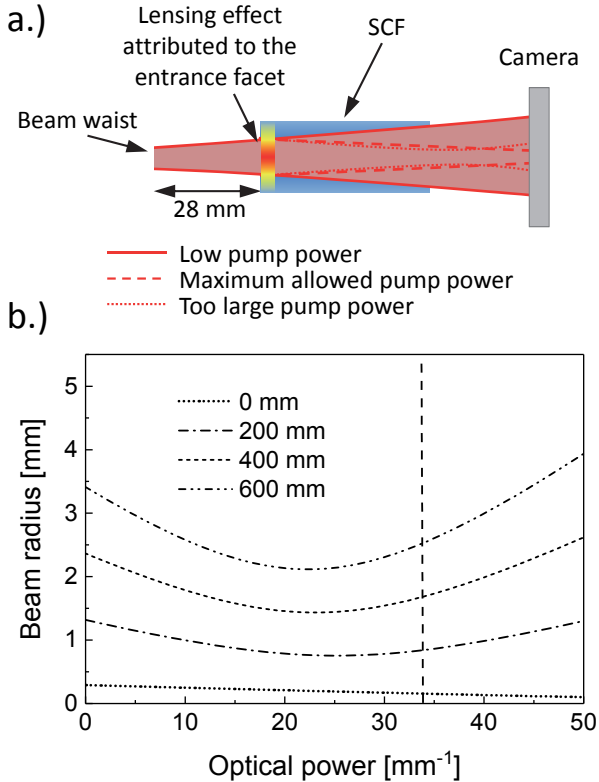


Figure 6.4: Schematic explanation on how a sufficiently large divergence of the seed beam was tested (a) and the calculated beam radii at different positions behind the SCF for a variation of the optical power of the thermal lens (b). For the calculation the complete thermal lensing effect was attributed to the entrance facet of the SCF. The dashed vertical line indicates the point at which the focal length of the thermal lens equals the 28 mm distance between the waist position and the entrance facet of the SCF.

or the SCF itself. Thus, in the experiments discussed in this work, the seed beam was prepared such that it was divergent on the entrance facet of the SCF to compensate for the thermal lens in the crystal. At the same time a good overlap with the pump light had to be guaranteed and excessive clipping at the facets of the SCF avoided. As the exact value of the thermal lens was unknown, preceding experiments were carried out to make sure that the divergence of the input beam was sufficiently large.

Figure 6.4 (a) shows the schematic concept of the approach. To determine the effects of the thermal lens a camera was placed some distance behind the amplifier and the size of the amplified beam was measured. It was assumed that the whole lensing effect can be attributed to the entrance facet of the SCF. This is a reasonable approximation due to the small beam diameter and thus the high intensity of the pump light in the first few millimeters of the SCF [108]. For low pump powers the amplified beam is large on the camera as there is only a minor focussing effect acting on it. When the pump power is increased, the beam radius on the camera decreases until it eventually reaches a minimum. For higher pump powers a beam waist is formed close to the exit facet of the SCF. With a decreasing diameter of this beam waist, as an effect of an increased pump power, the beam propagating towards the camera becomes again more divergent and thus the measured beam radius increases again. The beam radius expected from this simplified model versus the optical power of the thermal lens for different distances from the output facet to the camera is given in Figure 6.4 (b). A diameter of $250\ \mu\text{m}$ of the beam waist at a position 28 mm in front of the SCF was used as the starting point of the beam propagation. The dashed vertical line indicates the optical power of the thermal lens at which the focal length of the thermal lens equals the 28 mm distance to the waist of the seed beam. Thus, the amplified beam would be collimated. At this point the radius of the amplified beam of approximately $150\ \mu\text{m}$ can still be considered as being uncritical, taking into account the starting value of 200-225 μm in other experiments and the generally smaller peak intensity of the LG_{01}^* mode (compare to Subsection 5.1.2). Hence, the thermal lens was unproblematic as long as the measured beam size on the camera was decreasing. It can be seen that the larger the distance between the SCF and the camera is, the larger is also the safety margin and the more sensitive is the approach. At the same time, this test also allowed to make sure that the beam was not too divergent at the maximum targeted pump power. A too divergent seed beam results in diffraction of the amplified beam at the output facet even at full pump power, and hence a distortion of the beam profile. An example of a beam diffracted at the output facet is depicted in Figure 6.5.

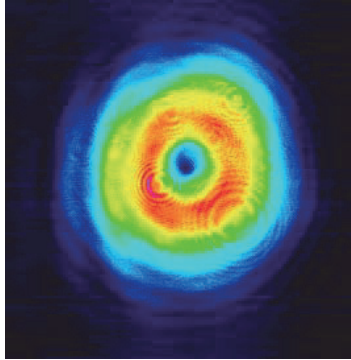


Figure 6.5: Distortion of the beam after the amplification as a result of diffraction at the output facet. This takes place when the divergence of the seed beam at the entrance facet of the SCF is chosen too large and therefore overcompensates the thermal lens.

6.4 Setup

As mentioned before, the radially polarized ultrashort laser pulses of the seed laser were amplified in a customized SCF amplifier module provided by FiberCryst. The experimental setup is depicted in Figure 6.6. An Yb:YAG crystal with a length of 40 mm, a diameter of 1 mm, and a doping concentration of 0.5 at. % was chosen for the experiments. The standard version with a doping concentration of 1 at. % would have provided a larger gain, but first experiments revealed strong distortions of the amplified beam. These were most probably a result of the larger thermal stress in the crystal. For comparison the SCF was pumped with two different pump diodes, one with a standard central emission wavelength around 940 nm and the second one stabilized at the zero-phonon wavelength of Yb:YAG at 969 nm. Both diodes were coupled into a multi-mode fiber with a core diameter of 600 μm and a numerical aperture of 0.22. In each of the experiments the pump beam was prepared by first collimating it using a 2-inch lens with a focal length of 80 mm. A second lens with the same focal length was subsequently used to image the output facet of the multi-mode fiber in a plane 2 mm in front of the SCF entrance facet. This resulted in a divergent pump beam on the SCF facet with a beam diameter slightly above 600 μm . The seed beam was focussed to a beam waist diameter of approximately 250 μm in the plane 28 mm in front of the SCF, leading to a beam diameter in the range of 400-500 μm on the entrance facet of the SCF. The comparatively large diameter guaranteed a good overlap with the pump radiation in the first few millimeters of the SCF. Additionally, the divergence of the seed beam in the SCF

resulted in sufficient compensation of the thermal lensing, which was verified following the approach outlined in Chapter 6.3. Diffraction at the output facet was not observed. The seed and the pump beam were coaxially superimposed in front of the SCF by means of a dichroic mirror. For an AOI of 22.5° the dichroic mirror was AR-coated for the wavelengths of the two pump diodes and HR-coated for the wavelength of the seed beam. As the pump radiation was not completely absorbed in the SCF, a second dichroic mirror behind the SCF was used to separate the unabsorbed pump power from the amplified beam. This second dichroic mirror was highly transmissive for the seed beam and HR-coated for the wavelength of pump diodes for an AOI of 45° . As the seed laser slightly changed its performance between the experiments with the two different pump diodes, e.g. due to the necessary realignment of the setup after a burn-in in the SESAM, Table 6.1 lists all the relevant seed beam parameters for the two experiments.

6.5 Experimental results

The measured average output power as well as the corresponding unabsorbed pump power for the amplification experiments with the 940 nm as well as the 969 nm pump can be found in Figure 6.7 (a). At maximum incident pump powers of 482 W (940 nm) and 519 W (969 nm) the seed beam was amplified to average output powers of 69.7 W and 66.3 W, respectively. These correspond to gain factors of 5.2 and 5.0. In both experiments the unabsorbed pump power increased in a nonlinear fashion, which was most probably a combined effect of the saturation of absorption of the SCF and an increasing crystal temperature. The latter leads to a decrease of the emission and absorption cross-sections of the Yb:YAG crystal, which in turn is also a plausible explanation for the roll-over of

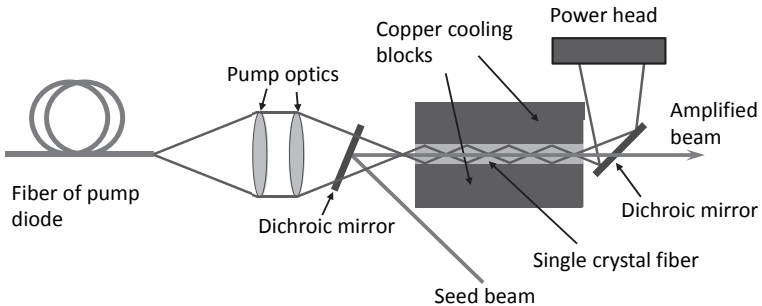


Figure 6.6: SCF amplifier setup.

Table 6.1: Summary of the seed beam parameters (average power P , M^2 , pulse duration τ_p , FWHM spectral width $\Delta\lambda$, pulse energy E_p , pulse peak power \hat{P} and DORP) before and after amplification.

Pump diode	940 nm	969 nm
P [W]	13.3	13.3
M^2	2.1	2.0
τ_p [fs]	938	800
$\Delta\lambda$ [nm]	1.5	1.46
TBP	0.41	0.33
f_{rep} [MHz]	41.5	40.7
E_p [μJ]	0.32	0.33
\hat{P} [MW]	0.30	0.36
DORP [%]	98.7 ± 1	96.8 ± 1

both output power curves.

The absolute efficiency η_{abs} of the amplification process can be defined as

$$\eta_{\text{abs}} = \frac{P_{\text{out}} - P_{\text{seed}}}{P_{\text{pump}}}, \quad (6.2)$$

wherein P_{out} is the average output power of the amplifier, P_{seed} the average power of the seed beam and P_{pump} the average power of the pump diode. Surprisingly, the amplification with the 940 nm diode was more efficient and reached a maximum value of 12.4 % before it started to decrease (Figure 6.7 (b)). With the pump with the wavelength of 969 nm a maximum efficiency of only 11.2 % was reached, and the efficiency was decreasing already for lower pump powers than in the experiments with the 940 nm pump. Considering the lower thermal load of the zero-phonon line pumping scheme (due to a 32 % lower quantum defect) and the almost equal values of the absorption cross-section peaks ($\approx 8 \cdot 10^{-21} \text{cm}^{-2}$) at 969 nm and 941 nm, respectively, one would actually expect a more efficient operation with the 969 nm pump. The explanation for the unforeseen behavior can be found in Figure 6.8. The graph shows the emission wavelengths of the two pump diodes at the given pump power levels (a) and the temperature-dependent absorption cross-section of Yb:YAG at the corresponding wavelengths (b)².

First of all, the central emission wavelength of the nominal 969 nm diode was actually 968.6 nm instead of 969 nm. As a result of the narrow width (≈ 3 nm) of the absorption

²The data in Figure 6.7 (b) was extracted from [109].

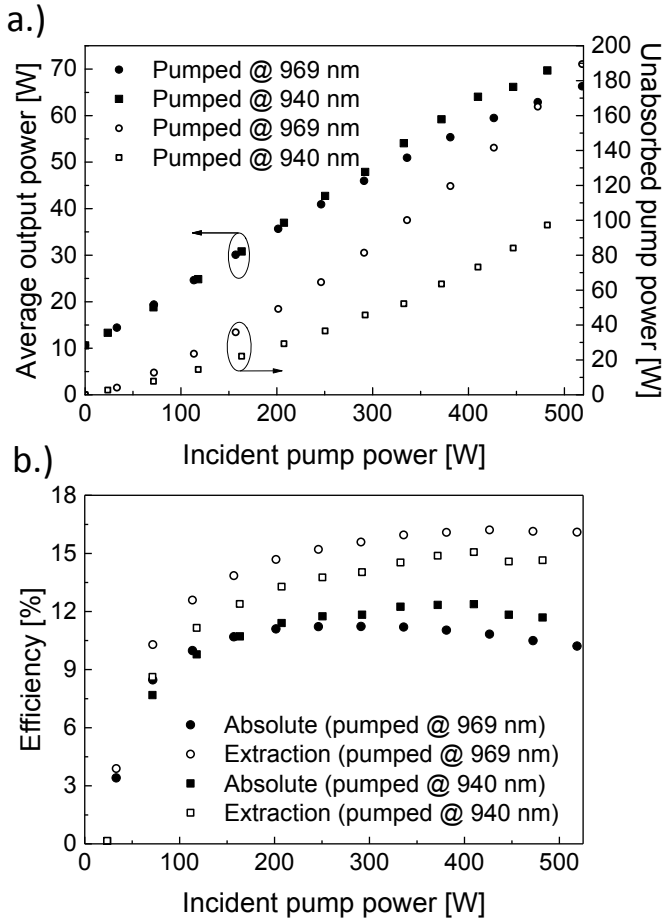


Figure 6.7: Average output power and unabsorbed pump power of the SCF vs. incident pump power for an average seed power of 13.3 W (a). The second graph shows the absolute and the extraction efficiency for both amplification experiments (b).

line, this leads to a 15 % smaller absorption cross-section at the wavelength of the diode compared to the peak value of $8 \cdot 10^{-21} \text{cm}^{-2}$ at a wavelength of 969 nm. Across the complete pump power range the emission wavelength of the 969 nm diode only shifts from 968.6 nm to 968.7 nm because of the wavelength stabilization. Pumping with the 969 nm diode becomes therefore increasingly less efficient with an increasing pump power and the consequentially increasing crystal temperature. In contrast, the 940 nm diode shifts from 937 nm at output powers below 100 W to 942.5 nm at the maximum average output power. Thus, up to a pump power of approximately 400 W, the thermally induced decrease of the absorption cross-section is at least partially compensated by the shift of the pump wavelength towards the absorption peak at 941 nm. Moreover, the heat induced decrease of the absorption cross-section (between 20 °C to 80 °) at the absorption peak at 940 nm is less significant than at absorption peak at 969 nm. The described behavior is well reflected in the lower absorption of the 969 nm pump in Figure 6.7 (a). To further investigate the issue, one can define the extraction efficiency η_{extr} of the amplification process by relating the extracted power $P_{extr} = P_{out} - P_{seed}$ to the absorbed pump power $P_{abs} = P_{pump} - P_{unabs}$, wherein P_{unabs} is the unabsorbed pump power. Then the the extraction efficiency can be written as

$$\eta_{extr} = \frac{P_{extr}}{P_{abs}}. \quad (6.3)$$

The expected lower temperature of the crystal in the experiments with the 969 nm becomes evident if the values of η_{extr} for the two experiments are compared, as done in Figure 6.7 (b). Regarding this parameter, the pumping at 969 nm was 8 % more efficient than pumping at 940 nm. Thereof, 3 % can be directly attributed to the lower quantum defect of this pumping scheme, but the residual 5 % can be related to a larger emission cross-section as a result of the lower temperature. The lower thermal load was also reflected in a more stable operation. For the experiments with the diode emitting at the zero-phonon wavelength of Yb:YAG at 969 nm a maximum fluctuation of the average output power of only ± 0.5 W was observed over the course of half an hour. In contrast, while pumping at a wavelength of 940 nm the average output power dropped by 2.4 W and fluctuated by ± 2 W within the same period of time.

The autocorrelations of the emitted pulses and the corresponding spectra at the maximum output power of the amplifier can be found in Figure 6.9. The pulse duration of the amplified pulses increased from 800 fs to 909 fs and from 938 fs to 1030 fs (under the assumption of a sech^2 pulse shape) for pumping the SCF at 969 nm (a) and 940 nm (c), respectively. While the spectrum for the latter stayed largely unaffected (b) it decreased for the former from 1.46 nm to 1.29 nm (d). As a result, in the experiments with the

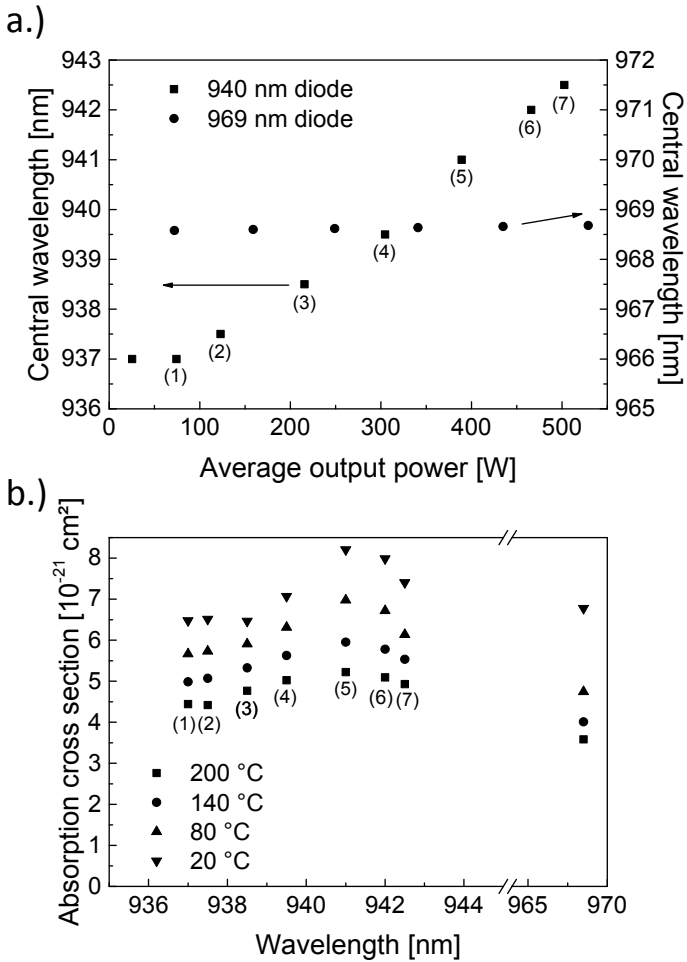


Figure 6.8: Central emission wavelengths of the 940 nm (1-7) and the 969 nm diode for different average output powers (a). To highlight the different diode behaviors the ordinates are equally scaled. Additionally, the absorption cross-section of Yb:YAG at the corresponding wavelengths (1-7) is shown for different temperatures (b). The data in (b) was extracted from [109].

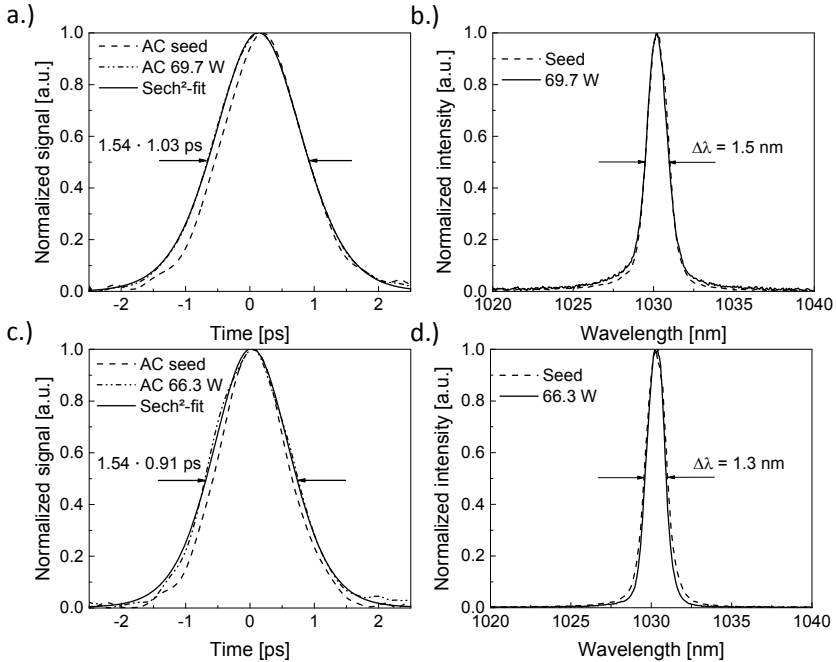


Figure 6.9: Autocorrelation traces and spectra of the seed and the amplified pulses for the experiments with the 940 nm (a,b) and the 969 nm (c,d) pump, respectively.

940 nm diode the TBP of the pulses increased slightly from 0.41 to 0.45, while it kept its value of 0.33 for the pulses amplified using the 969 nm diode. The maximum average powers in combination with the slightly different repetition rates of the seed systems of 40.7 MHz and 41.5 MHz resulted in pulse energies of $1.63 \mu\text{J}$ and $1.68 \mu\text{J}$ and pulse peak powers of 1.58 MW and 1.48 MW, respectively.

Pumping at extremely high power densities, as done in the described experiments, ultimately affects the beams transverse intensity distribution to a certain degree. Images of the beams and the beam caustics, obtained during the M^2 measurements, before and after the amplification are shown in Figure 6.10 and Figure 6.11, respectively. The numbers indicate the positions along the caustics where the images were taken. The beam caustics were obtained by introducing a focussing lens with a focal length of 75 mm into the beam paths. While the seed beams showed an almost ideal rotationally symmetric beam profile, both of the amplified beams became astigmatic to some degree. The origin of this

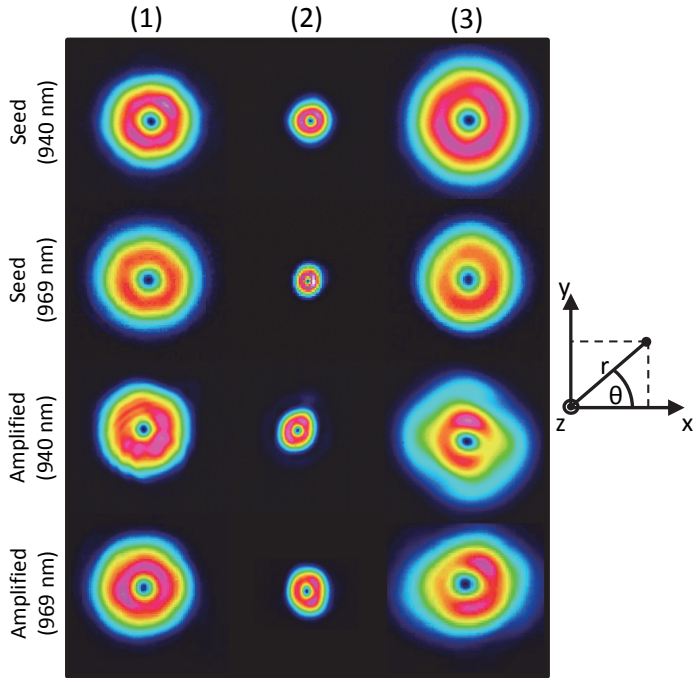


Figure 6.10: Images of the beams before and after amplification at different positions (1-3) of the caustics shown in Figure 6.11.

astigmatism could be the large temperature in the crystal, expected from the huge pump intensities, in conjunction with the two-sided asymmetric cooling scheme. Apart from the astigmatism, the doughnut shape seems most distorted in the third image (position 3) of the experiment with the 940 nm diode. Already in the second image (position 2) one can see a halo around the beam. This halo is then interfering with the amplified beam after the beam waist and causes the slightly distorted beam shape.

In general, the distortions can be attributed to two effects. First of all, the high pump power density leads to a strong thermal lens, which introduces aberrations. Additionally, the inhomogeneous gain profile across the SCF cross-section leads to further distortions of the beam profile. The origin of this effect is the following. As the pump light is guided by TIR it gets distributed across the complete crystal cross-section. Thus, also the population in the outer section of the crystal gets inverted. As a consequence of the larger intensity of the seed beam in the center of the crystal, the gain is depleted more effectively

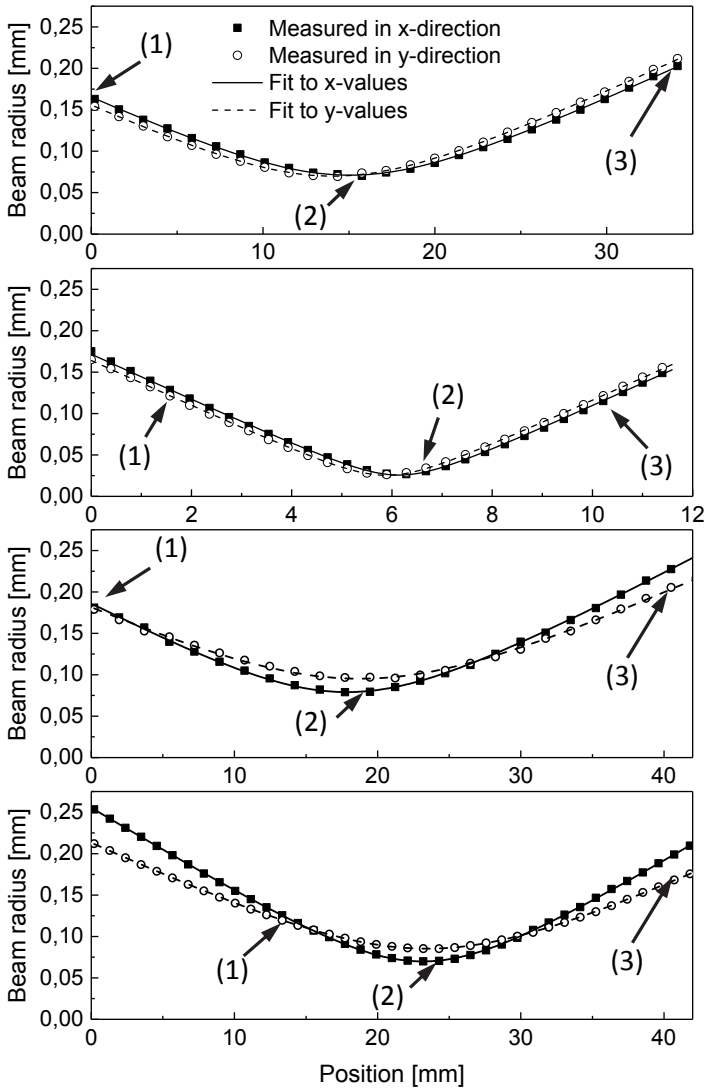


Figure 6.11: Measured radius of the beams before and after the amplification. The numbers indicate the positions of the images shown in Figure 6.10.

in the central area than in the outer parts of the crystal. Hence, the wings of the seed beam can get amplified by a larger magnitude than the center of the beam, which causes the distortions. According to the experimental and numerical investigations in [110], the effect of the thermal lens is much smaller than that resulting from the profile of the saturated gain. However, the saturated gain should be axially symmetric. Thus, as already mentioned before, the thermal effects are the most probable cause of the astigmatism of the amplified beams. Despite the distortions visible in some planes, good M^2 -values of 2.4 and 2.3 were measured for the vertical and horizontal plane of the beam amplified with the 940 nm pump. Values of 2.1 and 2.3 were determined during the experiments with the 969 nm diode.

To qualitatively assess the polarization state of the amplified beams, far field images were taken with a rotatable polarizer in front of the camera. The resultant intensity distributions are shown in Figure 6.12. The white arrows indicate the orientation of the polarization of a beam transmitted by the polarizer. In all of the images the lobes are well separated, which indicates a large polarization purity for all of the beams. However, it is apparent that the lobes at -45° are perpendicular to the orientation expected for a

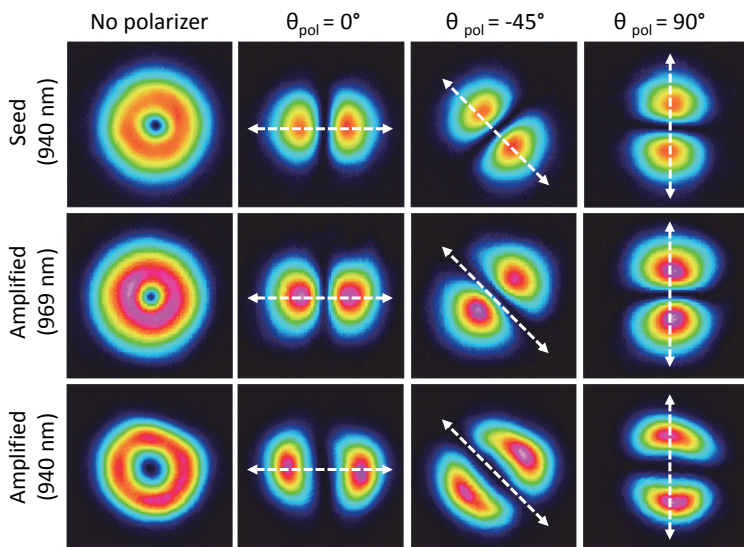


Figure 6.12: Images of the seed and the amplified beams and images of the beams with a polarizer in front of the camera. The white arrows indicate the orientation of the polarization of a beam transmitted by the polarizer.

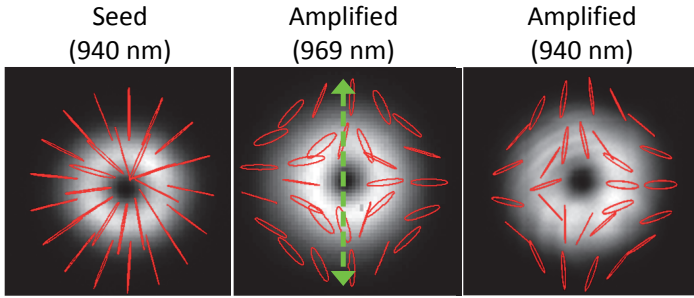


Figure 6.13: Images of the seed and the amplified beams with locally measured polarization ellipses obtained with the 2D-polarimeter. The green line indicates the required orientation of a half-wave plate used to transform the polarization state from H1 to radial.

radially polarized LG_{01}^* mode. This is due to a combined linear phase shift (between s- and p-polarized light components) of approximately 180° induced by the SCF and the subsequent dichroic mirror. The former added a phase shift of $\approx 30^\circ$, while the residual phase shift can be attributed to the latter. The effects of this phase shift are also evident in Figure 6.13 showing far field images of the beams combined with the local polarization ellipses obtained with the 2D-polarimeter. While the ellipses of the seed beam are mainly pointing to the center of the intensity distribution, they are rotated by 90° on the diagonal axes for the amplified beams. As a result the 2D-polarimeter measurements revealed that amplified beams were polarized to $96.4 \pm 1\%$ and $96.1 \pm 1\%$ in the H1 polarization for pumping at 940 nm and 969 nm, respectively. However, the H1 polarization can be transformed into the radial polarization simply by means of a half-wave plate. To prove this, a half-wave plate was introduced into the beam path of the seed right in front of the first dichroic mirror in the experiments with the 969 nm diode. The main axis of the half-wave plate was aligned parallel to the s-polarization of the incident beam (green line in Figure 6.13). At full pump power with the 969 nm pump this led to a DORP of $94 \pm 1\%$ which is close to the $96.8 \pm 1\%$ of the seed beam. The corresponding far field intensity distributions together with the measured polarization ellipses as well as the images taken with a rotatable polarizer in front of the camera can be found in Figure 6.14. The lobes are well separated, and the orientation of the polarization ellipses is close to the one expected for an ideal radially polarized mode. The other parameters, like e.g. the pulse duration or the M^2 , of the amplified beam were not affected by the phase shift compensation. It should be noted that every distortion of the polarization state due to a linear phase shift that is homogeneous across the beam cross section can be compensated

by means of a variable linear phase shifter.

6.6 Summary

This chapter discussed the experiments and the results of the amplification of a radially polarized mode-locked CVB. The beam was amplified in a high-power single-stage SCF system provided by Fibercryst SAS. The Yb:YAG crystal had a doping concentration of only 0.5 at. % to diminish detrimental thermal effects in the SCF. The standard doping concentration of the SCF crystals commercially available from Fibercryst is 1 at. %. The performance of the amplifier was compared for pumping wavelengths of 940 nm and 969 nm. As it turned out, the performance in terms of amplification was slightly better with the pump diode with an emission wavelength of 940 nm. This is different to observations made with the standard modules with the higher doping concentration [51] and might be attributed to the generally lower thermal load in the modules with lower doping concentration. Furthermore, the pump diode with a nominal emission wavelength of 969 nm actually emits light at 968.6 nm which already strongly affects the value of the respective absorption cross-section. Gain factors of approximately 5 were achieved for pump powers in the range of 500 W. Linear phase shifts in the SCF and the subsequent dichroic mirror converted the radially polarized CVB into a CVB with an H1 polarization. This was exemplarily compensated in the experiment with the 969 nm pump diode by means of a half-wave plate in front of the amplifier module. This led to a CVB with

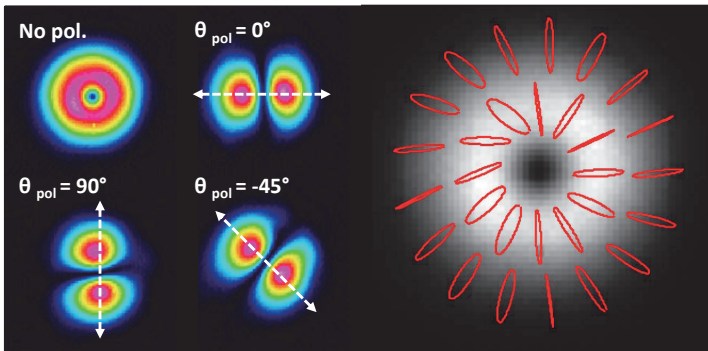


Figure 6.14: Right: Quick assessment of the polarization purity of the amplified beam with the compensated phase shift by taking images with a rotating analyzer in front of the camera. Left: Measured polarization ellipses obtained with the 2D-polarimeter.

a radially polarized output. The other parameters stayed unaffected by this measure. Overall the observed distortions of the intensity distribution and the polarization purity were acceptable and the beam would have still been a good seed beam for the TDMP amplifier. Therefore the requirements defined in the beginning of this work could be fulfilled. To give a comprehensive overview of the results, Table 6.2 lists all the relevant beam parameters before and after the amplification for the experiments with the 940 nm and 969 nm pump diode.

Table 6.2: Summary of the beam parameters (pump power P_{pump} , average output power P_{out} , gain factor, variation of the average output power ΔP_{out} , M^2 in the horizontal (h) and vertical (v) plain, pulse duration τ_p , FWHM spectral width $\Delta\lambda$, pulse energy E_p , pulse peak power \hat{P} , and radial and H1 polarization purity) before and after amplification.

	Seed (940 nm)	Amplified (940 nm)	Seed (969 nm)	Amplified (969 nm)
P_{pump} [W]	-	482	-	519
P_{out} [W]	13.3	69.7	13.3	66.3
Gain factor	5.2	-	5.0	-
ΔP_{out} [W/30 min]	-	-2.4 ± 2	-	± 0.5
M^2 (h/v)	2.1	2.3/2.4	2.0	2.3/2.1
τ_p [fs]	938	1030	800	909
$\Delta\lambda$ [nm]	1.53	1.54	1.46	1.29
TBP	0.41	0.45	0.33	0.33
f_{rep} [MHz]	41.5	41.5	40.7	40.7
E_p [μJ]	0.32	1.68	0.33	1.63
\hat{P} [MW]	0.30	1.48	0.36	1.58
Pol. purity [%]	98.7 ± 1 (R)	96.4 ± 1 (H1)	96.8 ± 1 (R)	96.1 ± 1 (H1) 94.1 ± 1 (R)

7 Summary and outlook

The aim of this work was to develop an alternative seed system for the RAZIPOL TDMP amplifier with a minimum average output power of 50 W. The focus was a reduced complexity compared to the existing system and a good quality of the CVB in terms of homogeneity of the intensity distribution and the radial polarization.

The goal was reached by starting with a mode-locked thin-disk oscillator with an CVB as an output beam. Mode-locked operation and radial polarization of the system were obtained by means of a SESAM and a GWOC, respectively. As the grating waveguide mirrors at the IFSW are usually designed to be used as the HR end mirror of the cavities, the structural parameters had to be adjusted, such that they could be used as output couplers instead. At a pump power of 61 W the oscillator reached an average output power of 13.3 W. Larger values were prevented by the onset of instabilities in the single-pulse operation and in the transverse intensity distribution. Furthermore, diffraction losses in the GWOC of 20 % to 45 % of the outcoupled light additionally limited the obtainable power. Despite this issue, an excellent slope efficiency for this type of laser of 36.9 % could be reached. The system had a pulse repetition rate of 42.1 MHz, from which a pulse energy of 316 nJ can be derived. Under the assumption of a sech²-shape of the pulse, a pulse duration of 907 fs was determined. This results in a pulse peak power of 0.31 MW. With these parameters, the system achieved an unprecedented performance in terms of average output power and pulse duration for pulsed oscillators generating CVBs. The same accounts for the homogeneity of the almost ideal doughnut-shape of the intensity distribution and the high DORP of 97 ± 1 %. The M^2 -values of the output beam were measured to be below 2.1. In terms of pulse energy, only Q-switched systems were capable to achieve higher values. A summary of the results was published in [84].

As the targeted 50 W of average output power could not be achieved solely with the oscillator, a subsequent SCF amplifier was used to increase the output power to the desired level. The performance of the SCF amplifier was investigated for two different pump diodes with nominal wavelengths of 940 nm and 969 nm. Surprisingly, the 940 nm diode resulted in a better performance regarding the average output power. At a pump power of 482 W an average output power of 69.7 W was reached, in comparison to 66.3 W at a pump power of 519 W with the 969 nm diode. Usually, one would expect an opposite behavior because of the lower thermal load in the crystal when pumping

at the zero-phonon wavelength of Yb:YAG at 969 nm. As it turned out, the behavior could be explained by the spectral shift of the diodes with increasing output powers and the thermal behavior of the two absorption lines of Yb:YAG at 940 nm and 969 nm. Despite the worse performance in terms of average output power, the experiments with the 969 nm diode showed better results with regard to the long-term stability of the output power. The measured pulse durations after the amplification were 1030 fs and 909 fs. The difference can be explained by a change in the pulse duration of the seed source between the two experiments. During the first experiment, the pulse duration of the seed source was 938 fs, whereas it was 800 fs during the second experiment. Pulse energies of $1.68 \mu\text{J}$ (940 nm) and $1.63 \mu\text{J}$ (969 nm) were achieved with corresponding pulse peak powers of 1.48 MW and 1.58 MW. The values of the M^2 in both cases increased to values in the range of 2.1-2.4. Furthermore, the beams developed a slight astigmatism and showed minor distortions of the intensity profile. As a result of a linear phase shift inside the SCF crystal and the subsequent dichroic mirror, the output beam was polarized with a DOHIP of $96.4 \pm 1 \%$ and $96.1 \pm 1 \%$ in the experiments with the 940 nm and 969 nm diode. To show that this polarization state can simply be transformed back into a radial polarization a half-wave plate was introduced into the beam path in front of the amplifier during the experiments with the 969 nm diode. This led to a good DORP of $94.1 \pm 1 \%$ without negative effects to the other performance parameters. Due to the high quality of the amplified beam in the experiments with the 969 nm diode these results were published in a Applied Physics B paper [111].

Despite the degradation of the M^2 and the DORP, the beam after the amplification is still suitable for the amplification in a TDMP amplifier. Thus the main goal of the work was reached. Nevertheless, it has to be mentioned that the system should be further optimized in case one wants to obtain optimum results. In this sense, there are several points that should be addressed. First of all the GWOCs should be further optimized to diminish the diffraction losses, which would directly increase the obtainable average output power of such a system. Secondly, as the standing wave inside the cavity has to be positioned exactly in the center of the GWOC to achieve a good polarization and beam quality, the system is extremely sensitive to misalignments of the cavity mirrors. Thus, over the course of several days readjustments to the cavity alignment were necessary, which in turn resulted in the necessity to align the subsequent amplifier setup as well. Thus, the system should be completely set up using highly stable mirror mounts, to avoid lengthy readjustments of the subsequent stages. In general, due to the lack of time, the output of the oscillator was amplified using the SCF instead of further investigating different resonator approaches. In the meantime this was done and an average output power of 125 W could be realized by Frieder Beirou et. al. with a system based on the results

outlined in the presented work [112]. This clearly shows the power scalability of the concept and proves that the investigation of such systems should be continued in the future.

Bibliography

- [1] ZHAN, Q.: *Trapping metallic Rayleigh particles with radial polarization*. Opt.Express **12** (2004) no. 15, pp. 3377.
- [2] VARIN, C.; PAYEUR, S.; MARCEAU, V.; FOURMAUX, S.; APRIL, A.; SCHMIDT, B.; FORTIN, P.-L.; THIRÉ, N.; BRABEC, T.; LÉGARÉ, F.; KIEFFER, J.-C.; PICHÉ, M.: *Direct Electron Acceleration with Radially Polarized Laser Beams*. Applied Sciences **3** (2013) no. 1, pp. 70–93.
- [3] ENDO, M.: *Sheet metal cutting with a 2 kW radially polarized CO₂ laser*. SPIE, 2010, pp. 77511B–77511B–9 (SPIE Proceedings).
- [4] ONUSEIT, V.; ABDOU AHMED, M.; WEBER, R.; GRAF, T.: *Space-resolved Spectrometric Measurements of the Cutting Front*. Physics Procedia **12** (2011), pp. 584–590.
- [5] MEIER, M.; ROMANO, V.; FEURER, T.: *Material processing with pulsed radially and azimuthally polarized laser radiation*. Appl. Phys. A **86** (2007) no. 3, pp. 329–334.
- [6] QUABIS, S.; DORN, R.; EBERLER, M.; GLÖCKL, O.; LEUCHS, G.: *Focusing light to a tighter spot*. Optics Communications **179** (2000) no. 1-6, pp. 1–7.
- [7] DORN, R.; QUABIS, S.; LEUCHS, G.: *Sharper Focus for a Radially Polarized Light Beam*. Phys. Rev. Lett. **91** (2003) no. 23.
- [8] ZHAN, Q.; LEGER, J.: *Focus shaping using cylindrical vector beams*. Opt.Express **10** (2002) no. 7, pp. 324.
- [9] VARIN, C.; PICHÉ, M.; PORRAS, M. A.: *Acceleration of electrons from rest to GeV energies by ultrashort transverse magnetic laser pulses in free space*. Physical Review E **71** (2005) no. 2.
- [10] SALAMIN, Y. I.; HARMAN, Z.; KEITEL, C. H.: *Direct High-Power Laser Acceleration of Ions for Medical Applications*. Phys. Rev. Lett. **100** (2008) no. 15.
- [11] LIU, J.-L.; SHENG, Z. M.; ZHENG, J.; LIU, C. S.; ZHANG, J.: *Proton acceleration by radially polarized chirped laser pulses*. Physical Review Special Topics - Accelerators and Beams **15** (2012) no. 4.
- [12] NIZIEV, V. G.; NESTEROV, A. V.: *Influence of beam polarization on laser cutting efficiency*. J. Phys. D: Appl. Phys. **32** (1999) no. 13, pp. 1455–1461.
- [13] KRAUS, M.; ABDOU AHMED, M.; MICHALOWSKI, A.; VOSS, A.; WEBER, R.; GRAF, T.: *Microdrilling in steel using ultrashort pulsed laser beams with radial*

- and azimuthal polarization*. Optics express **18** (2010) no. 21, pp. 22305–22313.
- [14] HNATOVSKY, C.; SHVEDOV, V. G.; KROLIKOWSKI, W.: *The role of light-induced nanostructures in femtosecond laser micromachining with vector and scalar pulses*. Opt.Express **21** (2013) no. 10, pp. 12651.
- [15] ENDO, M.; ARAYA, N.; KUROKAWA, Y.; UNO, K.: *Anomalous enhancement of drilling rate in carbon fiber reinforced plastic using azimuthally polarized CO₂ laser*. Laser Physics **26** (2016) no. 9, pp. 096001.
- [16] ANOOP, K. K.; FITTIPALDI, R.; RUBANO, A.; WANG, X.; PAPARO, D.; VECCHIONE, A.; MARRUCCI, L.; BRUZZESE, R.; AMORUSO, S.: *Direct femtosecond laser ablation of copper with an optical vortex beam*. J. Appl. Phys. **116** (2014) no. 11, pp. 113102.
- [17] [HTTP://WWW.RAZIPOL.EU/](http://www.razipol.eu/) .
- [18] SCHAWLOW, A. L.; TOWNES, C. H.: *Infrared and Optical Masers*. Physical Review **112** (1958) no. 6, pp. 1940–1949.
- [19] MARCATILI, E. A. J.; SCHMELTZER, R. A.: *Hollow Metallic and Dielectric Waveguides for Long Distance Optical Transmission and Lasers*. Bell System Technical Journal **43** (1964) no. 4, pp. 1783–1809.
- [20] POHL, D.: *Operation of a Ruby Laser in the Purely Transverse Electric Mode TE₀₁*. Appl. Phys. Lett. **20** (1972) no. 7, pp. 266–267.
- [21] MUSHIAKE, Y.; MATSUMURA, K.; NAKAJIMA, N.: *Generation of radially polarized optical beam mode by laser oscillation*. Proceedings of the IEEE **60** (1972) no. 9, pp. 1107–1109.
- [22] TIDWELL, S. C.; KIM, G. H.; KIMURA, W. D.: *Efficient radially polarized laser beam generation with a double interferometer*. Applied optics **32** (1993) no. 27, pp. 5222–5229.
- [23] STALDER, M.; SCHADT, M.: *Linearly polarized light with axial symmetry generated by liquid-crystal polarization converters*. Opt.Lett. **21** (1996) no. 23, pp. 1948.
- [24] [HTTP://WWW.ARCOPTIX.COM/RADIAL_POLARIZATION_CONVERTER.HTM](http://www.arcoptix.com/radial_polarization_converter.htm): .
- [25] [HTTP://WWW.ALTECHNA.DE/PRODUCT_DETAILS.PHP?ID=1048](http://www.altechna.de/product_details.php?id=1048): 07.03.2017.
- [26] BERESNA, M.; GECEVIČIUS, M.; KAZANSKY, P. G.; GERTUS, T.: *Radially polarized optical vortex converter created by femtosecond laser nanostructuring of glass*. Appl. Phys. Lett. **98** (2011) no. 20, pp. 201101.
- [27] MACHAVARIANI, G.; LUMER, Y.; MOSHE, I.; MEIR, A.; JACKEL, S.: *Efficient extracavity generation of radially and azimuthally polarized beams*. Opt.Lett. **32** (2007) no. 11, pp. 1468.
- [28] ITO, A.; KOZAWA, Y.; SATO, S.: *Selective oscillation of radially and azimuthally polarized laser beam induced by thermal birefringence and lensing*. Journal of the Optical Society of America B **26** (2009) no. 4, pp. 708.

- [29] MACHAVARIANI, G.; LUMER, Y.; MOSHE, I.; MEIR, A.; JACKEL, S.; DAVIDSON, N.: *Birefringence-induced bifocusing for selection of radially or azimuthally polarized laser modes*. Applied Optics **46** (2007) no. 16, pp. 3304.
- [30] KOECHNER, W.: *Solid-state laser engineering*, 5. ed. New York: Springer, 1999 (Springer series in optical sciences vol. v. 1).
- [31] MOSHE, I.; JACKEL, S.; MEIR, A.: *Production of radially or azimuthally polarized beams in solid-state lasers and the elimination of thermally induced birefringence effects*. Opt.Lett. **28** (2003) no. 10, pp. 807.
- [32] MOSHE, I.; JACKEL, S.; MEIR, A.; LUMER, Y.; LEIBUSH, E.: *2kW, $M^2 < 10$ radially polarized beams from aberration-compensated rod-based Nd:YAG lasers*. Opt.Lett. **32** (2007) no. 1, pp. 47.
- [33] ENDO, M.: *Azimuthally polarized 1 kW CO₂ laser with a triple-axicon retroreflector optical resonator*. Opt.Lett. **33** (2008) no. 15, pp. 1771.
- [34] LI, B.; HU, Y.; HU, Y.; ZHAO, J.: *1.5 kW radially polarized beam irradiated from a FAF CO₂ laser based on an intracavity triple-axicon retroreflector and quarter wave phase retarders*. Applied Optics **56** (2017) no. 12, pp. 3383.
- [35] MOSER, T.; BALMER, J.; DELBEKE, D.; MUYS, P.; VERSTUYFT, S.; BAETS, R.: *Intracavity generation of radially polarized CO₂ laser beams based on a simple binary dielectric diffraction grating*. Applied Optics **45** (2006) no. 33, pp. 8517.
- [36] ABDOU AHMED, M.; SCHULZ, J.; VOSS, A.; PARRIAUX, O.; POMMIER, J.-C.; GRAF, T.: *Radially polarized 3 kW beam from a CO₂ laser with an intracavity resonant grating mirror*. Opt.Lett. **32** (2007) no. 13, pp. 1824.
- [37] DIETRICH, T.; RUMPEL, M.; LIWEI, F.; PRUSS, C.; OSTEN, W.; ABDOU AHMED, M.; GRAF, T.: *CW thin-disk laser emitting kW-class beams with radial polarization*. CLEO/Europe-EQEC 2017 (2017).
- [38] KÄMPFE, T.; TONCHEV, S.; TISHCHENKO, A. V.; GERGOV, D.; PARRIAUX, O.: *Azimuthally polarized laser mode generation by multilayer mirror with wideband grating-induced TM leakage in the TE stopband*. Opt.Express **20** (2012) no. 5, pp. 5392.
- [39] ZHAO, J.; LI, B.; ZHAO, H.; WANG, W.; HU, Y.; LIU, S.; WANG, Y.: *Generation of azimuthally polarized beams in fast axial flow CO₂ laser with hybrid circular subwavelength grating mirror*. Applied optics **53** (2014) no. 17, pp. 3706–3711.
- [40] KOZAWA, Y.; SATO, S.; SATO, T.; INOUE, Y.; OHTERA, Y.; KAWAKAMI, S.: *Cylindrical Vector Laser Beam Generated by the Use of a Photonic Crystal Mirror*. Applied Physics Express **1** (2008), pp. 022008.
- [41] ENDERLI, F.; FEURER, T.: *Radially polarized mode-locked Nd:YAG laser*.

- Opt.Lett. **34** (2009) no. 13, pp. 2030.
- [42] JIANHONG, H.; JING, D.; YONGGE, C.; WEN, W.; HUI, Z.; JINHUI, L.; FEI, S.; YAN, G.; SHUTAO, D.; WENXIONG, L.: *Passively mode-locked radially polarized laser based on ceramic Nd:YAG rod*. Optics express **19** (2011) no. 3, pp. 2120–2125.
- [43] LI, L.; REN, Z.; CHEN, X.; QI, M.; ZHENG, X.; BAI, J.; SUN, Z.: *Passively Mode-Locked Radially Polarized Nd-Doped Yttrium Aluminum Garnet Laser Based on Graphene-Based Saturable Absorber*. Applied Physics Express **6** (2013) no. 8, pp. 082701.
- [44] SUN, B.; WANG, A.; GU, C.; CHEN, G.; XU, L.; CHUNG, D.; ZHAN, Q.: *Mode-locked all-fiber laser producing radially polarized rectangular pulses*. Opt.Lett. **40** (2015) no. 8, pp. 1691–1694.
- [45] TSAI, S.-Y.; CHIU, C.-P.; CHANG, K.-C.; WEI, M.-D.: *Periodic and chaotic dynamics in a passively Q-switched Nd:GdVO₄ laser with azimuthal polarization*. Opt.Lett. **41** (2016) no. 5, pp. 1054–1057.
- [46] HONG, K.-G.; HUNG, B.-J.; LIN, S.-T.; WEI, M.-D.: *Q-switched mode-locked and azimuthally polarized Nd: GdVO₄ laser with semiconductor saturable absorber mirror*. Japanese Journal of Applied Physics **55** (2016) no. 6, pp. 060303.
- [47] MOSHE, I.; JACKEL, S.; LUMER, Y.; MEIR, A.; FELDMAN, R.; SHIMONY, Y.: *Use of polycrystalline Nd:YAG rods to achieve pure radially or azimuthally polarized beams from high-average-power lasers*. Opt.Lett. **35** (2010) no. 15, pp. 2511–2513.
- [48] KANAZAWA, S.; KOZAWA, Y.; SATO, S.: *High-power and highly efficient amplification of a radially polarized beam using an Yb-doped double-clad fiber*. Opt.Lett. **39** (2014) no. 10, pp. 2857–2859.
- [49] PIEHLER, S.; DÉLEN, X.; RUMPEL, M.; DIDIERJEAN, J.; AUBRY, N.; GRAF, T.; BALEMBOIS, F.; GEORGES, P.; ABDOU AHMED, M.: *Amplification of cylindrically polarized laser beams in single crystal fiber amplifiers*. Optics express **21** (2013) no. 9, pp. 11376–11381.
- [50] LOESCHER, A.; NEGEL, J.-P.; GRAF, T.; ABDOU AHMED, M.: *Radially polarized emission with 635 W of average power and 21 mJ of pulse energy generated by an ultrafast thin-disk multipass amplifier*. Opt.Lett. **40** (2015) no. 24, pp. 5758.
- [51] LESPARRE, F.; GOMES, J. T.; DÉLEN, X.; MARTIAL, I.; DIDIERJEAN, J.; PALLMANN, W.; RESAN, B.; ECKERLE, M.; GRAF, T.; ABDOU AHMED, M.; DRUON, F.; BALEMBOIS, F.; GEORGES, P.: *High-power Yb:YAG single-crystal fiber amplifiers for femtosecond lasers in cylindrical polarization*. Opt.Lett. **40** (2015) no. 11, pp. 2517.
- [52] NEGEL, J.-P.; VOSS, A.; ABDOU AHMED, M.; BAUER, D.; SUTTER, D.; KILLI,

- A.; GRAF, T.: *1.1 kW average output power from a thin-disk multipass amplifier for ultrashort laser pulses*. Opt.Lett. **38** (2013) no. 24, pp. 5442–5445.
- [53] NEGEL, J.-P.: *Scheibenlaser-Multipassverstärker für ultrakurze Laserpulse mit Ausgangsleistungen im kW-Bereich*. Stuttgart: Institut für Strahlwerkzeuge, 2016. Universität Stuttgart, dissertation.
- [54] MOSER, T.; GLUR, H.; ROMANO, V.; PIGEON, F.; PARRIAUX, O.; ABDU AHMED, M.; GRAF, T.: *Polarization-selective grating mirrors used in the generation of radial polarization*. Appl. Phys. B **80** (2005) no. 6, pp. 707–713.
- [55] PRONIN, O.; BRONS, J.; GRASSE, C.; PERVAK, V.; BOEHM, G.; AMANN, M.-C.; KALASHNIKOV, V. L.; APOLONSKI, A.; KRAUSZ, F.: *High-power 200 fs Kerr-lens mode-locked Yb:YAG thin-disk oscillator*. Opt.Lett. **36** (2011) no. 24, pp. 4746.
- [56] KELLER, U.; WEINGARTEN, K. J.; KARTNER, F. X.; KOPF, D.; BRAUN, B.; JUNG, I. D.; FLUCK, R.; HONNINGER, C.; MATUSCHEK, N.; AUS DER AU, J.: *Semiconductor saturable absorber mirrors (SESAM's) for femtosecond to nanosecond pulse generation in solid-state lasers*. IEEE Journal of Selected Topics in Quantum Electronics **2** (1996) no. 3, pp. 435–453.
- [57] SNITZER, E.: *Optical Maser Action of Nd⁺³ in a Barium Crown Glass*. Phys. Rev. Lett. **7** (1961) no. 12, pp. 444–446.
- [58] KANE, T.; ECKARDT, R.; BYER, R.: *Reduced thermal focusing and birefringence in zig-zag slab geometry crystalline lasers*. IEEE Journal of Quantum Electronics **19** (1983) no. 9, pp. 1351–1354.
- [59] GIESEN, A.; HÜGEL, H.; VOSS, A.; WITTIG, K.; BRAUCH, U.; OPOWER, H.: *Scalable concept for diode-pumped high-power solid-state lasers*. Appl. Phys. B **58** (1994) no. 5, pp. 365–372.
- [60] SMITH, C. R.; BEECHER, S. J.; MACKENZIE, J. I.; CLARKSON, W. A.: *Amplification of a radially polarised beam in an Yb:YAG thin-slab*. Appl. Phys. B **123** (2017) no. 8, pp. 043402.
- [61] CHENG, W.: *Optical vortex beams: Generation, propagation and applications*. 2013. University of Dayton, dissertation.
- [62] MAURER, C.; JESACHER, A.; FÜRHAPTER, S.; BERNET, S.; RITSCH-MARTE, M.: *Tailoring of arbitrary optical vector beams*. New Journal of Physics **9** (2007) no. 3, pp. 78.
- [63] MILONNI, P. W.; EBERLY, J. H.: *Laser physics*, 2. ed. Hoboken (N.J.): Wiley, op. 2010.
- [64] SALEH, BAHAA E. A.; TEICH, M. C.: *Fundamentals of photonics*, 2. ed. Hoboken and N.J: Wiley-Interscience, 2009, ©2007 (Wiley series in pure and applied optics).

- [65] ZHAN, Q.: *Cylindrical vector beams: from mathematical concepts to applications*. Advances in Optics and Photonics **1** (2009) no. 1, pp. 1.
- [66] GORI, F.: *Polarization basis for vortex beams*. Journal of the Optical Society of America A **18** (2001) no. 7, pp. 1612.
- [67] BORGHI, R.; SANTARSIERO, M.: *Nonparaxial propagation of spirally polarized optical beams*. Journal of the Optical Society of America A **21** (2004) no. 10, pp. 2029.
- [68] VOSS, A.; ABDOU AHMED, M.; GRAF, T.: *Application of the extended Jones matrix formalism for higher-order transverse modes to laser resonators*. Optics express **18** (2010) no. 21, pp. 21540–21550.
- [69] VYAS, S.; KOZAWA, Y.; SATO, S.: *Polarization singularities in superposition of vector beams*. Optics express **21** (2013) no. 7, pp. 8972–8986.
- [70] DI LIN; DANIEL, J.; GECEVIČIUS, M.; BERESNA, M.; KAZANSKY, P. G.; CLARKSON, W. A.: *Cladding-pumped ytterbium-doped fiber laser with radially polarized output*. Opt.Lett. **39** (2014) no. 18, pp. 5359.
- [71] BEIROW, F.: *Camera based polarimeter for the characterization of laser optics and laser beams*. University of Stuttgart, master thesis, 2014.
- [72] VOSS, A.; ABDOU AHMED, M.; GRAF, T.: *Extension of the Jones matrix formalism to higher-order transverse modes*. Opt.Lett. **32** (2007) no. 1, pp. 83.
- [73] HECHT, E.: *Optics*, 4. ed. Reading and Mass: Addison-Wesley, op. 2002.
- [74] COLLETT, E.: *Field Guide to Polarization*. 1000 20th Street and Bellingham and WA 98227-0010 USA: SPIE, 2005.
- [75] BOMZON, Z.; BIENER, G.; KLEINER, V.; HASMAN, E.: *Radially and azimuthally polarized beams generated by space-variant dielectric subwavelength gratings*. Opt.Lett. **27** (2002) no. 5, pp. 285.
- [76] HAIML, M.; GRANGE, R.; KELLER, U.: *Optical characterization of semiconductor saturable absorbers*. Appl. Phys. B **79** (2004) no. 3, pp. 331–339.
- [77] SARACENO, C. J.; SCHRIEBER, C.; MANGOLD, M.; HOFFMANN, M.; HECKL, O. H.; BAER, C. R.; GOLLING, M.; SÜDMEYER, T.; KELLER, U.: *SESAMs for High-Power Oscillators: Design Guidelines and Damage Thresholds*. IEEE Journal of Selected Topics in Quantum Electronics **18** (2012) no. 1, pp. 29–41.
- [78] SIEGMAN, A. E.: *How to (Maybe) Measure Laser Beam Quality*. In: Diode Pumped Solid State Lasers: Applications and Issues. , p. MQ1.
- [79] ABDOU AHMED, M.; HAEFNER, M.; VOGEL, M.; PRUSS, C.; VOSS, A.; OSTEN, W.; GRAF, T.: *High-power radially polarized Yb:YAG thin-disk laser with high efficiency*. Optics express **19** (2011) no. 6, pp. 5093–5104.
- [80] MÜLLER, L.: *Investigations on grating waveguide structures in thin-disk lasers*. Institut für Strahlwerkzeuge, 2017. Universität Stuttgart, dissertation.

- [81] ABDOU AHMED, M.; VOSS, A.; VOGEL, M. M.; GRAF, T.: *Multilayer polarizing grating mirror used for the generation of radial polarization in Yb: YAG thin-disk lasers*. Opt.Lett. **32** (2007) no. 22, pp. 3272.
- [82] <https://www.newport.com/ffberekswaveplates>. 09.11.2016.
- [83] CONTAG, K.: *Modellierung und numerische Auslegung des Yb:YAG-Scheibenlasers*. München: Utz, Wiss., 2002 (Laser in der Materialbearbeitung).
- [84] ECKERLE, M.; DIETRICH, T.; SCHAAL, F.; PRUSS, C.; OSTEN, W.; ABDU AHMED, M.; GRAF, T.: *Novel thin-disk oscillator concept for the generation of radially polarized femtosecond laser pulses*. Opt.Lett. **41** (2016) no. 7, pp. 1680.
- [85] MOLLENAUER, L. F.; STOLEN, R. H.: *The soliton laser*. Opt.Lett. **9** (1984) no. 1, pp. 13.
- [86] GRAF, T.: *Laser: Grundlagen der Laserstrahlquellen*, 1. ed. Wiesbaden: Vieweg + Teubner, 2009 (Studium).
- [87] HÖNNINGER, C.; PASCHOTTA, R.; MORIER-GENOUD, F.; MOSER, M.; KELLER, U.: *Q-switching stability limits of continuous-wave passive mode locking*. Journal of the Optical Society of America B **16** (1999) no. 1, pp. 46.
- [88] INNERHOFER, E.; SÜDMEYER, T.; BRUNNER, F.; HÄRING, R.; ASCHWANDEN, A.; PASCHOTTA, R.; HÖNNINGER, C.; KUMKAR, M.; KELLER, U.: *60-W average power in 810-fs pulses from a thin-disk Yb:YAG laser*. Opt.Lett. **28** (2003) no. 5, pp. 367.
- [89] SARACENO, C. J.; EMAURY, F.; SCHRIEBER, C.; HOFFMANN, M.; GOLLING, M.; SÜDMEYER, T.; KELLER, U.: *Ultrafast thin-disk laser with 80 μJ pulse energy and 242 W of average power*. Opt.Lett. **39** (2014) no. 1, pp. 9.
- [90] BAUER, D.; ZAWISCHA, I.; SUTTER, D. H.; KILLI, A.; DEKORSY, T.: *Mode-locked Yb:YAG thin-disk oscillator with 41 μJ pulse energy at 145 W average infrared power and high power frequency conversion*. Optics express **20** (2012) no. 9, pp. 9698–9704.
- [91] HAUS, H. A.; FUJIMOTO, J. G.; IPPEN, E. P.: *Structures for additive pulse mode locking*. Journal of the Optical Society of America B **8** (1991) no. 10, pp. 2068.
- [92] KÄRTNER, F. X.; DER AU, J. A.; KELLER, U.: *Mode-locking with slow and fast saturable absorbers-what's the difference?* IEEE Journal of Selected Topics in Quantum Electronics **4** (1998) no. 2, pp. 159–168.
- [93] SCHLATTER, A.; ZELLER, S. C.; GRANGE, R.; PASCHOTTA, R.; KELLER, U.: *Pulse-energy dynamics of passively mode-locked solid-state lasers above the Q-switching threshold*. Journal of the Optical Society of America B **21** (2004) no. 8, pp. 1469.
- [94] EICHLER, J.; DÜNKEL, L.; EPPICH, B.: *Die Strahlqualität von Lasern – Wie bestimmt man Beugungsmaßzahl und Strahldurchmesser in der Praxis?* Laser

- Technik Journal **1** (2004) no. 2, pp. 63–66.
- [95] DI LIN; XIA, K.; LI, R.; LI, X.; LI, G.; UEDA, K.-I.; LI, J.: *Radially polarized and passively Q-switched fiber laser*. Opt.Lett. **35** (2010) no. 21, pp. 3574–3576.
- [96] ZOU, L.; YAO, Y.; HAN, X.; LIU, J.; XU, Y.; LI, J.: *Azimuthally polarized, passively Q-switched Yb-doped fiber laser*. Optics Communications **355** (2015), pp. 181–185.
- [97] ZHOU, Y.; LIN, J.; ZHANG, X.; XU, L.; GU, C.; SUN, B.; WANG, A.; ZHAN, Q.: *Self-starting passively mode-locked all fiber laser based on carbon nanotubes with radially polarized emission*. Photonics Research **4** (2016) no. 6, pp. 327.
- [98] ZHOU, Y.; WANG, A.; GU, C.; SUN, B.; XU, L.; LI, F.; CHUNG, D.; ZHAN, Q.: *Actively mode-locked all fiber laser with cylindrical vector beam output*. Opt.Lett. **41** (2016) no. 3, pp. 548–550.
- [99] <http://fibercryst.com/>. 09.11.2016.
- [100] BOYD, R. W.: *Nonlinear optics*, 3. ed. Amsterdam: Elsevier/Academic Press, 2008.
- [101] <https://refractiveindex.info/?shelf=main&book=Y3A15O12&page=Zelmon>. 16.10.2017.
- [102] YASUKI TAKEUCHI; JUNJI KAWANAKA; MASAYUKI FUJITA: *Nonlinear refractive index of a YAG crystal at low temperature*. In: 11th European Quantum Electronics Conference (CLEO/EQEC). , p. 1.
- [103] SMITH, A. V.; GEHR, R. J.; BOWERS, M. S.: *Numerical models of broad-bandwidth nanosecond optical parametric oscillators*. Journal of the Optical Society of America B **16** (1999) no. 4, pp. 609.
- [104] SZIKLAS, E. A.; SIEGMAN, A. E.: *Mode calculations in unstable resonators with flowing saturable gain. 2: Fast Fourier transform method*. Applied optics **14** (1975) no. 8, pp. 1874–1889.
- [105] DÉLEN, X.; ZAOUTER, Y.; MARTIAL, I.; AUBRY, N.; DIDIERJEAN, J.; HÖNNINGER, C.; MOTTAY, E.; BALEMBOIS, F.; GEORGES, P.: *Yb:YAG single crystal fiber power amplifier for femtosecond sources*. Opt.Lett. **38** (2013) no. 2, pp. 109–111.
- [106] KIENEL, M.; MÜLLER, M.; DEMMLER, S.; ROTHHARDT, J.; KLENKE, A.; EIDAM, T.; LIMPET, J.; TÜNNERMANN, A.: *Coherent beam combination of Yb:YAG single-crystal rod amplifiers*. Opt.Lett. **39** (2014) no. 11, pp. 3278–3281.
- [107] LESPARRE, F.; GOMES, J. T.; DÉLEN, X.; MARTIAL, I.; DIDIERJEAN, J.; PALLMANN, W.; RESAN, B.; DRUON, F.; BALEMBOIS, F.; GEORGES, P.: *Yb:YAG single-crystal fiber amplifiers for picosecond lasers using the divided pulse amplification technique*. Opt.Lett. **41** (2016) no. 7, pp. 1628.
- [108] DÉLEN, X.: *Amplificateurs laser à cristaux massifs pompés par diode : fibres*

- crystallines Yb:YAG et cristaux Nd:YVO₄*. Paris: Laboratoire Charles Fabry de l'Institut d'Optique, 2013. UNIVERSITÉ PARIS-SUD XI, dissertation.
- [109] KOERNER, J.; VORHOLT, C.; LIEBETRAU, H.; KAHLE, M.; KLOEPFEL, D.; SEIFERT, R.; HEIN, J.; KALUZA, M. C.: *Measurement of temperature-dependent absorption and emission spectra of Yb:YAG, Yb:LuAG, and Yb:CaF₂ between 20 °C and 200 °C and predictions on their influence on laser performance*. Journal of the Optical Society of America B **29** (2012) no. 9, pp. 2493.
- [110] ALBRODT, P. R.: *Investigation of beam distortions in high power end-pumped bulk laser amplifiers*. Universität Stuttgart, master thesis, 2016.
- [111] ECKERLE, M.; BEIROW, F.; DIETRICH, T.; SCHAAL, F.; PRUSS, C.; OSTEN, W.; AUBRY, N.; PERRIER, M.; DIDIERJEAN, J.; DÉLEN, X.; BALEMBOIS, F.; GEORGES, P.; ABDOU AHMED, M.; GRAF, T.: *High-power single-stage single-crystal Yb:YAG fiber amplifier for radially polarized ultrashort laser pulses*. Appl. Phys. B **123** (2017) no. 5.
- [112] BEIROW, F.; ECKERLE, M.; DANNECKER, B.; DIETRICH, T.; ABDOU AHMED, M.; GRAF, T.: *Radially polarized passively mode-locked thin-disk laser oscillator emitting sub-picosecond pulses with an average output power exceeding the 100 W level*. Opt.Express **26** (2018) no. 4, pp. 4401.

Acknowledgements

The final words of this thesis I want to dedicate to the people that made this work possible by supporting me in different ways during all these years.

First, I want to express my sincere gratitude to Prof. Dr. phil. nat. Graf for his continuous support. His scientific input always pushed me to further improve my results.

Besides, I want to thank Prof. Dr.-Ing. Bertho for being part of my thesis committee.

I also want to thank Prof. Dr.-Ing. Rohr and the GSaME for taking over my scholarship and for the interesting advanced training their program offered.

Furthermore, I want to thank Dr. Marwan Abdou Ahmed with whom I had plenty of fruitful discussions regarding CVBs and without whom I would have never been able to write this thesis. His deep insight into the topic made it possible to achieve the presented results.

A special thanks goes to all my former colleagues at the IFSW, in particularly to my former office mates Benjamin Dannecker, Jan-Hinnerk Wolter and Xavier Délen with whom I had hundreds of scientific discussions on various topics, which in the end made me a better scientist. Special thanks also goes to Frieder Beirow, Tom Dietrich and Martin Rumpel who supported me in the lab in different ways.

I also want to thank my former supervisors Dr. Siegfried Nau and Dr. Marc Eichhorn. Both of them are to a large extent responsible for my decision to do a PhD as both of them always kept pushing me onwards and thereby ignited my scientific interest.

Finally, my biggest thanks goes to my girlfriend Melanie and my family who always supported me throughout these years. Their support kept me going even when generating good results took much longer than I was hoping for. Without them writing this thesis would not have been possible!

Cologne, June 2018

Michael Eckerle

Laser in der Materialbearbeitung

Forschungsberichte des IFSW (Institut für Strahlwerkzeuge)

Herausgegeben von

Prof. Dr.-Ing. habil. Helmut Hügel, Universität Stuttgart

Forschungsberichte des IFSW von 1992 bis 1999 erschienen im Teubner Verlag, Stuttgart

Zoske, Uwe

Modell zur rechnerischen Simulation von Laserresonatoren und Strahlführungssystemen
1992, 186 Seiten, ISBN 3-519-06205-4

Gorritz, Michael

Adaptive Optik und Sensorik im Strahlführungssystem von Laserbearbeitungsanlagen
1992, vergriffen, ISBN 3-519-06206-2

Mohr, Ursula

Geschwindigkeitsbestimmende Strahleigenschaften und Einkoppelmechanismen beim CO₂-Laserschneiden von Metallen
1993, 130 Seiten, ISBN 3-519-06207-0

Rudlaff, Thomas

Arbeiten zur Optimierung des Umwandlungshärtens mit Laserstrahlen
1993, 152 Seiten, ISBN 3-519-06208-9

Borik, Stefan

Einfluß optischer Komponenten auf die Strahlqualität von Hochleistungslasern
1993, 200 Seiten, ISBN 3-519-06209-7

Paul, Rüdiger

Optimierung von HF-Gasentladungen für schnell längsgeströmte CO₂-Laser
1994, 149 Seiten, ISBN 3-519-06210-0

Wahl, Roland

Robotergeführtes Laserstrahlschweißen mit Steuerung der Polarisationsrichtung
1994, 150 Seiten, ISBN 3-519-06211-9

Frederking, Klaus-Dieter

Laserlöten kleiner Kupferbauteile mit geregelter Lotdrahtzufuhr
1994, 139 Seiten, ISBN 3-519-06212-7

Grünewald, Karin M.

Modellierung der Energietransferprozesse in längsgeströmten CO₂-Lasern
1994, 158 Seiten, ISBN 3-519-06213-5

Shen, Jialin

Optimierung von Verfahren der Laseroberflächenbehandlung mit gleichzeitiger Pulverzufuhr
1994, 160 Seiten, ISBN 3-519-06214-3

Arnold, Johannes M.

Abtragen metallischer und keramischer Werkstoffe mit Excimerlasern
1994, 192 Seiten, ISBN 3-519-06215-1

Holzwarth, Achim

Ausbreitung und Dämpfung von Stoßwellen in Excimerlasern
1994, 153 Seiten, ISBN 3-519-06216-X

Dausinger, Friedrich

Strahlwerkzeug Laser: Energieeinkopplung und Prozesseffektivität
1995, 143 Seiten, ISBN 3-519-06217-8

Meiners, Eckhard

Abtragende Bearbeitung von Keramiken und Metallen mit gepulstem Nd:YAG-Laser als zweistufiger Prozeß
1995, 120 Seiten, ISBN 3-519-06222-4

Beck, Markus

Modellierung des Lasertiefschweißens
1996, 160 Seiten, ISBN 3-519-06218-6

Breining, Klaus

Auslegung und Vermessung von Gasentladungsstrecken für CO₂-Hochleistungslaser
1996, 131 Seiten, ISBN 3-519-06219-4

Griebsch, Jürgen

Grundlagenuntersuchungen zur Qualitätssicherung beim gepulsten Lasertiefschweißen
1996, 133 Seiten, ISBN 3-519-06220-8

Krepulat, Walter

Aerodynamische Fenster für industrielle Hochleistungslaser
1996, 144 Seiten, ISBN 3-519-06221-6

Xiao, Min

Vergleichende Untersuchungen zum Schneiden dünner Bleche mit CO₂- und Nd:YAG-Lasern
1996, 118 Seiten, ISBN 3-519-06223-2

Glumann, Christiane

Verbesserte Prozeßsicherheit und Qualität durch Strahlkombination beim Laserschweißen
1996, 143 Seiten, ISBN 3-519-06224-0

Gross, Herbert

Propagation höhermodiger Laserstrahlung und deren Wechselwirkung mit optischen Systemen
1996, 191 Seiten, ISBN 3-519-06225-9

Rapp, Jürgen

Laserschweißtauglichkeit von Aluminiumwerkstoffen für Anwendungen im Leichtbau
1996, 202 Seiten, ISBN 3-519-06226-7

Wittig, Klaus

Theoretische Methoden und experimentelle Verfahren zur Charakterisierung von Hochleistungslaserstrahlung
1996, 198 Seiten, ISBN 3-519-06227-5

Grünenwald, Bernd

Verfahrensoptimierung und Schichtcharakterisierung beim einstufigen Cermet-Beschichten mittels CO₂-Hochleistungslaser
1996, 160 Seiten, ISBN 3-519-06229-1

Lee, Jae-Hoon

Laserverfahren zur strukturierten Metallisierung
1996, 154 Seiten, ISBN 3-519-06232-1

Albinus, Uwe N. W.

Metallisches Beschichten mittels PLD-Verfahren
1996, 144 Seiten, ISBN 3-519-06233-X

Wiedmaier, Matthias

Konstruktive und verfahrenstechnische Entwicklungen zur Komplettbearbeitung in Drehzentren mit integrierten Laserverfahren
1997, 129 Seiten, ISBN 3-519-06228-3

Bloehs, Wolfgang

Laserstrahlhärten mit angepassten Strahlformungssystemen
1997, 143 Seiten, ISBN 3-519-06230-5

Bea, Martin

Adaptive Optik für die Materialbearbeitung mit CO₂-Laserstrahlung
1997, 143 Seiten, ISBN 3-519-06231-3

Stöhr, Michael

Beeinflussung der Lichtemission bei mikrokanalgekühlten Laserdioden
1997, 147 Seiten, ISBN 3-519-06234-8

Pließ, Wilfried

Zerstörungsschwellen und Degradation von CO₂-Laseroptiken
1998, 158 Seiten, ISBN 3-519-06235-6

Schaller, Markus K. R.

Lasergestützte Abscheidung dünner Edelmetallschichten zum Heißgaskorrosionsschutz für Molybdän
1998, 163 Seiten, ISBN 3-519-06236-4

Hack, Rüdiger

System- und verfahrenstechnischer Vergleich von Nd:YAG- und CO₂-Lasern im Leistungsbereich bis 5 kW
1998, 165 Seiten, ISBN 3-519-06237-2

Krupka, René

Photothermische Charakterisierung optischer Komponenten für Hochleistungslaser
1998, 139 Seiten, ISBN 3-519-06238-0

Pfeiffer, Wolfgang

Fluiddynamische und elektrophysikalisch optimierte Entladungsstrecken für CO₂-Hochleistungslaser
1998, 152 Seiten, ISBN 3-519-06239-9

Volz, Robert

Optimiertes Beschichten von Gußeisen-, Aluminium- und Kupfergrundwerkstoffen mit Lasern
1998, 133 Seiten, ISBN 3-519-06240-2

Bartelt-Berger, Lars

Lasersystem aus kohärent gekoppelten Grundmode-Diodenlasern
1999, 135 Seiten, ISBN 3-519-06241-0

Müller-Hummel, Peter

Entwicklung einer Inprozeßtemperaturmeßvorrichtung zur Optimierung der laserunterstützten Zerspansung
1999, 139 Seiten, ISBN 3-519-06242-9

Rohde, Hansjörg

Qualitätsbestimmende Prozeßparameter beim Einzelpulsbohren mit einem Nd:YAG-Slablaser
1999, 171 Seiten, ISBN 3-519-06243-7

Huonker, Martin

Strahlführung in CO₂-Hochleistungslasersystemen zur Materialbearbeitung
1999, 121 Seiten, ISBN 3-519-06244-5

Callies, Gert

Modellierung von qualitäts- und effektivitätsbestimmenden Mechanismen beim Laserabtragen
1999, 119 Seiten, ISBN 3-519-06245-3

Schubert, Michael E.

Leistungsskalierbares Lasersystem aus fasergekoppelten Singlemode-Diodenlasern
1999, 105 Seiten, ISBN 3-519-06246-1

Kern, Markus

Gas- und magnetofluiddynamische Maßnahmen zur Beeinflussung der Nahtqualität beim Laserstrahlschweißen
1999, 132 Seiten, ISBN 3-519-06247-X

Raiber, Armin

Grundlagen und Prozeßtechnik für das Lasermikrobohren technischer Keramiken
1999, 135 Seiten, ISBN 3-519-06248-8

Laser in der Materialbearbeitung

Forschungsberichte des IFSW (Institut für Strahlwerkzeuge)

Herausgegeben von

Prof. Dr.-Ing. habil. Helmut Hügel, Universität Stuttgart

Forschungsberichte des IFSW ab 2000 erschienen im Herbert Utz Verlag, München

Schittenhelm, Henrik

Diagnostik des laserinduzierten Plasmas beim Abtragen und Schweißen
2000, 141 Seiten, ISBN 3-89675-712-1

Stewen, Christian

Scheibenlaser mit Kilowatt-Dauerstrichleistung
2000, 145 Seiten, ISBN 3-89675-763-6

Schmitz, Christian

Gaselektronische Analysemethoden zur Optimierung von Lasergasentladungen
2000, 107 Seiten, ISBN 3-89675-773-3

Karszewski, Martin

Scheibenlaser höchster Strahlqualität
2000, 132 Seiten, ISBN 3-89675-785-7

Chang, Chin-Lung

Berechnung der Schmelzbadgeometrie beim Laserstrahlschweißen mit Mehrfokustechnik
2000, 141 Seiten, ISBN 3-89675-825-X

Haag, Matthias

Systemtechnische Optimierungen der Strahlqualität von Hochleistungsdiodenlasern
2000, 166 Seiten, ISBN 3-89675-840-3

Bahn Müller, Jochen

Charakterisierung gepulster Laserstrahlung zur Qualitätssteigerung beim Laserbohren
2000, 138 Seiten, ISBN 3-89675-851-9

Schellhorn, Martin Carl Johannes

CO-Hochleistungslaser: Charakteristika und Einsatzmöglichkeiten beim Schweißen
2000, 142 Seiten, ISBN 3-89675-849-7

Angstenberger, Birgit

Fliehkraftunterstütztes Laserbeschichten
2000, 153 Seiten, ISBN 3-89675-861-6

Bachhofer, Andreas

Schneiden und Schweißen von Aluminiumwerkstoffen mit Festkörperlasern für den Karosseriebau
2001, 194 Seiten, ISBN 3-89675-881-0

Breitschwerdt, Sven

Qualitätssicherung beim Laserstrahlschweißen
2001, 150 Seiten, ISBN 3-8316-0032-5

Mochmann, Gunter

Laserkristallisation von Siliziumschichten auf Glas- und Kunststoffsubstraten für die Herstellung verbesserter Dünnschichttransistoren
2001, 170 Seiten, ISBN 3-89675-811-X

Herrmann, Andreas

Fertigungsorientierte Verfahrensentwicklung des Weichlötlens mit Diodenlasern
2002, 133 Seiten, ISBN 3-8316-0086-4

Mästle, Rüdiger

Bestimmung der Propagationseigenschaften von Laserstrahlung
2002, 147 Seiten, ISBN 3-8316-0113-5

Voß, Andreas

Der Scheibenlaser: Theoretische Grundlagen des Dauerstrichbetriebs und erste experimentelle Ergebnisse anhand von Yb:YAG
2002, 195 Seiten, ISBN 3-8316-0121-6

Müller, Matthias G.

Prozessüberwachung beim Laserstrahlschweißen durch Auswertung der reflektierten Leistung
2002, 122 Seiten, ISBN 3-8316-0144-5

Abeln, Tobias

Grundlagen und Verfahrenstechnik des reaktiven Laserpräzisionsabtragens von Stahl
2002, 138 Seiten, ISBN 3-8316-0137-2

Erhard, Steffen

Pumpoptiken und Resonatoren für den Scheibenlaser
2002, 184 Seiten, ISBN 3-8316-0173-9

Contag, Karsten

Modellierung und numerische Auslegung des Yb:YAG-Scheibenlasers
2002, 155 Seiten, ISBN 3-8316-0172-0

Krastel, Klaus

Konzepte und Konstruktionen zur laserintegrierten Komplettbearbeitung in Werkzeugmaschinen
2002, 140 Seiten, ISBN 3-8316-0176-3

Staud, Jürgen

Sensitive Werkzeuge für ein neues Montagekonzept in der Mikrosystemtechnik
2002, 122 Seiten, ISBN 3-8316-0175-5

Schinzel, Cornelius M.

Nd:YAG-Laserstrahlschweißen von Aluminiumwerkstoffen für Anwendungen im Automobilbau
2002, 177 Seiten, ISBN 3-8316-0201-8

Sebastian, Michael

Grundlagenuntersuchungen zur Laser-Plasma-CVD Synthese von Diamant und amorphen Kohlenstoffen
2002, 153 Seiten, ISBN 3-8316-0200-X

Lücke, Bernd

Kohärente Kopplung von Vertikalemitter-Arrays
2003, 120 Seiten, ISBN 3-8316-0224-7

Hohenberger, Bernd

Laserstrahlschweißen mit Nd:YAG-Doppelfokus-
technik – Steigerung von Prozesssicherheit, Fle-
xibilität und verfügbarer Strahlleistung
2003, 128 Seiten, ISBN 3-8316-0223-9

Jasper, Knut

Neue Konzepte der Laserstrahlformung und
-führung für die Mikrotechnik
2003, 152 Seiten, ISBN 3-8316-0205-0

Heimerdinger, Christoph

Laserstrahlschweißen von Aluminiumlegierungen
für die Luftfahrt
2003, 112 Seiten, ISBN 3-8316-0256-5

Christoph Fleig

Evaluierung eines Messverfahrens zur genauen
Bestimmung des Reflexionsgrades optischer
Komponenten
2003, 150 Seiten, ISBN 3-8316-0274-3

Joachim Radtke

Herstellung von Präzisionsdurchbrüchen in ke-
ramischen Werkstoffen mittels repetierender
Laserbearbeitung
2003, 150 Seiten, ISBN 3-8316-0285-9

Michael Brandner

Steigerung der Prozesseffizienz beim Löten und
Kleben mit Hochleistungsdiodenlasern
2003, 195 Seiten, ISBN 3-8316-0288-3

Reinhard Winkler

Porenbildung beim Laserstrahlschweißen von
Aluminium-Druckguss
2004, 153 Seiten, ISBN 3-8316-0313-8

Helmut Kindler

Optische und gerätetechnische Entwicklungen
zum Laserstrahlspritzen
2004, 117 Seiten, ISBN 3-8316-0315-4

Andreas Ruf

Modellierung des Perkussionsbohrens von Metal-
len mit kurz- und ultrakurzgepulsten Lasern
2004, 140 Seiten, ISBN 3-8316-0372-3

Guido Hergenhan

Kohärente Kopplung von Vertikalemittern – Sys-
temkonzept und experimentelle Verifizierung
2004, 115 Seiten, ISBN 3-8316-0376-6

Klaus Goth

Schweißen von Mischverbindungen aus Alumini-
umguß- und Knetlegierungen mit CO₂-Laser
unter besonderer Berücksichtigung der Nahtart
2004, 143 Seiten, ISBN 3-8316-0427-4

Armin Strauch

Effiziente Lösung des inversen Problems beim
Laserstrahlschweißen durch Simulation und
Experiment
2004, 169 Seiten, ISBN 3-8316-0425-8

Thomas Wawra

Verfahrensstrategien für Bohrungen hoher Präzi-
sion mittels Laserstrahlung
2004, 162 Seiten, ISBN 3-8316-0453-3

Michael Honer

Prozesssicherungsmaßnahmen beim Bohren
metallischer Werkstoffe mittels Laserstrahlung
2004, 113 Seiten, ISBN 3-8316-0441-x

Thomas Herzinger

Prozessüberwachung beim Laserbohren von
Turbinenschaufeln
2004, 143 Seiten, ISBN 3-8316-0443-6

Reiner Heigl

Herstellung von Randschichten auf Aluminium-
gusslegierungen mittels Laserstrahlung
2004, 173 Seiten, ISBN 3-8316-0460-8

Laser in der Materialbearbeitung

Forschungsberichte des IFSW (Institut für Strahlwerkzeuge)

Herausgegeben von

Prof. Dr. phil. nat. Thomas Graf, Universität Stuttgart

Forschungsberichte des IFSW ab 2005 erschienen im Herbert Utz Verlag, München

Thomas Fuhrich

Marangoni-effekt beim Laserstrahl-tiefschweißen von Stahl

2005, 163 Seiten, ISBN 3-8316-0493-2

Daniel Müller

Pulsenergiestabilität bei regenerativen Kurzpuls-verstärkern im Scheibenlaserdesign

2005, 172 Seiten, ISBN 3-8316-0508-4

Jiancun Gao

Neodym-dotierte Quasi-Drei-Niveau-Scheiben-laser: Hohe Ausgangsleistung und Frequenzver-dopplung

2005, 148 Seiten, ISBN 3-8316-0521-1

Wolfgang Gref

Laserstrahlschweißen von Aluminiumwerkstoffen mit der Fokusmatrixtechnik

2005, 136 Seiten, ISBN 3-8316-0537-8

Michael Weikert

Oberflächenstrukturieren mit ultrakurzen Laser-pulsen

2005, 116 Seiten, ISBN 3-8316-0573-4

Julian Sigel

Lasergenerieren metallischer Bauteile mit vari-ablem Laserstrahldurchmesser in modularen Fert-igungssystemen

2006, 132 Seiten, ISBN 3-8316-0572-6

Andreas Ruß

Schweißen mit dem Scheibenlaser-Potentiale der guten Fokussierbarkeit

2006, 142 Seiten, ISBN 3-8316-0580-7

Gabriele Seibold

Absorption technischer Oberflächen in der La-sermaterialbearbeitung

2006, 156 Seiten, ISBN 3-8316-0618-8

Dirk Lindenau

Magnetisch beeinflusstes Laserstrahlschweißen

2007, 180 Seiten, ISBN 978-3-8316-0687-0

Jens Walter

Gesetzmäßigkeiten beim Lasergenerieren als Basis für die Prozesssteuerung und -regelung

2008, 140 Seiten, ISBN 978-3-8316-0770-9

Heiko Ridderbusch

Longitudinal angeregte passiv gütegeschaltete Laserzündkerze

2008, 175 Seiten, ISBN 978-3-8316-0840-9

Markus Leimser

Strömungsinduzierte Einflüsse auf die Nahteigenschäften beim Laserstrahlschweißen von Aluminiumwerkstoffen

2009, 150 Seiten, ISBN 978-3-8316-0854-6

Mikhail Larionov

Kontaktierung und Charakterisierung von Kristal-len für Scheibenlaser

2009, 186 Seiten, ISBN 978-3-8316-0855-3

Jürgen Müller-Borhanian

Kamerabasierte In-Prozessüberwachung beim Laserstrahlschweißen

2009, 162 Seiten, ISBN 978-3-8316-0890-4

Andreas Letsch

Charakterisierung allgemein astigmatischer La-serstrahlung mit der Methode der zweiten Mo-mente

2009, 176 Seiten, ISBN 978-3-8316-0896-6

Thomas Kübler

Modellierung und Simulation des Halbleiterschei-benlasers

2009, 152 Seiten, ISBN 978-3-8316-0918-5

Günter Ambrosy

Nutzung elektromagnetischer Volumenkräfte beim Laserstrahlschweißen

2009, 170 Seiten, ISBN 978-3-8316-0925-3

Agnes Ott

Oberflächenmodifikation von Aluminiumlegierun-gen mit Laserstrahlung: Prozessverständnis und Schichtcharakterisierung

2010, 226 Seiten, ISBN 978-3-8316-0959-8

Detlef Breitling

Gasphaseneinflüsse beim Abtragen und Bohren mit ultrakurz gepulster Laserstrahlung

2010, 200 Seiten, ISBN 978-3-8316-0960-4

Dmitrij Walter

Online-Qualitätssicherung beim Bohren mittels ultrakurz gepulster Laserstrahlung

2010, 156 Seiten, ISBN 978-3-8316-0968-0

Jan-Philipp Weberpals

Nutzen und Grenzen guter Fokussierbarkeit beim Laserstrahlschweißen

2010, 154 Seiten, ISBN 978-3-8316-0995-6

Angelika Beyertt

Yb:KYW regenerativer Verstärker für ultrakurze Pulse

2010, 166 Seiten, ISBN 978-3-8316-4002-7

Christian Stolzenburg

Hochrepetierende Kurzpuls-Scheibenlaser im infraroten und grünen Spektralbereich
2011, 184 Seiten, ISBN 978-3-8316-4041-6

Svent-Simon Beyertt

Quantenfilm-Pumpen zur Leistungsskalierung von Halbleiter-Scheibenlasern
2011, 130 Seiten, ISBN 978-3-8316-4051-5

Sonja Kittel

Verzugsarmes Laserstrahlschweißen an axial-symmetrischen Bauteilen
2011, 162 Seiten, ISBN 978-3-8316-4088-1

Andrey Andreev

Schweißen mit dem Scheibenlaser im Getriebebau – Prozessmerkmale und Anlagenkonzepte
2011, 140 Seiten, ISBN 978-3-8316-4103-1

Christian Föhl

Einsatz ultrakurz gepulster Laserstrahlung zum Präzisionsbohren von Metallen
2011, 156 Seiten, ISBN 978-3-8316-4120-8

Andreas Josef Birnesser

Prozessregelung beim Laserstrahlschweißen
2011, 150 Seiten, ISBN 978-3-8316-4133-8

Christoph Neugebauer

Thermisch aktive optische Bauelemente für den resonatorinternen Einsatz beim Scheibenlaser
2012, 220 Seiten, ISBN 978-3-8316-4178-9

Andreas Dauner

Fluidmechanische Maßnahmen zur Reduzierung von Schmelzablagerungen beim Hochgeschwindigkeitslaserbohren
2012, 150 Seiten, ISBN 978-3-8316-4194-9

Axel Heß

Vorteile und Herausforderungen beim Laserstrahlschweißen mit Strahlquellen höchster Fokussierbarkeit
2012, 164 Seiten, ISBN 978-3-8316-4198-7

Christian Gehrke

Überwachung der Struktureigenschaften beim Oberflächenstrukturieren mit ultrakurzen Laserpulsen
2013, 164 Seiten, ISBN 978-3-8316-4271-7

David Schindhelm

In-Prozess Qualitätssicherung für das Laserstrahlschneiden von Metallen
2013, 150 Seiten, ISBN 978-3-8316-4345-5

Moritz Vogel

Speciality Fibers for High Brightness Laser Beam Delivery
2014, 187 Seiten, ISBN 978-3-8316-4382-0

Andreas Michalowski

Untersuchungen zur Mikrobearbeitung von Stahl mit ultrakurzen Laserpulsen
2014, 176 Seiten, ISBN 978-3-8316-4424-7

Georg Stöppler

Untersuchung eines OPOs im mittleren Infrarot im Hinblick auf Anwendungen für minimalinvasive Chirurgie
2015, 144 Seiten, ISBN 978-3-8316-4437-7

Patrick Mucha

Qualitäts- und produktivitätsbeeinflussende Mechanismen beim Laserschneiden von CF und CFK
2015, 120 Seiten, ISBN 978-3-8316-4516-9

Claus-Dieter Reiniger

Fluiddynamische Effekte beim Remote-Laserstrahlschweißen von Blechen mit Fügespalt
2015, 188 Seiten, ISBN 978-3-8316-4528-2

Andreas Leitz

Laserstrahlschweißen von Kupfer- und Aluminiumwerkstoffen in Mischverbindung
2016, 172 Seiten, ISBN 978-3-8316-4549-7

Peter Stritt

Prozessstrategien zur Vermeidung von Heißrissen beim Remote-Laserstrahlschweißen von AlMgSi 6016
2016, 194 Seiten, ISBN 978-3-8316-4555-8

Katrin Sarah Wentsch

Analyse Ytterbium-dotierter Materialien für den Einsatz in ultrakurz-gepulsten Scheibenlasersystemen
2016, 162 Seiten, ISBN 978-3-8316-4578-7

Jan-Philipp Negel

Scheibenlaser-Multipassverstärker für ultrakurze Laserpulse mit Ausgangsleistungen im kW-Bereich
2017, 142 Seiten, ISBN 978-3-8316-4632-6

Christian Freitag

Energietransportmechanismen bei der gepulsten Laserbearbeitung Carbonfaser verstärkter Kunststoffe
2017, 152 Seiten, ISBN 978-3-8316-4638-8

Andreas Popp

Faserlaser und Faserlaserverstärker als Brillanzkonverter für Scheibenlaserstrahlen
2017, 242 Seiten, ISBN 978-3-8316-4638-8

Karin Heller

Analytische Temperaturfeldbeschreibung beim Laserstrahlschweißen für thermographische Prozessbeobachtung
2017, 130 Seiten, ISBN 978-3-8316-4654-8

Stefan Piehler

Resonatorinterne Kompensation thermisch induzierter Wellenfrontstörungen in hochbrillanten Scheibenlasern
2017, 148 Seiten, ISBN 978-3-8316-4690-6

Felix Abt

Bildbasierte Charakterisierung und Regelung von Laserschweißprozessen
2017, 232 Seiten, ISBN 978-3-8316-4691-3

Volker Rominger

Untersuchungen der Prozessvorgänge bei Einschweißungen in Baustahl mit Lasern hoher Brillanz
2017, 186 Seiten, ISBN 978-3-8316-4692-0

Thomas Rataj

Hochleistungstaugliche faserintegrierte Strahlweichen
2018, 142 Seiten, ISBN 978-3-8316-4733-0

Michael Diez

Pulsformung zur schädigungsarmen Laserbearbeitung von Silizium
2018, 194 Seiten, ISBN 978-3-8316-4737-8

Andreas Heider

Erweitern der Prozessgrenzen beim Laserstrahlschweißen von Kupfer mit Einschweißtiefen zwischen 1 mm und 10 mm
2018, 156 Seiten, ISBN 978-3-8316-4738-5

Marcel Schäfer

Energetische Beeinflussung von Schmelzfluss und Heißrißbildung beim Laserstrahlschweißen von Vergütungsstahl
2018, 146 Seiten, ISBN 978-3-8316-4742-2

Laser in der Materialbearbeitung

Forschungsberichte des IFSW (Institut für Strahlwerkzeuge)

Herausgegeben von

Prof. Dr. phil. nat. Thomas Graf, Universität Stuttgart

Forschungsberichte des IFSW ab 2019 erschienen im utzverlag, München

Tom Dietrich

Gitterwellenleiterstrukturen zur Strahlformung in Hochleistungsscheibenlasern
2019, 154 Seiten, ISBN 978-3-8316-4785-9

Martin Rumpel

Applications of Grating Waveguide Structures in Solid-State Lasers
2019, 112 Seiten, ISBN 978-3-8316-4801-6

Michael Eckerle

Generation and amplification of ultrashort pulsed high-power cylindrical vector beams
2019, 112 Seiten, ISBN 978-3-8316-4804-7

